THE DEVELOPMENT OF A CORTICAL BONE TURNOVER MODEL: PARATHYROID HORMONE EFFECTS IN THE RABBIT

A Thesis Submitted to the
College of Graduate and Postdoctoral Studies
In Partial Fulfillment of the Requirements
For the Degree of Masters of Science
In the Department of Anatomy & Cell Biology
University of Saskatchewan
Saskatoon

By

Beverly Hiebert

PERMISSION TO USE

In presenting this thesis/dissertation in partial fulfillment of the requirements for a Postgraduate degree from the University of Saskatchewan, I agree that the Libraries of this University may make it freely available for inspection. I further agree that permission for copying of this thesis/dissertation in any manner, in whole or in part, for scholarly purposes may be granted by the professor or professors who supervised my thesis/dissertation work or, in their absence, by the Head of the Department or the Dean of the College in which my thesis work was done. It is understood that any copying or publication or use of this thesis/dissertation or parts thereof for financial gain shall not be allowed without my written permission. It is also understood that due recognition shall be given to me and to the University of Saskatchewan in any scholarly use which may be made of any material in my thesis/dissertation.

Requests for permission to copy or to make other uses of materials in this thesis/dissertation in whole or part should be addressed to:

Head of the Department of Anatomy & Cell Biology
Health Science Building
107 Wiggins Rd
University of Saskatchewan
Saskatoon, Saskatchewan S7N 5E5 Canada

OR

Dean
College of Graduate and Postdoctoral Studies
University of Saskatchewan
116 Thorvaldson Building, 110 Science Place
Saskatoon, Saskatchewan S7N 5C9 Canada

ABSTRACT

Osteoporosis (OP) is a disease of progressive bone loss that is intimately linked with bone remodeling, a lifelong process of turnover essential for the maintenance of bone microarchitecture. Remodeling involves processes of coupled bone resorption and formation, carried out by complex cellular groupings known as basic multicellular units (BMUs). Imbalances in remodeling, where bone resorption exceeds formation, leads to elevations in cortical porosity and an increased risk of OP. Understanding the spatio-temporal coordination of BMUs is the key to elucidating the mechanisms underpinning cortical bone loss associated with OP and developing therapeutic approaches aimed at improving the balance between BMU phases to minimize bone loss. Much of the research on this subject has been largely theoretical or *in silico* thus far due to the lack of direct empirical evidence. Combining the use of high-resolution synchrotron based micro-computed tomography (micro-CT), a powerful imaging tool capable of characterizing cortical porosity in three-dimensional (3D) space, with the appropriate animal model has the potential to directly track individual BMUs and assess their behaviours *in vivo*. Rabbits are suitable model systems since they are the smallest laboratory animals to exhibit cortical bone remodeling like humans, however, remodeling rates in their cortices are generally low and approaches aimed at increasing remodeling have largely focused on trabecular bone. Therefore, there exists a need to develop an operationally effective cortical bone model given the growing recognition of the role cortical bone microarchitecture plays in bone loss and fragility in OP. The primary aim of this thesis was to establish a cortical porosity model in the rabbit using parathyroid hormone (PTH), a known inducer of cortical remodeling at intermittent levels. The experiment described in this thesis is presented as one aspect of a larger study characterizing numerous rabbit-based models of cortical bone loss (ovariectomy and glucocorticoid induced), all of which are compared to a control. After one month of intermittent PTH administration, cortical bone microarchitectural changes in the distal tibiae of rabbits were assessed *ex vivo* using micro-CT at a resolution of 10 μm and dynamic histomorphometry. Trabecular bone microarchitecture of the proximal tibial epiphysis was assessed secondarily. Results indicated that cortical porosity was substantially elevated in PTH rabbits relative to controls, and this was associated with increases in remodeling rate and cortical pore size. Despite bone losses intracortically, bone formation was evident on endosteal and periosteal surfaces of the tibiae and the rate of new bone deposition was increased in BMUs. Furthermore, a pattern of bone gain was observed in the proximal tibial epiphysis indicated by changes in micro-CT derived trabecular microarchitectural parameters. Notably, remodeling induced by PTH appeared to be distinct from that of the other rabbit-based models of bone loss in this larger study, with regards to cortical porosity and trabecular bone structural changes, warranting further investigations into these intriguing PTH-driven effects. Overall, the PTH rabbit model provides an effective and novel platform for developing future mechanistic studies aimed at testing a number of hypotheses directly related to bone remodeling regulation, which would ultimately enhance our understanding of the complex and dynamic nature of cortical bone in health and disease.

ACKNOWLEDGEMENTS

I would like to express my deepest gratitude to my supervisor Dr. Dave Cooper for his endless support, guidance, and assistance during this journey. He has been such an important part of my academic and personal development, helping me foster my interest in the scientific process and providing me with an abundance of knowledge and invaluable advice that I will be taking with me into the next chapter of my life. I also greatly appreciate the many additional opportunities Dave has provided me with that have enriched my research program, like working on other projects, attending conferences, and gaining teaching experience. Dave exemplifies everything a researcher, supervisor, and mentor should be and I feel so privileged to have worked with someone who is so hard working and dedicated to his students and work.

I would like to extend my gratitude to the other members of my advisory committee, Drs. Julia Boughner and Terra Arnason. I am grateful for their insights and thoughtful inputs on my work and appreciative of their helpful advice, both in and outside of the lab.

I would especially like to thank the co-authors of the manuscript included in this thesis for their contributions: Kim Harrison, Arash Panahifar, Janna Andronowski, Amir Ashique, Gavin King, Terra Arnason, Kurtis Swekla, Peter Pivonka, and of course, Dave. I would like to further thank my co-lead author Kim, for making this partnership such an easy and enjoyable one (despite the many late nights of work!) and for being such a great friend to me. I would also like to thank the Laboratory Animal Services Unit for their assistance with the rabbits, Ingrid Pickering and Natalia Dolgova for training and use of the confocal microscope, and Adi Manek for generously lending his expertise, time, and efforts with optimizing the histology work.

I would like to recognize the various sources of funding that have made this research possible – the Canadian Institutes of Health Research, the University of Saskatchewan College of Medicine, and to Dave Cooper, for his generosity and support.

My sincerest thanks go out to my fellow Cooper lab mates, past & present, for not only providing me with scientific and emotional support but also for the indispensable friendships and laughs. I would particularly like to thank Kim Harrison, Gavin King, and Kush Parolia for the countless office conversations and puzzle breaks that have kept me sane during this journey.

I would like to acknowledge my first grad school friends, Lexi Busse and Cassy Appelt, whom I surely would not have been able to endure the ups and downs of grad school without.

I am grateful for my long distance support systems; to Ally Simms and Nicole Breedon for their friendships and positive words of encouragement and to my second family, Manda Guest, Scott Van Os, Aurora-Lyn, and Ezmay, for their undeniable support and for always being there for me throughout my academic pursuits.

Last but certainly not least, I would like to sincerely thank my family – to my parents for their unconditional love and support (emotionally & financially), to Amanda and Derek (and pups!) for always having my back no matter what, and to my twin/roommate/best friend Crystal, who deserves the greatest recognition for being my rock throughout this whole journey. I can honestly say that this achievement would not have been possible without her unwavering support, encouragement, motivation, and cheers during the past 3 years.

DEDICATION

I dedicate this thesis to my dad, mom, and sisters.
Brian, Julia, Amanda, & Crystal

TABLE OF CONTENTS

LIST OF TABLES

LIST OF FIGURES

LIST OF ABBREVIATIONS

°	Degrees
%	Percent
2D	Two-Dimensional
3D	Three-Dimensional
4D	Four-Dimensional
α	Alpha
Ac.f	Activation Frequency
a.Rm.Cr	Active Remodeling Center
BFR	Bone Formation Rate
BMD	Bone Mineral Density
BMU	Basic Multicellular Unit
BS	Bone Surface
BV/TV	Bone Volume fraction
C	Celsius
Ca.Dm	Canal Diameter
Ct.Ar	Cortical Area
Ct.Po	Cortical Porosity
Ct.Th	Cortical Thickness
CCAC	Canadian Council on Animal Care
CLS	Canadian Light Source
CI	Confidence Interval
cm	Centimeter
CT	Computed Tomography
DKK1	Dickkopf-1
DIC	Differential Interference Contrast microscopy
dL.On	Double Labelled Osteon
dLS	Double labelled Bone Surface
DXA	Dual-Energy X-ray Absorptiometry
Es.MS/BS	Endosteal Mineralizing Surface per Bone Surface
EtOH	Ethanol
FDA	American Food and Drug Administration
g	Gram
GC	Glucocorticoid *(referring to both the class of drugs and within Chapter 3, the group of rabbits treated with glucocorticoids)*
Gy	Gray
HR-pQCT	High Resolution peripheral Quantitative Computed Tomography
IGF-1	Insulin-like Growth Factor 1
I_{max}	Maximum second moment of area

I_{min}	Minimum second moment of area
in.Hg	inch of Mercury
Kg	Kilogram
kVp	Peak Kilovoltage
LER	Longitudinal Erosion Rate
M	Molar
Ma.Ar	Marrow Area
MAR	Mineral Apposition Rate
Micro-CT	Micro-Computed Tomography
ml	Milliliter
mg	Milligram
mm	Millimeter
MMA	Methylmethacrylate
ms	Millisecond
MS/BS	Mineralizing Surface per bone Surface
n	Sample size
ND	No Data
OCT	Optimal Cutting Temperature medium
On.MAR	Osteonal Mineral Apposition Rate
OP	Osteoporosis
OPG	Osteoprotegerin
OVX	Ovariectomy *(referring to either the surgical procedure or in the case of Chapter 3, the rabbit group subject to this procedure)*
OVX+GC	Ovariectomy & Glucocorticoid
PBS	Phosphate Buffered Saline
PHPT	Primary Hyperparathyroidism
Ps.MS/BS	Periosteal Mineralizing Surface per Bone Surface
PTH	Parathyroid Hormone *(referring to both the drugs and within Chapter 3, the group of rabbits treated with parathyroid hormone)*
RANKL	Receptor Activator of Nuclear factor Kappa-β Ligand
ROI	Region of Interest
Rs.N	Resorption Cavity
Runx2	Runt-related transcription factor 2
σ_f	Osteon formation time
SCEM	Supercryoembedding medium
SD	Standard Deviation
SHAM	Sham control
sL.On	Single Labelled Osteon
sLS	Single Labelled Bone Surface
Tb.N	Trabecular Number

Tb.Sp	Trabecular Spacing
Tb.Th	Trabecular Thickness
TGF- β	Transforming Growth Factor-β
Tt.Ar	Total Area
µA	Microampere
µg	Microgram
µm	Micron
VOI	Volume of Interest
vs	Versus
Wnt	Mammalian homologue of wingless-related integration site in drosophila
W.Th	Wall Thickness
Z_{pol}	Torsional section modulus

CHAPTER 1. Introduction

1.1. Introduction

1.11. Bone Microarchitecture & Remodeling

Bone is a living, dynamic tissue that serves to provide mechanical support and protection to the body and plays an important role in calcium and phosphate homeostasis. Bone consists of the calcium-phosphate mineral hydroxyapatite and collagen fibers to provide compressive and tensile strength to bones, respectively. Bone is made up of two major structural types, trabecular and cortical bone (Figure 1.1). Trabecular (spongy, cancellous) bone consists of interconnected plates and rods of bone (trabeculae) predominantly found in bones like the vertebrae or in the ends, or epiphyses, of long bones. Cortical (compact) bone forms the dense outer shell of bones and is the primary component of the shaft or diaphysis of a long bone, surrounding the inner marrow cavity. The organization of bone is related to its functional needs. Trabecular bone provides structural support while minimizing added weight and is the primary site of mineral homeostasis due to its abundant surface area. Cortical bone's dense and rigid structure substantially contributes to the overall mechanical strength of bone (1).

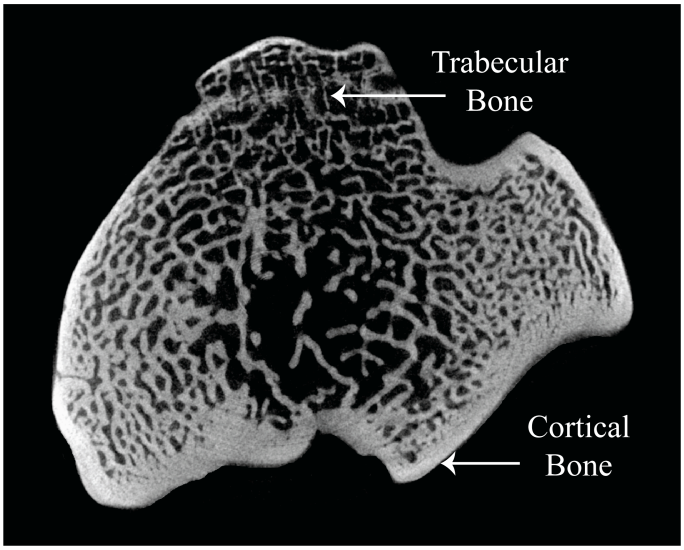

Figure 1.1. Micro-CT image depicting cortical and trabecular bone. This scan was taken from the proximal epiphysis of the tibia from a rabbit. Cortical bone comprises the outer shell surrounding trabecular bone and the inner marrow cavity.

Bones are formed during development by two distinct processes: intramembranous ossification, which involves the development of bone directly from primitive connective tissue, and endochondral ossification, where a cartilaginous template is gradually replaced by mineralized bone (2). The primary accumulation of bone tissue by these processes results in growth (3). During growth and development, the size and shape of bones are modified in a process known as **modeling** (3). This is accomplished by the coordinated actions of osteoclasts, which are multi-nucleated cells that remove or resorb bone, and osteoblasts, which are cells that are responsible for forming bone (4) (Figure 1.2). These processes occur independently of one another, taking place on separate, pre-existing bone surfaces. The bone formed during growth is known as primary bone, which can be deposited as lamellar bone or woven bone (1). Lamellar bone is characterized by parallel collagen fiber orientation, creating concentric layers of bone seen primarily within the diaphysis. Woven bone has an irregular appearance due to highly disorganized collagen fibers. This type of bone is associated with rapid growth and is also found during fracture repair or in states of high bone turnover. As primary bone is being deposited, vascular canals which may form into primary osteons through subsequent infilling with new bone (5). While prevalent during growth, a low level of modeling continues into adulthood and modeling can occur in response to alterations in mechanical loads, thereby modifying the position of the bone relative to its central axis, lending to the term "modeling drift" (2).

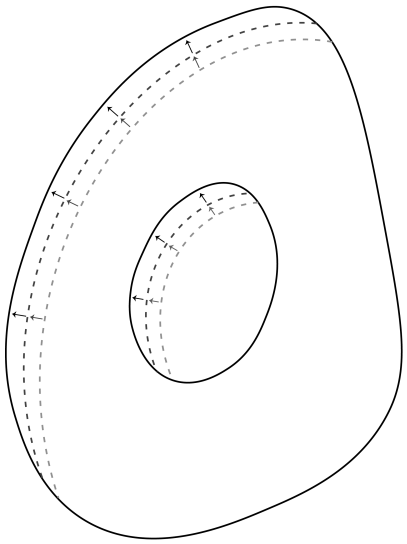

Figure 1.2. Schematic of a transverse section through a long bone undergoing bone modeling. The independent actions of osteoclasts and osteoblasts modify the external structure of bone, in this case, removing bone from the endosteal surface and adding bone to the periosteal surface, contributing to the bone's appositional growth or as an adaptation to mechanical loads.

After development ceases, the existing bone is continually turned over in a process known as bone **remodeling** (4). Remodeling maintains skeletal integrity throughout one's lifetime by replacing old and damaged bone with new tissue and by mediating bone tissue level adaptation to mechanical demands associated with loading (6). Remodeling can occur in cortical bone and on trabecular, endosteal, and periosteal bone surfaces. The endosteal surface lines the inner surface of bone surrounding the marrow cavity while the periosteal surface refers to the outer surface of a bone. Bone remodeling consists of three highly coordinated, sequential stages: activation, resorption, and then formation, carried out by a group of specialized bone cells collectively known as the Basic Multicellular Unit (BMU) (4) (Figure 1.3). The BMUs in cortical and trabecular bone (as well as on bone surfaces) differ in the way they remove and form bone and therefore, their morphologies also differ. The remodeling process is activated by a molecular or mechanical signal that triggers the recruitment and differentiation of osteoclast precursors to a bone surface (7). Osteoclasts then resorb bone, forming a trench-like pit on trabecular, endosteal, and periosteal surfaces or a tunnel like resorption space known as the cutting cone in cortical bone. Once a trench or tunnel is excavated to a certain size, osteoblasts fill the space in with osteoid, an unmineralized bone matrix that eventually becomes calcified to form mature bone. On bone surfaces, this process yields a hemi-osteon (8) (Figure 1.3). In cortical bone, this new bone is deposited around a central canal in densely packed, concentric layers known as lamellae, creating the closing cone (Figure 1.3). The resulting structure is a secondary osteon or Haversian system (8) (Figure 1.4). The central canal contains a neurovascular bundle that supplies mature osteocytes or bone cells that are arranged in the lamellae. Perforating Volkmann's canals run transversely connecting the osteons to each other as well as to the endosteal and periosteal surfaces (1). The cement line demarcates the outer border of the osteon and represents the maximum limits of the cutting cone that had been created during bone remodeling (6). In addition to the presence of a cement line, secondary osteons differ from primary osteons in that they are greater in size and have more abundant lamellae. Between the cutting and closing cones, a reversal zone exists, spatially and temporally coupling bone resorption to bone formation (Figure 1.3) (9). Within the reversal zone, osteoclastic activity transitions to osteoblastic activity as osteoclasts undergo apoptosis and osteoblast precursors differentiate into mature cells to synthesize new bone (7). The exact cellular and molecular mechanisms that mediate the coupling of resorption to formation has not yet been fully elucidated therefore BMU coupling remains as an important topic of much inquiry. Under normal conditions, the sequential activities within a BMU are balanced, such that bone resorption equals bone formation, maintaining bone structure and minimizing bone loss.

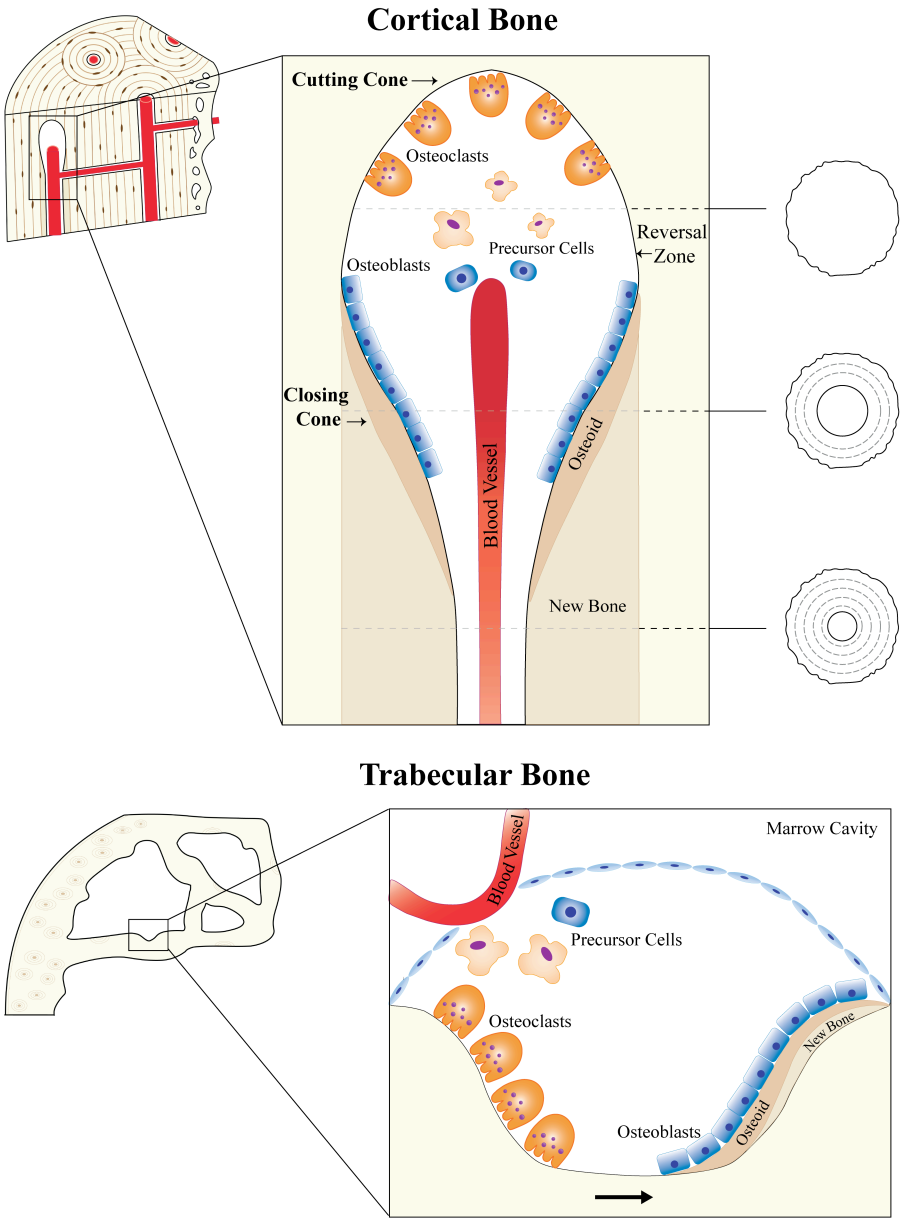

Figure 1.3. Schematic illustrating cortical and trabecular bone remodeling. In cortical bone, osteoclasts remove old or damaged bone creating a tunnel like resorption space known as the cutting cone. Osteoblasts follow in the closing cone, filling the space with new bone, first as osteoid, then as mineralized bone. A reversal zone exists between the two phases, coupling bone resorption to bone formation. Collectively, this group of cells is known as a basic multicellular unit (BMU) and their activity creates a new secondary osteon. Trabecular bone remodeling results in a BMU of different morphology than that of cortical bone. Osteoclasts resorb bone on a surface to form a trench, which is then refilled by new bone via osteoblasts, creating a hemi-osteon.

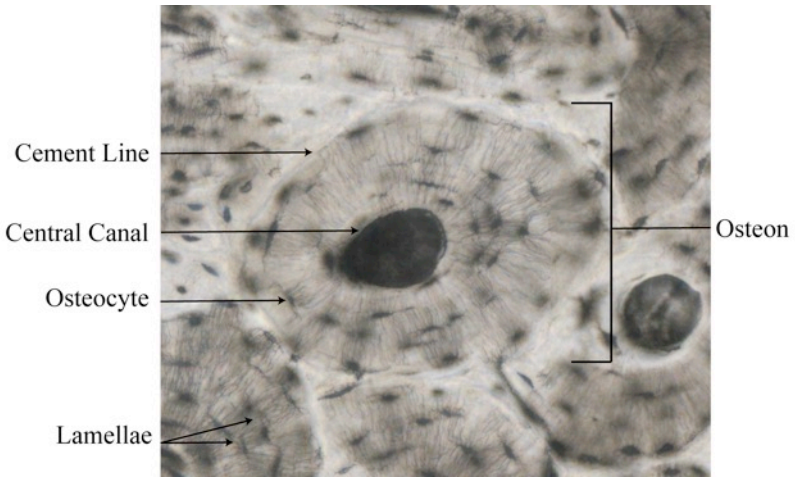

Figure 1.4. Micrograph of a secondary osteon in cortical bone (transverse section, 20X). The secondary osteon is a product of bone remodeling consisting of layers of bone (lamellae) surrounding the central canal, which contains the neurovascular bundle that sustains the osteocytes, or bone cells. The lamellae are enclosed within the outer boundary of the osteon, known as the cement line. Secondary osteons can be distinguished from primary osteons, the vascular canals found in primary bone created during growth, by their larger size and more abundant lamellae.

1.12. Osteoporosis

Normally, the integrity of the skeleton is maintained through balanced activities between osteoblasts and osteoclasts, but as humans age and in certain conditions, the bone remodeling rate accelerates and bone resorption outweighs bone formation resulting in bone loss and an increased risk of osteoporosis (OP) (10). Osteoporosis is a disease characterized by the structural deterioration of the skeleton and low bone mass, which increases the risk of fractures (11). Osteoporosis is classified by the different factors that contribute to bone loss. Primary OP is associated with aging and with estrogen deficiency in postmenopausal women (12). Secondary OP is defined as low bone mass in the presence of an underlying condition or pharmaceutical agents, such as chronic glucocorticoid (GC) treatment, immobility, anti-gravity scenarios, or in diseases like primary hyperparathyroidism (PHPT), where parathyroid hormone (PTH) is continually and excessively produced by the parathyroid gland, which under normal conditions, releases PTH in a pulsatile manner and responds to feedback inhibition (13). Osteoporosis has a large impact on the Canadian population currently afflicting 2 million Canadians (11) and costing the healthcare system $2.3 billion annually (14). In trabecular bone, remodeling imbalance leads to the thinning and loss of trabeculae (15) and its overall structure becomes less interconnected (16). Bone within this compartment is thought to be lost at a more rapid rate due to the higher rate of remodeling in comparison to cortical bone, lending to the conventional "trabeculocentric" view of bone loss in OP. Significant losses are however, observed within cortical bone with age (17, 18) and cortical bone is the site for which approximately 80% of all

fractures in old age occur in, such as the hip and distal wrist for example (19, 20). Cortical bone loss results from elevations in porosity as well as the size of cortical pores themselves, increasing the likelihood of coalescence in regions near the endosteal surface, leading to cortical thinning (21). Currently, therapies for treating osteoporosis are aimed at reducing bone resorption like widely used anti-resorptive drugs such as bisphosphonates and denosumab. These approaches rely on inhibiting osteoclastic formation and activity to increase bone mineral density (BMD), however this is a result of increased mineralization of the existing bone and not the acceleration of new bone formation. These treatments cannot reverse the structural deterioration that is already present at the time of treatment (22) and because of the coupled nature of BMU phases, bone formation will not ensue as bone resorption is suppressed. Furthermore, while the use of these treatments are generally safe and widely used, there is a growing body of literature documenting rare yet serious side effects of these drugs (ie., osteonecrosis of jaw, atypical femoral fractures, fatal strokes, and venous thromboembolic events) (23-26). Because OP arises from an imbalance in bone remodeling processes, strategies to prevent or reverse osteoporosis must aim to improve the balance between the resorptive and formative phases within individual BMUs. The ideal therapy for individuals susceptible to OP would involve slowing down the rate of resorption, both longitudinally and radially, while speeding up formation to minimize bone loss. Such therapies are not yet developed or available. In order to reach this potential, we need to have a thorough understanding of the spatio-temporal behaviour of BMUs.

1.13. Analysis of the Dynamic Activity of BMUs with Histology and Imaging

Despite its significance for bone adaptation and disease, the spatio-temporal behaviour of BMUs has never been replicated *in vitro*, nor has is been directly observed *in vivo*, and therefore there is little known about the three-dimensional (3D) or four-dimensional (4D) coordination of remodeling events. While we do know of factors that affect BMU activity and contribute to osteoporosis (certain disease states, pharmaceutical use), it is not well established how these factors impact the rate of advance or the coordination of remodeling events within an individual BMU. Elevations in porosity may be a result of an increase in the rate of BMU progression, an increase in the number of BMUs, or both. Most of the dynamic activity we know about BMUs is formative, largely derived from histological bone fluorochrome labelling studies, or dynamic histomorphometry, which enables the analysis of the rate of change in bone tissue, particularly with regards to remodeling (4, 27). Bone fluorochrome labels bind to newly calcified bone, thereby labelling the osteoblastic closing cone at the time of administration. The fluorescent label can be visualized in a histological section of a bone biopsy with ultraviolet or blue light. When labels are administered at two different time points, the amount of bone formed within that time interval, measured as the distance between the two labels, can be determined from longitudinal histological sections (Figure 1.5). Aspects of the resorptive phase have only been inferred indirectly based on this technique. The histological measure of longitudinal erosion rate (LER), or cutting cone advance, has been measured based on the assumption that cutting cone advance is equal to that of closing cone advance (Figure 1.5). This measure has only been assessed in two

studies from the 1970s, reporting LERs of approximately 40 μm/day (28, 29). This value has been utilized in studies simulating BMU dynamics *in silico* using predictive, theoretical models and computer simulations (30-32). Despite being frequently cited, these classic studies bear several limitations. For instance, small sample sizes of mongrel dogs (n = 3-5) were used and LER was only assessed in the rib (28, 29). The results also showed a large level of variation in the rate of advance as well as the size of the reversal zone between the cutting and closing cone (29), indicating variation in BMU activity. This variation indicates BMU behaviour may in fact vary considerably across species and bone types and be influenced by external factors. This variation is not taken into consideration in the classical histological measure of LER, yet has been the potentially flawed foundation upon which all subsequent studies have been based on.

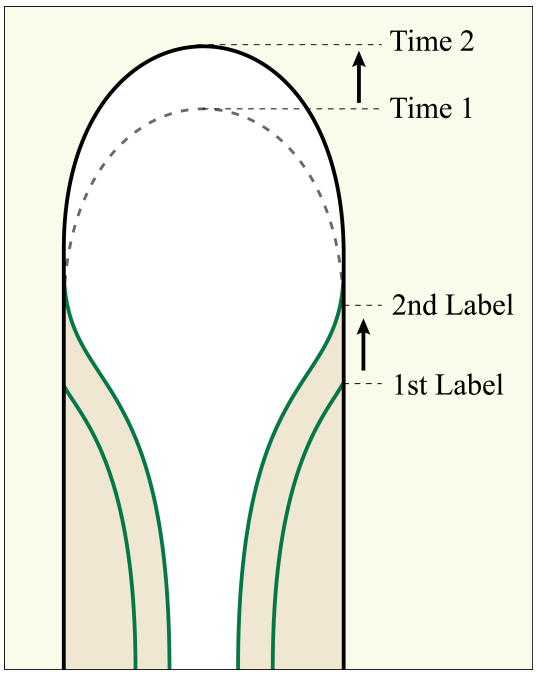

Figure 1.5. A schematic of a longitudinal section of cortical bone depicting a BMU analyzed with dynamic histomorphometry. Dual bone fluorochrome labels, which incorporate into newly mineralized bone, are administered *in vivo* to enable the direct quantification of closing cone advance, or the amount of bone formed within the labelling period (distance between 1nd Label and 2nd Label). Longitudinal erosion rate (LER), or the rate of cutting cone advance (distance between Time 1 and Time 2), has only been inferred from the rate of closing cone advance, under the assumption that the two activities are equal. This histological measure of LER was measured in two classic studies from the 1970s (28, 29).

Micro-computed tomography (micro-CT) provides a non-destructive pathway for the 3D visualization of cortical bone microarchitecture (33). Micro-CT is an essential imaging tool that uses X-rays to visualize skeletal structure in high resolution. A direct, accurate measure of LER can be obtained utilizing this high-resolution imaging modality to provide novel 3D and 4D information about cortical porosity; however, *in vivo* imaging is limited by the radiation dose it imparts. In order to increase imaging resolution, radiation dose is required to increase exponentially (34). Other imaging modalities that can assess bone microarchitecture *in vivo*, like high-resolution peripheral quantitative computed tomography (HR-pQCT), are not capable of imaging with high enough resolution to sufficiently resolve all vascular pores. Standard patient HR-pQCT operates at an isotropic voxel size of ~82 μm (35, 36), while newer second-generation HR-pQCT can image with a higher spatial resolution of ~61 μm (37, 38). These systems are ideal for the assessment of trabecular bone microarchitecture, cortical geometry, and only the largest of cortical pores in the distal radius and tibia of humans. Combining the use of longitudinal, synchrotron-based micro-CT imaging (39) with an appropriate animal model can enable the direct tracking of cutting cones *in vivo* to measure BMU progression. This is achieved by the use of a powerful technique known as phase contrast (40), which utilizes the structural properties within a sample to generate refraction of monochromatic, coherent synchrotron based x-rays (in contrast to absorption of x-rays with conventional micro-CT) when the object is placed a certain distance from the detector. The refraction of x-rays increases image contrast and thus effective resolution without the expense of high radiation dose. This technique significantly improves the detection and in turn, the 3D characterization of cortical porosity and BMU related resorption spaces. This platform will allow us to overcome the limitations associated with two-dimensional (2D) histological studies so we can assess the complex spatio-temporal behaviour of BMUs for the first time. Studying bone remodeling in this capacity will provide novel insight into how osteoclast function contributes to altering bone microarchitecture since bone remodeling dysregulation and variation lie at the root of osteoporosis. Additionally, this information will enable the improvement and advancement of therapeutic interventions aimed at targeting the OP disease pathway to minimize bone loss.

1.14. Animal Models of Cortical Bone Turnover

Animal models provide critical platforms for studies investigating factors affecting or regulating bone remodeling (41). Particularly, rabbits serve as excellent models to investigate BMU behaviour, since they are the smallest laboratory animal to exhibit cortical bone remodeling similar to that of humans, as compared to commonly used laboratory mice and rats, which exhibit little to no secondary osteons naturally (42-45). Rabbits also have good temperament, they exhibit faster bone turnover than primates, and they reach skeletal maturity within a relatively short period of time in comparison to larger animal models, at approximately 6 months old (46). Preliminary proof-of-principal studies conducted by our group have demonstrated the feasibility of directly tracking individual remodeling events in rabbit tibiae however, these studies revealed that remodeling rates in cortical bone of normal rabbits are low.

Furthermore, in general, remodeling rates are lower in cortical bone than to that of trabecular bone. In order for a cortical bone model to be operationally effective, there needs to be an increase in activation frequency (Ac.f) (47), which is the "birth rate" of new BMUs or the frequency with which remodeling is initiated in a given area of bone. Approaches focused specifically on cortical bone would establish a viable platform to study the coordination of remodeling events and its role in disease progression when utilized in longitudinal *in vivo* imaging studies. Parathyroid hormone is an encouraging and viable pathway for increasing the number of potential targets to study BMU activity from given its ability to stimulate bone remodeling.

1.2. Thesis Objectives

There exists a need for suitable animal models focused on cortical bone to enable the study of bone remodeling and its associated porosity. Thus, the primary objective of this thesis project was to develop an animal model system of elevated cortical porosity in the rabbit using PTH and utilizing micro-CT imaging and histomorphometry to characterize 2D and 3D changes in cortical and trabecular bone microarchitecture in the tibiae of PTH-dosed rabbits. This model system will be capable of tracking individual remodeling events using longitudinal synchrotron based imaging so that we can gain novel insight into the spatio-temporal behaviour of BMUs, the very structures involved in the generation of OP, and begin to address the significant knowledge gap surrounding bone remodeling dynamics and its role in the development of disease.

1.3. Organization of Thesis

The research described within this thesis focuses on the development of a rabbit cortical porosity model while exploring the effects of PTH on bone microarchitecture. The body of this thesis is organized into 3 chapters. Chapter 2 consists of a review of the current literature regarding PTH and its effects on bone, providing a rationale for its use in the current thesis project to elevate cortical bone porosity in rabbits. This chapter highlights the important role of the mode of administration of PTH on trabecular and cortical bone microarchitecture in animals and humans, and discusses some of the important mechanisms by which PTH induces its anabolic and catabolic effects in bone. This chapter concludes with a brief section on PTH effects in rabbit bone to segue into Chapter 3.

Chapter 3 consists of the main experiment involving the development of the PTH-dosed rabbit model. This research is one aspect of a larger study presented as a manuscript entitled "*Cortical Bone Porosity in Rabbit Models of Osteoporosis*" published in the Journal of Bone and Mineral Research. The manuscript begins with a recap on bone remodeling and animal models, reiterating the importance of developing a cortical bone turnover model before proceeding into the experimental manipulation of remodeling events. The manuscript aims to characterize 3D cortical porosity changes in the PTH dosed rabbit model in addition to several other rabbit-based models of OP (ovariectomy and glucocorticoid induced). Cortical bone microarchitecture is

compared amongst the models to determine the rabbit model best suited for future longitudinal *in vivo* imaging studies. These rabbit models were developed in parallel to minimize the need for control animals, minimize costs, and convenience. Another graduate student, Kim Harrison, characterized the other rabbit based models although, we both equally contributed to the experiment and the manuscript in its entirety. As such, we share joint first authorship on this manuscript.

Chapter 4 consists of a brief overview of Chapter 2 and 3 and the future directions of this thesis project, discussing potential avenues of research utilizing the PTH dosed rabbit model in order to better understand cortical bone remodeling. This chapter also contains some of the additional histological work I carried out during my research program as it contributes to future directions aimed at reproducing the classic histological measure of LER.

CHAPTER 2. Parathyroid Hormone Effects on Bone

2.1. Introduction

Parathyroid hormone, an endogenous hormone involved in calcium and phosphate homeostasis, acts on multiple organ systems to increase calcium levels in the blood when they are low. In addition to acting directly on the kidney and indirectly on the intestine to increase calcium uptake, PTH acts on the skeletal system by stimulating both bone resorption and bone formation, thereby increasing bone turnover overall (48). Parathyroid hormone acts directly on members of the osteoblast lineage through binding of the PTH-1 receptor and indirectly on osteoclasts to increase the number and activity of both cell types (49). Increased resorption is predominantly achieved through osteoblastic-mediated synthesis of the cytokine receptor activator of nuclear factor kappa-β ligand (RANKL), which binds to its receptor RANK on osteoclasts and osteoclast precursors, and by a decrease in osteoprotegerin (OPG), a decoy receptor inhibiting the action of RANKL, together increasing osteoclastogenesis (50). On the other hand, increased formation can be partly explained by elevations in osteoblast number through multiple mechanisms that modulate the function of osteoprogenitor cells, osteoblasts, osteocytes, and bone lining cells (51). The specific cellular and molecular mechanisms that underlie this increased formation are currently not fully understood. Interestingly, it has been shown that PTH imparts distinct effects on the skeleton depending on the amount of circulating PTH in the blood. Generally speaking, intermittent administration of PTH increases bone formation, resulting in a net gain in bone mass, whereas high circulating levels of PTH, as seen in patients of hyperparathyroidism or with continuous administration in animal studies, results in a net loss of bone mass (48). This review will focus on the dual action of PTH on bone, highlighting some of the pivotal work that has been carried out in animal (mice, rats, rabbits, dogs, monkeys) and human clinical studies, and offering several plausible explanations for the distinct outcomes observed with intermittent and continuous PTH dosing regimens and for the variation observed with some of the bone responses to PTH.

2.2. Intermittent PTH

Since the discovery of its anabolic properties on bone (52), intermittent PTH has been studied in basic and translational studies utilizing intact/normal and OP animal models, as well as in clinical studies. Repeated transient exposures of bone to PTH and its analogues, particularly the N-terminal fragment of the intact hormone (PTH (1-34)), the bioactive portion of the hormone, leads to bone apposition and thus, increased bone mass. Low, intermittent doses of the recombinant protein form of PTH (1-34), known as teriparatide, have been employed as one of the only clinical anabolic treatments indicated for OP in postmenopausal women (53-63), elderly men (61, 63, 64), pre-menopausal women with idiopathic OP (65), and patients with GC induced OP with high risk of fracture (66). Parathyroid hormone's anabolic capabilities have also been

exploited recently to stimulate and accelerate bone healing with bone grafts and implants in animal studies (67-70). The current literature has revealed intermittent PTH administration as promoting bone formation on trabecular, endosteal, and periosteal (the outer surface of a bone) surfaces, while increasing intracortical porosity in the axial and appendicular skeleton, although there is heterogeneity in terms of trabecular and cortical bone responses.

2.21. Intermittent PTH Effects in Trabecular Bone

In trabecular bone, intermittent PTH administration has been shown to increase BMD as assessed by dual-energy X-ray absorptiometry (DXA) and HR-pQCT within trabecular rich sites of animals (71-73), and postmenopausal women (55, 56, 59, 74-76). This increase in BMD is related to improvements in trabecular bone architecture, which is based on studies utilizing histology or various imaging modalities like standard computed tomography (CT), pQCT, HR-pQCT, and micro-CT. PTH increases trabecular bone volume (trabecular bone volume fraction; BV/TV) (55, 61, 67, 77-80), the number of trabeculae (trabecular number; Tb.N) (67, 74, 79-82), and the thickness of trabeculae (trabecular thickness; Tb.Th) (55, 78, 81, 83), and decreases the distance between trabeculae (trabecular separation; Tb.Sp) (67, 79, 80, 82), all contributing to the elevation of bone mass. In addition to improving trabecular microarchitectural parameters, trabecular strut analyses have revealed PTH also increases trabecular connectivity in animal models (68, 77, 79) and clinical patients (59). The improvement in trabecular bone microarchitecture contributes to the overall strength and stiffness of bone and renders it more efficient in bearing mechanical loads.

Bone formation is typically evaluated in bone biopsies by dynamic histomorphometry, which involves the assessment of dual fluorochrome labels administered at discrete time points *in vivo* prior to sacrifice. These parameters include mineralizing surface per bone surface (MB/BS), mineral apposition rate (MAR), and bone formation rate (BFR) which can all be measured on trabecular, endosteal, and periosteal surfaces as well as in intracortical osteons (84) (Figure 2.1). Mineralizing surface per bone surface describes the extent of mineralization on a bone surface at a particular time measured as the sum of the total extent of double label and half the extent of the single label, divided by the total bone surface. Mineral apposition rate represents the linear rate of new bone deposition, measured as the distance between two consecutive fluorochrome labels divided by the labelling period. When quantified in a longitudinal section of a BMU, this measure can be utilized to infer LER histologically (Figure 1.5) (28, 29). Bone formation rate is the amount of mineralized bone formed per unit time, calculated as the product of MAR and MS/BS. Bone formation in the trabecular compartment is reflected by increases in these histomorphometric parameters of bone formation (54, 57, 58, 62, 71, 77, 82, 83). Activation frequency, a fundamental measure of remodeling rate previously defined in Chapter 1, has also been shown to increase in trabecular bone (62, 63, 75, 83, 85), reflecting PTH's ability to elevate turnover rate in the trabecular compartment.

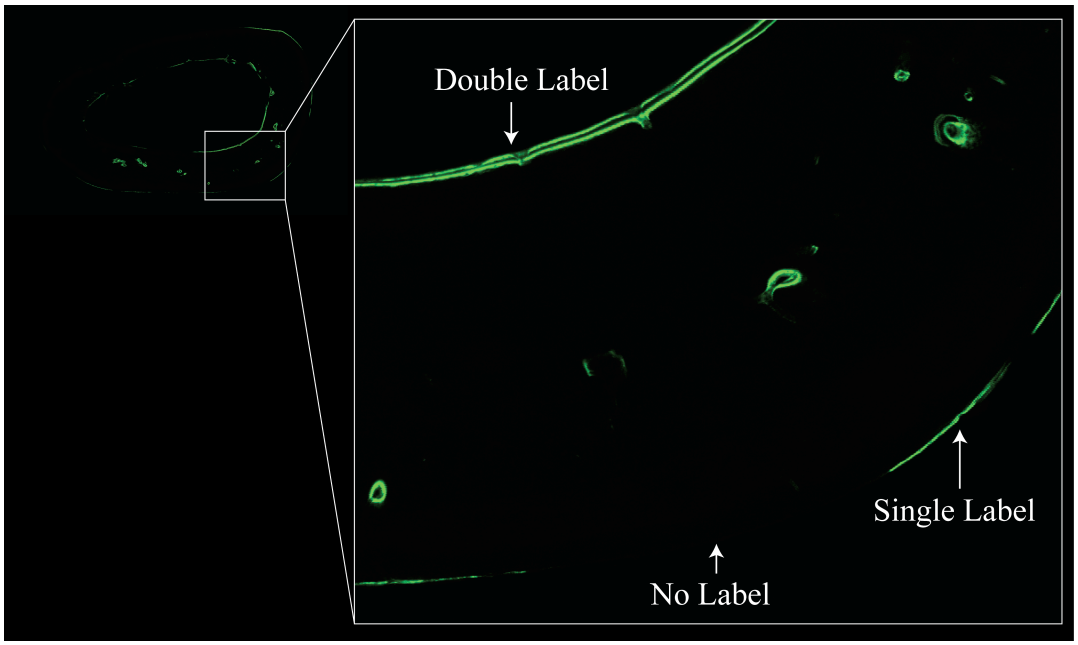

Figure 2.1. Confocal micrograph of a histological transverse section of cortical bone depicting fluorescent bone labels (green). Primary histomorphometric measures of bone formation activity can be quantified from these fluorochrome labels that appear on periosteal and endosteal surfaces and in intracortical BMUs. They can also be measured on trabecular bone surfaces. Mineralizing surface per bone surface (MS/BS) is measured as the full extent of double labelled bone surfaces plus half the extent of single labelled bone surfaces, normalized to the total bone surface. Mineral apposition rate (MAR) can be measured from double labelled surfaces as the distance between two fluorochrome labels divided by the time between label administrations. Bone formation rate (BFR) can then be calculated as the product of these two parameters.

Not all studies evaluating intermittent PTH have found increases in trabecular bone formation as some groups have reported a lack of change in Tb.Th (71, 80, 82), and one study reported decreases in BMD, Tb.N, and BV/TV within the radius of postmenopausal women with OP treated with 20 μg/day PTH for 18 months (53). This variation in responses may be explained by a number of reasons. The lack of change in Tb.Th may have been a result of resorption occurring within the trabeculae, as several groups have reported trabecular tunnelling, with intermittent PTH doses (55, 79, 80, 85, 86). This resorption would divide existing trabeculae that were initially thickened by bone accrual early in treatment, which could explain the increase in Tb.N typically reported in these studies. Trabecular tunnelling does however, seem to occur with the administration of high PTH doses (55), with continuous PTH administration (78), and with long, extended courses of treatment (79, 80), therefore it is not clear if tunneling is the result of excessive resorption or occurs as an adaptive response to PTH

associated trabecular thickening. The dose and timing of PTH may also be a factor in the varying trabecular outcomes seen with intermittent PTH, as significant increases in Tb.Th seen after 35 days of PTH dosing in rabbit lumbar vertebrae were diminished after 70 days (83). It is not clear if this diminished effect was a result of trabecular tunneling since Tb.N was not assessed in the study. Similarly, in a longitudinal, prospective clinical study, Hansen and colleagues found Tb.N to be increased in postmenopausal women after 6 months of daily PTH treatment at a 20 μg dose but this decreased with continued treatment at 18 months (74). Dose frequency of PTH may also influence trabecular outcomes as Yamamoto and colleagues found that more frequent dosing of PTH (up to 4 times per day) resulted in thinner trabeculae in the mouse femoral metaphysis while less frequent, once daily dosing of PTH resulted in thicker trabeculae (67). Variation in trabecular outcomes with intermittent PTH may also be related to the site of study. Anabolic effects of PTH are evident in skeletal sites rich in trabecular bone such as the iliac crest, lumbar spine, femoral neck, mandible, and proximal tibia, but not in the middle or distal radius (55, 73, 74). One study reported reductions of BMD in the distal radius of postmenopausal women treated with daily PTH (20 μg) for 18 months (74). The lack of bone formation at the radius may be due to its tissue composition, as these regions are rich in both cortical and trabecular bone, however it is not clear why these bone site specific differences exist.

2.22. Intermittent PTH Effects on Endosteal and Periosteal Surfaces

On endosteal and periosteal surfaces, PTH induces similar effects to that of trabecular bone, stimulating bone apposition as revealed through histomorphometric fluorochrome labelling studies on bone biopsies. Increases in MS/BS (57, 58, 87), MAR (57, 58, 71, 83, 85, 88), and BFR (57, 58, 71, 83, 85, 88) have been reported on one or both surfaces. Formation generally occurs to a greater extent on the endosteal surface than that on the periosteal surface (58, 71). This is probably due to the fact that the adjacent vascular marrow cavity readily provides a rich source of cells. The significant mineralization of these surfaces is associated with changes in cortical geometry demonstrated by increases in cortical thickness (Ct.Th) (55, 59, 74, 75, 79, 87-89), cortical area (Ct.Ar) (71, 87, 88), and total area (Tt.Ar) (71, 74, 88). While some groups have reported decreases in marrow area (Ma.Ar) (88), others have found no changes in this parameter (71, 87). These data indicate bone is forming on both surfaces, and this accrual of bone may contribute to elevations in BMD (83). As indicated in trabecular bone focused experiments, differences in cortical geometry outcomes may be specific to certain bone sites. Despite a reduction in BMD in the radius, total area was slightly elevated in postmenopausal women treated with daily PTH (20 μg) for 18 months but no change was observed in the tibia (74). Within this study, it was unclear whether the increase in area was due to bone apposition or related to the HR-pQCT methodology where the region of interest between baseline and follow-up scans was determined by a common region matching procedure which assumes constant area over time. It may be the case that the imaging methodology employed introduced an additional variable into bone architectural analysis and therefore, the apparent variation observed may not be accurate.

2.23. Anabolic Effects & Timing

The magnitude of the anabolic effects induced on bone surfaces by PTH not only depends on mode (intermittent *vs.* continuous) and dose (low *vs.* high), but also on the length of PTH administration and the time within the course of the treatment that the bones are analyzed (early *vs.* late in treatment). It has been shown that low intermittent dosages of PTH stimulate bone formation early in treatment, as evidenced by an early rise in bone formation markers, followed sometime thereafter by a rise in both bone formation and resorption markers (62). If bone markers reflect physiological actions, then it is likely from these studies that modeling based bone formation, formation that occurs in the absence of resorption, predominates at this early stage, with the proportions of remodeling based bone formation to modeling based formation increasing with long term intermittent PTH treatment (54, 63). Modeling based bone formation has been reported in several human clinical (57, 58, 63, 90) and animal (91) studies as revealed by histological staining of cement lines. Lindsay and colleagues found that bone formation induced by PTH was 70% remodeling based and 30% was modeling based within the iliac crests of postmenopausal women with OP treated with PTH for one month in comparison to age-matched controls which exclusively exhibited remodeling based bone formation (57). The time frame for which PTH is maximally anabolic is termed the "anabolic window" and occurs within the first 9-12 months of clinical PTH treatment (92-94). Long term PTH administration is associated with declining anabolic effects, which may be related to the level of the protein Dickkopf-1 (DKK1), a potent regulator of osteoblast activity. Increasing serum levels of DKK1 have been shown to be associated with a decrease in bone formation markers in postmenopausal women after receiving daily PTH (20 μg) for 18 months, although levels of these markers were still significantly higher than baseline (95). The proportion of remodeling to modeling based bone formation may also be dependent on dosing frequency as Yamamoto and colleagues found that the modeling based bone formation prevalent on quiescent trabecular surfaces within the femoral metaphysis of mice treated with once daily PTH was diminished with increased administration of PTH, of up to 2-4 times per day, which probably favoured bone remodeling (67).

Modeling based bone formation not only occurs on previously quiescent bone surfaces but also on existing, actively remodeling BMUs where modeling based bone formation "spills over" onto quiescent surfaces (57, 58, 90). In a quadruple bone fluorochrome labeling study, modeling was observed in hemi-osteons within trabecular and endosteal bone of postmenopausal women treated with PTH for one month. Hemi-osteons were classified based on the characteristics of their cement lines and collagen fiber orientation. As such, structures were termed remodeling hemi-osteons, modeling hemi-osteons, and mixed modeling-remodeling hemi-osteons (90). Within mixed modeling-remodeling osteons, the mineralized perimeter (the second double fluorochrome bone label) increased in length indicating bone formation extended beyond the original boundaries of the scalloped cement line onto adjacent, previously unresorbed quiescent surfaces (58). As a result of this "overfilling", trabecular and endosteal hemi-osteonal wall thickness increase, demonstrating PTH's ability to induce a positive bone balance (90).

Overall, the early mechanism of anabolic action of PTH is the initiation of bone remodeling based bone formation as well as modeling based bone formation.

2.24. Cellular Mechanisms of Bone Apposition

At the cellular level, the extent of bone formation is largely determined by the number of osteoblasts, which in turn, is determined by the rate of replication of osteoblast precursors and the life span of mature osteoblasts. A significant proportion of the anabolic effects of intermittent PTH on trabecular, endosteal, and periosteal surfaces are mediated by increases in osteoblast number. Osteoblasts have 3 fates: to become osteocytes encased by mineralized bone, to become quiescent bone lining cells, or to undergo apoptosis. Amplification of osteoblast number by intermittent PTH has been associated with increases in the differentiation of osteoblast precursors (96, 97), the survival of osteoblasts (98-100), and the mobilization of bone lining cells (101). Several cellular mechanisms have been proposed which mediate these anabolic effects involving increases in growth factors (insulin like growth factor 1 (IGF-1), transforming growth factor-β (TGF- β), and bone morphogenic proteins), which increase the differentiation and survival of osteoblasts, increase in the expression of runt-related transcription factor 2 (Runx2), a transcription factor involved in the regulation of osteoblast differentiation and survival of osteoblasts, and activation of mammalian homologue of wingless-related integration site in drosophila (Wnt) signalling, which regulates osteoblast proliferation and differentiation (51). Apposition on bone surfaces may also be achieved by increases in angiogenesis (102) and through osteocyte mediated sclerostin inhibition (103, 104), as the glycoprotein is known to inhibit bone formation. These are just a few of the notable pathways involved in the vast signalling network activated by PTH therefore, further investigation is required to fully understand and appreciate PTH's anabolic effects.

The mechanisms noted above appear to affect trabecular and cortical bone compartments to different extents, which may explain some of the differences observed on the bone surfaces with intermittent PTH administration. For instance, Jilka and colleagues found that the predominant mechanism of osteoblast number increase in trabecular bone was through the attenuation of osteoblast apoptosis, which they studied in PTH treated transgenic mice vertebrae (100). On the periosteal surface, this mechanism did not substantially contribute to the increase in osteoblast number since the rate of osteoblast apoptosis was low in that region and therefore, did not have much of an effect. The increase in osteoblast number on the periosteal surface was accounted for by the increase in the differentiation of osteoblast precursors (100). The increase in osteoblast number on the periosteal surface is further elevated by the reactivation of bone lining cells. In an *in vivo* lineage tracing study, PTH increased osteoblast number by converting bone lining cells to active osteoblasts on the quiescent periosteal surfaces of calvaria (parietal bones) in transgenic mice treated with 80 μg/kg PTH for 3 days (101). This reactivation of bone lining cells into mature osteoblasts is one of the primary mechanisms underlying modeling based bone formation seen early in intermittent PTH treatment. These studies suggest that skeletal compartment (trabecular, endosteal, periosteal, intracortical) specific responses to intermittent

PTH may be a result of osteoblast progenitors responding differently to PTH, although there may be many cellular mechanisms at play.

2.25. Intermittent PTH Effects on Intracortical Bone

Despite increases in bone formation on trabecular, endosteal, and periosteal surfaces, intermittent PTH has been shown to increase cortical porosity (Ct.Po) assessed using histology (55, 71, 79, 87, 105), HR-pQCT (53, 74), and more recently, *ex vivo* conventional micro-CT (89, 106) within the appendicular skeleton. Cortical porosity has also been reported in the outer shell of the iliac crest of postmenopausal women (54), and in the rib of dogs (85). This increase in porosity is due to PTH's ability to increase bone remodeling in cortical bone as evidenced by an increase in Ac.f (71, 79, 83, 87). PTH has also been shown to increase bone formation intracortically by increasing osteonal MAR (On.MAR) (63, 87) and BFR (71, 79, 87). There is concern that high proportions of intracortical porosity would increase the risk of fragility and therefore fractures in OP patients, but animal and clinical studies have demonstrated intermittent PTH preserves (74, 83, 87, 89, 91) and even improves (71, 79, 105) bone strength in long bones. It has also been reported that intermittent PTH reduces incidences of vertebral (56, 66) and non-vertebral (56, 107) fractures in populations of OP patients. This maintenance of bone strength imparted by intermittent PTH can be explained by two possible reasons. First, it may be that intracortical porosity is compensated by increases in cortical geometry through endosteal and periosteal bone apposition thereby limiting negative biomechanical impacts. A key determinant of bone strength is its geometry, or the bone's overall size and shape. Bone strength is also dependent on the amount of bone present. Small increases on the periosteal surface of bones especially improves strength since the diameter of a bone is proportional to the moment of inertia, or the bending resistance of bone (108). Hirano and colleagues found the cross sectional moment of inertia to be increased despite a 3.8% increase in Ct.Po in tibiae of rabbits treated with 40 μg PTH/kg/5 days a week for 140 days. The gain in strength was associated with an increase in Tt.Ar (105). Similarly, an increase in Ct.Po and Ct.Ar in the humerus of OVX cynomolgus monkeys treated with 5 μg PTH/kg/day for 18 months did not have an effect on extrinsic mechanical parameters (ultimate load, stiffness, work to failure) in comparison to OVX controls (87). This outcome has also been reported clinically, as Hansen and colleagues found bone strength, estimated by finite element analysis, to be preserved in the radius and tibia of postmenopausal women with OP treated with daily PTH (20 μg) for 18 months despite reporting increases in Ct.Po (74).

The second reason bone strength may not be negatively impacted by PTH despite elevations in intracortical porosity is that the porosity frequently exhibits a non-random distribution throughout the cortex, predominantly occupying the region near the endosteal surface (83, 87, 91, 105, 106, 109, 110). This distribution of pores in this region aids in offsetting the negative impact of increased intracortical porosity on biomechanical strength, since the loss of bone is closest to the bone's neutral axis of bending (87, 105), which minimizes the risk of fracture by modulating the impact on the resistance to bending and torsional loads (108).

Localization of pores within certain regions along the endosteal surface may further contribute to offsetting potential biomechanical impacts as porosity was seen to be localized within anteromedial and posterolateral sites of the tibia in rabbits treated with 40 μg PTH/kg/day for 4 weeks (89). This pattern occurs within cortical bone of larger animal systems and humans, however, porosity was pronounced near the endosteal surface in the tibiae of rats (109), a species known to generally exhibit little to no spontaneous cortical remodeling. The pores observed in these rats were likely not "true" intracortical pores as they were continuous with the medullary cavity. Furthermore, in rats, it may be the case that this phenotype only occurs with exposure to high circulating levels of PTH, since within the same study, porosity was non-existent in rats treated with intermittent PTH. This raises the question whether PTH-driven species-specific cellular mechanisms involved in the development of cortical porosity are at play. The non-random distribution of porosity accompanied by geometrical changes of cortical bone may be part of the explanation as to why the integrity of the bone's biomechanical properties were maintained, despite elevations in intracortical porosity. These effects are particularly important in bones of the appendicular skeleton since they withstand high mechanical loads. Further investigation into the impact of cortical porosity and geometry by PTH on biomechanical properties of cortical bone is certainly warranted.

Overall, the literature has shown intermittent PTH stimulates bone apposition on trabecular, endosteal, and periosteal surfaces while increasing intracortical porosity. Increased intracortical porosity is primarily due to elevated remodeling while bone surface apposition is due to increased remodeling (with a net positive balance) in addition to early modeling based bone formation. The precise cellular and regulatory mechanisms that initiate these actions on the skeletal envelopes are largely unknown and warrant further study.

2.3. Continuous PTH Effects on Cortical and Trabecular Bone

While intermittent PTH accelerates bone turnover creating a net positive bone balance, observations of patients with hyperparathyroidism and animals receiving continuous PTH administration (delivered via osmotic pumps), show that PTH at sustained elevated levels induces predominantly catabolic effects in bone. This is a consistent finding for only cortical bone as the effect in trabecular bone is controversial. In cortical bone, continuous infusions of PTH result in increased Ct.Po (111, 112), decreased BMD (112, 113), and thinner cortices (114, 115) as bone resorption in elevated on the endosteal surface. One study in rats found Ct.Ar to be maintained and accompanied by increases in mineralization on the endosteal and periosteal surfaces and no deleterious effects on bone strength (111). It is worth noting that the clearance from serum of biologically active PTH may play a role in its effects on bone, which in turn can influence the significant changes observed, since some species may metabolize the hormone more quickly than others. Parathyroid hormone clearance in rats is approximately 1 hour after subcutaneous PTH injection (82), whereas PTH clearance in humans is approximately 4 hours (116), although this may be altered by a number of factors including age and health. One should consider the role that species-specific physiological mechanisms play in pharmacokinetics and

therefore, PTH administration should to be adjusted in animal studies accordingly to better mimic the PTH dose delivered clinically.

In trabecular bone, there is a lack of consensus on the effects continuous PTH has in this bone compartment. Some studies in patients with PHPT and in animals receiving continuous infusions of PTH have indicated preservation and apposition of trabecular bone with continuous PTH (78, 82, 109, 111, 114, 117), while others have reported losses of trabecular bone mass (81, 112, 115). One group even found improvements in trabecular architectural parameters (increase in BV/TV, Tb.N, and decrease in Tb.Sp) within PHPT patients (114). In those studies reporting apparent maintenance or increases of trabecular bone, pronounced mineralization was observed (78, 111, 117) indicating prevalent bone formation. Conversely, at high doses, some have reported the appearance of woven bone (78, 111) and trabecular tunnelling (78) in trabeculae of rats receiving osmotic infusions of PTH. In some instances, continuous infusions of high dose PTH in rats have even resulted in high rates of hypercalcemia as a result of elevated bone resorption and death (81, 82). Variation in trabecular bone outcomes in response to continuous PTH may be related to the relative amount of trabecular bone present at the skeletal site, as similarly observed with intermittent PTH. This is illustrated by a study of PHPT patients where losses of bone were observed to have occurred in a cortical and trabecular bone rich site, the radius, while the trabecular bone-abundant lumbar vertebrae was maintained, and the femoral neck, which has a mixed composition of cortical and trabecular bone, had an intermediate effect (113). Interestingly, Uzawa and colleagues found losses in the rat tibial diaphysis and epiphysis with infusions of 2.14 ng/hr or 214 ng/hr PTH for 4 weeks, but increases in trabecular bone volume (BV/TV) in the tibial metaphysis (78). It is important to note that the morphology of trabecular bone at this site in rats was abnormal. Despite its apparent preservation, abnormal trabecular morphology can negatively impact the quality of bone, which in turn affects the overall bone strength in that compartment.

The apparent maintenance of trabecular bone in PHPT patients may be an artificial result as many of the imaging modalities utilized to measure bone microarchitectural outcomes in clinical studies (ie., DXA) do not distinguish between cortical and trabecular bone compartments. In a HR-pQCT study of cortical and trabecular bone in 43 PHPT patients (male and female, mean age 63 years old), Vu and colleagues speculated that remodeling near the endosteal surface results in both the development of porosity intracortically and the erosion of the endosteal surface, together creating structures resembling trabeculae and thus, enlarging the medullary cavity. These “cortical remnants” are usually included in the quantification of trabecular BMD as these are not distinguishable from true trabeculae with standard imaging modalities and therefore, there is an overestimation of trabecular BMD (112). It should be noted that the “trabecularization” of the cortex is associated with advancing age (21) therefore, it may be the case that several mechanisms of bone loss contributed to the thinning of cortices in PHPT subjects. The degree to which this effect occurs in animals or younger PHPT patients remains to be elucidated.

The periodicity of PTH administration, intermittent *vs*. continuous, is one of the prevailing factors that determine the outcome in cortical and trabecular bone, and the current literature has overwhelmingly supported this. It has been suggested that the two modes of administration regulate different sets of genes as indicated by gene expression profiling (118) although many additional mechanisms may also be at play. Some of the cellular mechanisms that contribute to these differences involve relative levels of Runx2 and RANKL/OPG. With regards to the former, intermittent PTH has been shown to temporarily decrease Runx2 protein levels, thereby repeatedly delaying osteoblast apoptosis with each exposure. Runx2 mediated transcription of pro-survival genes by intermittent exposures of PTH is short lived because of subsequent feedback inhibition back on PTH which then stimulates the degradation of the transcription factor. In an *in vitro* study, a continuous infusion of PTH on cultured osteoblast cells was shown to decrease Runx2 protein levels below a critical threshold needed to sustain the anti-apoptotic signalling, thereby terminating the pro-survival effect on osteoblasts, while intermittent PTH levels increased Runx2 levels transiently (98). The duration of the anti-apoptotic effects of PTH appears to be dependent on the protein level of Runx2, which illustrates the importance of employing intermittent PTH to stimulate bone formation. As shown *in vivo* and *in vitro*, continuous PTH circulation has also been shown to prolong and sustain the expression of RANKL levels while inhibiting OPG, thereby increasing osteoclast differentiation and lifespan and promoting bone resorption (119, 120). Under intermittent conditions, PTH only induces a transient change in RANKL and OPG (119) or no alteration at all (120). While the increase in resorption can be partially explained by these pathways, the catabolic and anabolic effects of PTH likely involve many signalling pathways and cells and the current knowledge of these mechanisms are limited and require further investigation.

2.4. PTH Effects on Rabbit Bone

The rabbit has been an important laboratory animal model for assessing PTH affects on bone, since its cortical bone undergoes remodeling similar to that of humans and it responds remarkably well to PTH. The rabbit has been a better model system to assess bone ingrowth into implants and with bone grafts because their bones are greater in size than that of mice and rats. These studies have utilized PTH's anabolic effect to promote bone healing and the incorporation of implants and grafts into bone (67-70). As discussed in sections 2.21 - 2.25, intermittent dosages of PTH have been shown to increase intracortical porosity while stimulating bone apposition on trabecular, endosteal, and periosteal surfaces in the rabbit, albeit there is variation within some bone microarchitectural outcomes (71, 83, 89, 91, 105, 106). Within cortical bone, improvements in bone geometry induced by PTH have been shown to maintain and even strengthen cortical bone despite elevations in intracortical porosity (71, 83, 105). Currently, information regarding the effect of continuously high circulating levels of PTH on rabbit bone is limited, being reported in only two studies (121, 122). Within these studies, PHPT was experimentally induced in rabbits using a high phosphate diet, and the presence of the disease was confirmed by histopathological analyses of the parathyroid glands, kidney, and bone. While

bone fibrosis was noted, these studies did not extensively characterize cortical or trabecular bone microarchitectural changes in these rabbits. Future studies are needed to optimize rabbit models of PHPT, particularly with respect to bone microarchitecture.

Much of the work that has characterized changes in cortical and trabecular bone microarchitecture due to intermittent PTH in the rabbit have employed standard static histology and dynamic histomorphometry. Recently, several groups have utilized desktop micro-CT to investigate the effects of PTH dose frequency on cortical bone microarchitecture in rabbits (89, 106). These studies imaged rabbit bone with an isotropic voxel size of 15-20 μm. It would be beneficial to image rabbit cortical bone at a higher spatial resolution in order to acquire more 3D information on its porosity so that we can better understand how PTH affects bone remodeling. Given that PTH has well-documented effects on cortical bone in the rabbit, the hormone can be employed to increase intracortical porosity in animals that typically have low levels of bone turnover to establish a viable model system that is currently lacking in the literature.

2.5. Conclusion

Overall, PTH is a potent stimulator of bone remodeling in cortical and trabecular bone. Intermittent PTH increases bone formation, thereby increasing bone mass and improving microarchitecture. Conversely, excess PTH shifts remodeling to increased resorption rather than formation leading to the deterioration of bone microarchitecture. Variation does exist in trabecular and cortical bone's response to PTH. Parathyroid hormone increases porosity in larger animals capable of remodeling their bones and humans with both modes of administration by initiating new remodeling events and increasing the rate of remodeling. Parathyroid hormone can therefore be utilized to increase cortical bone remodeling in animal model systems with low rates of bone turnover, like in the rabbit tibiae, as mentioned in section 1.4, to maximize the number of potential targets to study BMU activity from within a small section of bone using *in vivo* high-resolution longitudinal imaging. Intermittent PTH can increase the number of new BMUs in cortical bone while minimizing adverse effects associated with high circulating levels of the hormone (ie. hypercalcemia) and even offer benefits like bone apposition on the trabecular, endosteal, and periosteal surfaces to offset potential detrimental effects on bone strength. For this reason, PTH was employed in my thesis project to establish a cortical bone model in the rabbit, providing a platform for the study of bone remodeling and associated cortical porosity.

CHAPTER 3. Cortical Bone Porosity in Rabbit Models of Osteoporosis

This chapter consists of the manuscript entitled "*Cortical Bone Porosity in Rabbit Models of Osteoporosis*" published in the Journal of Bone and Mineral Research. The manuscript aims to describe 3D cortical porosity changes in the PTH rabbit model in addition to several other rabbit-based models of OP (ovariectomy and glucocorticoid induced), which have been characterized by Kim Harrison (doctoral student). As Kim and I have equally contributed to the work presented in this manuscript, we share joint first-authorship. Contributions to the manuscript have also been made by the following co-authors: Arash Panahifar, Amir Ashique, Janna Andronowshi, Gavin King, Kurtis Swekla, Terra Arnason, Peter Pivonka, and David Cooper. The discussion of data within this manuscript has been written to adhere to the guidelines set by the Journal of Bone and Mineral Research such that results are reported to reflect a more thoughtful interpretation of all the data presented and avoid dichotomous use of the *p* value. This manuscript is a previous revision to the accepted version online and has been reformatted for inclusion in this thesis.

3.1. Introduction

Globally, 200 million people live with OP (123), which places significant burdens on health care systems worldwide. Assessment of osteoporotic bone loss has classically focused on bone mass and density at common fracture sites such as the hip, wrist, and lumbar vertebrae; however, there is growing recognition of the role of microarchitecture in bone deterioration and fragility (124). This trend has been driven by advances in imaging which have enabled assessment of microarchitecture – particularly for trabecular bone. More recently, imaging approaches to assess cortical bone microarchitecture (porosity) have emerged for both preclinical (animal model) and clinical assessment (33, 125), creating the potential to move beyond what has been termed a 'trabeculocentric' view of bone loss (126). Indeed, the majority of the appendicular skeleton is comprised of cortical bone which suffers from significant losses associated with age (18, 126, 127). Moreover, 80% of all fractures occur at sites of weakened, thinned cortical bone (19, 20). As recently reviewed, cortical bone porosity is associated with the mechanical strength of bone and is negatively related to material stiffness, toughness, and the capacity of bone to absorb impact (125).

An increase in cortical porosity, at the scale of vascular pores (e.g. osteonal/Haversian canals and associated resorption spaces), is a physical manifestation of bone loss that arises as a result of an imbalance in cortical remodeling with bone resorption outweighing bone formation. Remodeling, in the strict sense that Frost defined, refers only to the creation of secondary tissue (turnover) in either cortical or trabecular bone. The cells responsible for an individual remodeling event are referred to as a BMU (4). Basic multicellular units are activated on bone surfaces, leading to the replacement of cylindrical packets (secondary osteons) in the cortex and

trench-like packets (hemi-osteons) in trabecular bone (8). Within cortical bone, BMUs are classically depicted as consisting of an osteoclastic cutting cone which creates a tunnel-like resorption space followed by an osteoblastic closing cone. A reversal zone separates them, but the two processes are spatially and temporally 'coupled' (128, 129) and continued resorption has been demonstrated in this "reversal-resorption" phase of the BMU (130). Imbalance with resorption outweighing formation within individual remodeling events is the underlying mechanism by which cortical porosity increases with age and/or disease. Increases in cortical porosity may be either a product of increased rate of remodeling, where formation lags behind resorption (131) also referred to as "transient remodeling spaces" (132), or through "uncoupling" where there is an arrest during the reversal phase of the BMU (133-135). Strategies for the prevention and/or reversal of OP ultimately must seek to augment the balance between resorption and formation within individual BMUs and not simply the cessation of remodeling as reflected by the growing body of literature on the side-effects (e.g., osteonecrosis of the jaw, atypical fractures) of some anti-resorptive therapies for OP - mainly bisphosphonates, but also recently reported for Denosumab (136-140). High-resolution pre-clinical imaging of the resorptive phase of individual BMUs holds great promise for novel spatial-temporal assessment of BMU regulation, both *ex vivo* (141) and even *in vivo* (33, 39).

Given that cortical bone porosity is intimately linked with the remodeling process, is of clinical relevance, and presents an increasingly accessible target for imaging, there is a growing need for suitable animal models of OP to advance our understanding of how cortical porosity develops and how it is impacted by countermeasures. Inter-species variation in cortical microarchitecture can, however, limit the utility of common animal models. The cortical bone of larger vertebrates, including humans, tends to be dominated by secondary bone that is generated by remodeling while smaller species (mammals under 2 kg (142)), including mice and rats exhibit little, if any, cortical turnover and thus retain primary vascular canals throughout their lives (42, 43, 45, 143, 144). Because of this, the American Food and Drug Administration (FDA) recommends the use of larger animals which remodel their cortices in addition to the common OVX rat model for OP studies (145). Notably, larger species including rabbits, sheep, goats, dogs, and swine have all been employed in OP research (42, 43, 45, 144). Here we focus on the rabbit, the smallest commonly employed laboratory animal with well-defined spontaneous cortical remodeling similar to humans (44, 146, 147). Rabbits also have the advantage of a remodeling period that is shorter than larger animal models, a relatively rapid skeletal maturation (by 6–9 months) (148, 149), and they are known to respond to PTH treatment with elevated remodeling and cortical porosity (71, 105, 106, 150). Taken together, these characteristics make the rabbit a promising platform for OP studies which is well suited for potential *in vivo* imaging (151) in future studies.

Animal models of OP generally focus on OVX to simulate post-menopausal decline in estrogen. In rabbits, however, the efficacy of this model is uncertain. OVX alone has been reported by several groups as ineffective at inducing OP in the rabbit (152-154), while others, conversely, have reported significant reductions in BMD (155-158). The efficacy of the rabbit

OVX model for induction of cortical porosity, in particular, is uncertain as existing studies have primarily focused on trabecular bone. The administration of GC either alone or, more commonly, in combination with OVX (OVX+GC) is a proven approach for inducing trabecular (152-154, 159-162) and cortical geometry/density changes (153, 161) in the rabbit. That said, the impact of GC alone on cortical bone porosity in the rabbit has not yet been assessed and cortical porosity outcomes for OVX+GC have only recently been explored (163). Rabbit OP models hold great potential as platforms for advancing our understanding of cortical remodeling and associated porosity; however, this potential can only be realized by filling these gaps in the literature.

Our primary objective was to characterize 3D cortical bone porosity changes in rabbit models of OP (OVX, GC, and OVX+GC) at the distal tibia using *ex vivo* micro-CT. Via correlative histomorphometry, we sought to test the hypothesis that cortical remodeling is elevated by these treatments relative to sham OVX controls (SHAM). Our secondary objective was to compare these changes with those caused by PTH, a known inducer of elevated intra-cortical remodeling and porosity in the rabbit. Finally, we sought to characterize 3D trabecular bone changes in the proximal tibia across these groups to enable assessment of changes in different bony compartments and to facilitate comparison with the more extensive literature pertaining to trabecular bone.

3.2. Materials and Methods

3.21. Animals

All animal work was approved by the University of Saskatchewan's University Animal Care Committee and adhered to the Canadian Council on Animal Care (CCAC) guidelines for humane animal use. Thirty-five skeletally mature, 6-month old (3.7-3.9 kg), female New Zealand White rabbits were acquired from a commercial supplier, Charles River Laboratories (Quebec, Canada). Animals were housed individually in stainless steel rabbit racks in the University of Saskatchewan's Health Sciences Laboratory Animal Services Unit, a CCAC accredited facility. Room temperature and humidity were controlled by a computerized system and the light cycle was maintained at 12:12 (12 hours of dark and 12 hours of light). Standard rabbit chow (Hi-Pro Feeds, Trouw Nutrition Canada Inc., Sherwood Park, Alberta, Canada) and reverse osmosis water through an automated watering system were provided *ad libitum*. Animals were acclimatized for a minimum of 7 days before any experimental procedures commenced.

The rabbits were randomly divided into 5 groups of 7 animals each: SHAM, OVX, GC, OVX+GC, and PTH. The OVX and OVX+GC group underwent bilateral ovariectomy whereas the SHAM, GC, and PTH groups underwent bilateral sham OVX surgery. Fifty-six days (8 weeks) post OVX/SHAM surgery (pre-dosing period), the GC groups (GC and OVX+GC) received Methylprednisolone Sodium Succinate (Pfizer, Kirkland, Quebec, Canada) by daily subcutaneous injection of 1.5 mg/kg for 4 weeks and the PTH group was dosed by daily subcutaneous injection for 4 weeks with human PTH (1-34) (Alfa Aesar, Ward Hill, MA, USA) at a concentration of 30 µg/kg (dosing period). The PTH dose used was intermediate to what has

been utilized in recent studies analyzing the effects of PTH dosing regimens (10 μg/kg/day *vs*. 40 μg/kg/day) on rabbit cortical bone (106, 150). The GC dose used was an intermediate-to-high dose (0.5 mg/kg/day *vs*. 1.0 mg/kg/day *vs*. 2.0 mg/kg/day) based on a previous study analyzing OVX and OVX+GC OP models in the rabbit (152). SHAM and OVX received daily subcutaneous injections of 1 ml saline for the corresponding 4 week dosing period. Dose initiation at 8 weeks post-surgery was selected based upon previous studies that found conflicting BMD results in relation to time (4, 6, or 8 weeks) post OVX (152, 154, 162). Each animal was monitored daily at the time of injection, as well as weekly to assess weight. The bone labelling fluorochrome calcein (Sigma Aldrich, St. Louis, Missouri, USA) was administered by subcutaneous injection at a dose of 10 mg/kg on days 13 and 14 (label 1) and days 27 and 28 (label 2; end-point) of the treatment period to facilitate dynamic histomorphometry. Animals were euthanized by intravenous injection of pentobarbital sodium (Euthanyl; Bimeda-MTC, Animal Health Inc, Cambridge, ON, Canada) at a dose of 0.4 ml/kg. Post-euthanasia, the right tibiae were removed and fixed in 10% formalin.

3.22. Micro-CT Analysis

The distal diaphysis and proximal epiphysis (Figure 3.1 C & A) were imaged with a SkyScan 1172 desktop micro-CT scanner (Bruker, Belgium) to assess cortical porosity and trabecular morphology, respectively. CTVol (version 2.3.2.0; Bruker, Belgium) was used to generate 3D volumetric renderings of cortical porosity and trabecular bone morphology. For cortical porosity analysis, a Volume of Interest (VOI) along 1 cm of the diaphysis, beginning 3 cm proximal the distal end of the tibia, was scanned (Figure 3.1 C) at 75 kVp, 133 μA with 460 ms exposure, 0.2º rotation step, 4-frame averaging, and a 0.5 mm aluminum filter. Resolution dependency of micro-CT analysis has long been recognized for both trabecular bone morphology (164) and cortical bone porosity (5). Here we chose a nominal resolution (voxel size) of 10 μm to specifically target cortical porosity on the scale of remodeling-related resorption spaces/osteons (~100 μm in rabbits (165)) with smaller spaces (including primary canals, mature secondary osteonal canals, osteocyte lacunae, and canaliculi) falling below the spatial resolution (Supplemental Figure 3.81). It should be noted that our resolution was higher (smaller voxel size) than that of micro-CT protocols previously applied to rabbit cortical bone (14-19 μm) (106, 150, 154, 163). Important considerations for future study included that the 10 μm voxel size is similar in scale to that potentially available *in vivo* (33, 39) and the distal hind limb of the rabbit is well suited for live imaging with the animal in an upright position (151). We validated our 3D micro-CT outcomes through comparison with 2D histological measures of osteon size, confirming correlation between the approaches and similar distributions of values from each (Supplemental Figure 3.82). Finally, the distal tibia represents a region of elevated porosity relative to the mid-diaphysis (Supplemental Figure 3.83) consistent with observations of elevated remodeling distally in lower limb elements (166).

For trabecular analysis, the proximal epiphysis of each tibia was scanned (Figure 3.1 A) at 75 kVp, 133 μA with 1080 ms exposure, 0.2° rotation step, 4-frame averaging, and a 0.5 mm

aluminum filter at a voxel size of 13 µm. The trabecular envelope within the entire epiphysis proximal to the growth plate was segmented as the VOI (Figure 3.1 A). The epiphyseal subchondral trabecular bone was targeted for both consistency with the existing literature (152, 161) and the fact that little trabecular bone was present in the metaphyses of the rabbits (Figure 3.1 A).

Micro-CT data were reconstructed using the NRecon software package (Bruker, Belgium) and quantitative 3D analysis was conducted with CTAnalyser (CTAn; version 1.16.4.1; Bruker, Belgium). To assess changes in cortical bone microarchitecture, Ct.Po (%) and mean canal diameter (Ca.Dm, µm) were measured after application of a standardized global threshold. Histograms representing the distribution of canal diameter sizes were produced to contrast patterns across the groups. For analysis of the trabecular VOIs, a standardized global threshold was again applied followed by 3D measurement of BV/TV (%), Tb.Th (mm), Tb.N (mm^{-1}), and Tb.Sp (mm).

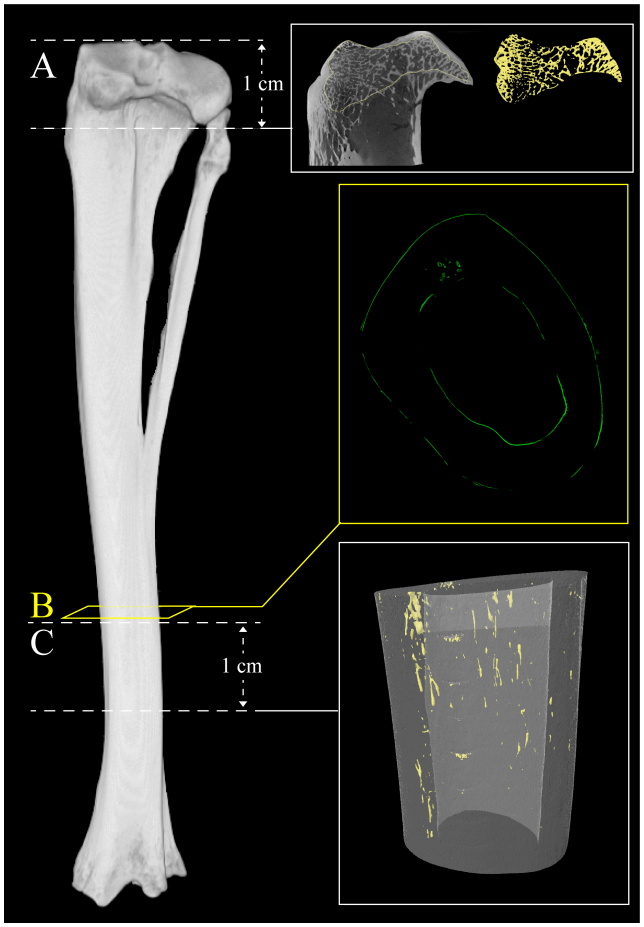

Figure 3.1. Micro-Computed Tomography (micro-CT) image of rabbit tibia depicting regions of analyses. (*A*) Location of trabecular bone micro-CT analysis. Scan field height is 1 cm. Reconstructed micro-CT image of proximal tibia scan and

corresponding three-dimensional reconstructed image of isolated trabecular bone highlighted in yellow *(right)*. (*B*) Location of histomorphometric analysis. Section is 300 μm thick. Fluorescent confocal microscopy image of transverse section of cortical bone *(right)*. (*C*) Location of cortical bone micro-CT analysis. Scan field height is 1 cm. Three-dimensional reconstructed image of cortical bone with cortical porosity highlighted in yellow *(right)*.

3.23. Dynamic Histomorphometry & Cortical Geometry

Confocal microscopy images were acquired from a cortical cross-section placed immediately proximal to the micro-CT VOI (Figure 3.1 B). The sections were cut using a low speed sectioning saw with a diamond wafer blade and ground and polished to a thickness of 300 μm (167). Mounted sections were subsequently imaged with a Leica (Leica Microsystems, Wetzlar, Germany) DMi8 confocal fluorescent microscope equipped with differential interference contrast microscopy (DIC) to capture fluorescent signals and cortical microstructure. 2D mosaics of the DIC and fluorescent images were produced and analyzed using basic ImageJ (https://imagej.nih.gov/ij/) functions (unless otherwise described).

Cross-sectional cortical geometry parameters, Ct.Ar (mm^2), Ma.Ar (mm^2), and Tt.Ar (mm^2) were assessed and percent cortical and percent marrow area (%Ct.Ar, %Ma.Ar) were calculated relative to Tt.Ar. Cortical thickness (μm) was measured using the BoneJ (168) plugin for ImageJ. To complement the cortical geometry measures, estimates of maximal and minimal bending (second moments of area, Imax, Imin, mm^4) as well as torsional stiffness (torsional section modulus, Zpol, mm^3) were measured from the most proximal micro-CT cross-sectional image. These measures were performed on the micro-CT data as this modality enabled the impact of internal porosity/surface geometry to be better integrated into the measures.

To evaluate the extent of active mineralization on bone surfaces, single and double labelled bone surfaces (sLS, dLS, respectively), and total bone surface (BS) were measured on the endosteal (Es) and periosteal (Ps) surfaces. Mineralizing surface per bone surface was calculated as (dLS+sLS/2)/BS on the endosteal (Es.MS/BS, %) and periosteal (Ps.MS/BS, %) surfaces.

Intracortical remodeling activity was then counted manually as single labelled osteons (sL.On), double labelled osteons (dL.On), and resorption cavities (Rs.N), defined as non-mineralizing pores characterized by eroded surfaces, no lamellar bone formation, and no calcein labelling. These parameters were normalized to Ct.Ar (sL.On/Ct.Ar, dL.On/Ct.Ar, and Rs.N/Ct.Ar, mm^{-2}) and used to calculate a ratio of labelled osteons *vs*. resorption cavities ((sL.On+dL.On)/Rs.N). In cross-sections where Rs.N was zero, a denominator of 1 was used to maximize the inclusion of data. Activation frequency was calculated as Ac.f = ((sL.On+dL.On)/Ct.Ar)/σ_f (#/mm^2/year), where σ_f, the osteon formation time, was calculated as W.Th/On.MAR (4). Wall thickness (W.Th, μm) reflects osteon wall thickness, the distance between osteon canal and cement line. This was measured from 50 randomly selected osteons for each animal within each transverse section using transmitted light microscopy at 20X

magnification. In sections with fewer than 50 osteons, all osteons present were measured. Osteonal mineral apposition rate (μm/day) was calculated as the inter-label distance, measured as the distance between two consecutive osteonal calcein labels, divided by the labeling period (14 days). Osteonal mineral apposition rate was measured in 20 randomly selected dL.On within each transverse section. In sections with fewer than 20 dL.On, all osteons present were measured. Activation frequency was calculated from mean W.Th and On.MAR values for each animal and therefore, only rabbits with On.MAR values were included in the mean calculation of Ac.f. Finally, to provide a measure of overall remodeling activity that did not rely upon normalization to σ_f, we calculated active remodeling centers (a.Rm.Cr, mm^{-2}) as the sum of resorption spaces and labelled osteons normalized to Ct.Ar: (sL.On+dL.On+Rs.N)/Ct.Ar.

3.24. Statistical Analysis

All statistical analyses were performed with SPSS version 26.0 (IBM, New York). The normality of all parameters was assessed by Shapiro-Wilk tests. Independent sample *t* tests were employed to evaluate animal weight percent change (testing difference from 0) across the entire experimental period (weeks 0-12) and also within the pre-dosing period (weeks 0-8) and the dosing period (weeks 8-12). When normally distributed for all groups, bone parameter data were assessed with One-way ANOVA ($\alpha = 0.05$) and, when significant, post-hoc tests were used to compare all groups *vs.* SHAM. If non-normal distributions were detected for one or more groups, the non-parametric Kruskal-Wallis H tests ($\alpha = 0.05$) with, when significant, post-hoc pairwise comparisons vs. SHAM using Dunn's procedure (169) were carried out. To account for repeated pair-wise post-hoc tests, the alpha value was adjusted using Bonferroni's method (170). For most measures, alpha and Confidence Intervals of the mean/median differences (SHAM – Treatment; hereafter just CI unless otherwise stated) were adjusted to account for the four pair-wise comparisons *vs.* SHAM resulting in $\alpha = 0.0125$ ($\alpha = 0.05/4$) and %CI = 98.75% (1- α). For comparisons lacking the two GC-dosed groups, the two pair-wise comparisons employed $\alpha = 0.025$ and %CI = 97.5%. To calculate the CIs, additional independent *t* tests for the normal data and Hodges-Lehmann tests for the non-normal data were employed. Instances where $p > \alpha$ but CIs did not straddle zero were flagged in the tables. Finally, fold changes relative to SHAM (Treatment / SHAM) were calculated for all parameters.

3.3. Results

3.31. Animal Weight

Statistics for weight and % weight change are summarized in Table 3.1 and depicted in Figure 2. SHAM, OVX, and OVX+GC gained weight during the 8-week pre-dosing period. While $p > \alpha$ for GC and PTH, the 95% CI of the percent change suggests weight gain in PTH should not be ruled out. During the 4-week dosing period SHAM and OVX again gained weight while GC, OVX+GC, and PTH all lost weight. Considering the entire 12-week experimental period, SHAM and OVX exhibited overall weight gain while only GC lost weight.

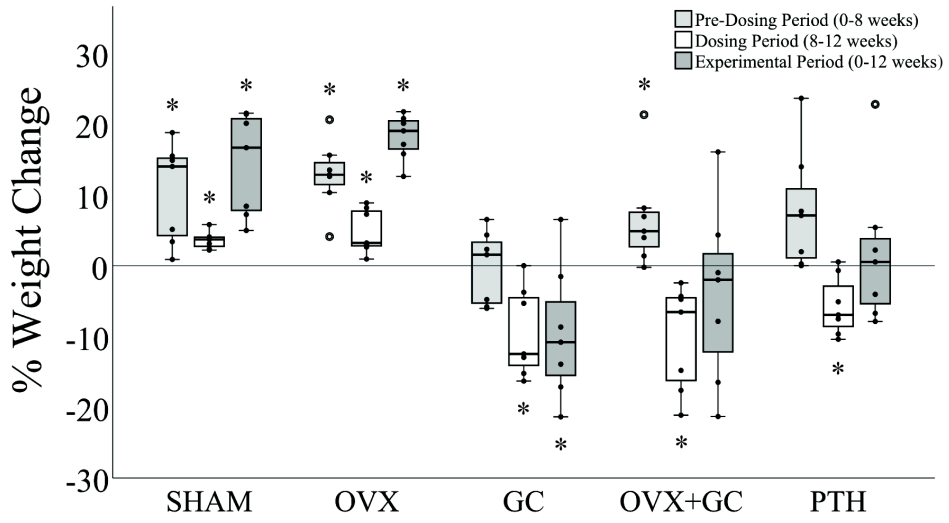

Figure 3.2. Analyses of mean changes in body weight in rabbit groups over experimental time period (0-3 months). Data are presented by boxplots with individual rabbits plotted as solid circles and outliers plotted as open circles. *N*=7. *Indicates $p < 0.05$ compared to 0 (independent sample *t* test). SHAM = control. OVX = Ovariectomy. GC = Glucocorticoid. OVX+GC = Ovariectomy & Glucocorticoid. PTH = Parathyroid Hormone.

Table 3.1. Rabbit Weight Analyses

	SHAM			OVX			GC			OVX+GC			PTH		
Parameter	**Mean ± SD**	***vs.* 0 *p***	**95% CI**	**Mean ± SD**	***vs.* 0 *p***	**95% CI**	**Mean ± SD**	***vs.* 0 *p***	**95% CI**	**Mean ± SD**	***vs.* 0 *p***	**95% CI**	**Mean ± SD**	***vs.* 0 *p***	**95% CI**
% Weight Change Pre-Dosing Period	10.37 ± 7.04	**0.008***	3.86 – 16.87	12.80 ± 5.02	**0.001***	8.16 – 17.45	-0.27 ± 5.19	0.894	-5.07 – 4.53	6.63 ±7.11	**0.049***	0.05 – 13.20	7.80 ± 8.58	0.053	-0.13 – 15.74
% Weight Change Dosing Period	3.60 ± 1.23	**<0.001***	2.46 – 4.74	4.86 ± 3.15	**0.006***	1.95 – 7.77	-9.44 ± 6.33	**0.008***	-15.29 - -3.58	-10.23 ± 7.45	**0.011***	-17.13 - -3.34	-5.69 ± 4.22	**0.012***	-9.59 - -1.78
% Weight Change Experimental Period	14.33 ± 7.24	**0.002***	7.64 – 21.02	18.18 ± 3.21	**<0.001***	15.21 – 21.15	-9.56 ± 9.49	**0.037***	-18.34 - -0.78	-4.04 ± 12.62	0.430	-15.71 – 7.64	1.75 ± 10.46	0.674	-7.92 – 11.42

Values are reported as mean ± standard deviation. N=7. Independent sample t tests were employed. Significance level for t tests was $\alpha = 0.05$ for comparison to 0. 95% confidence intervals (CI) of the mean are reported. SHAM = control. OVX = Ovariectomy. GC = Glucocorticoid. OVX+GC = Ovariectomy & Glucocorticoid. PTH = Parathyroid Hormone.

3.32. Cortical Porosity

Representative micro-CT 2D cross-sectional images and 3D renders of the VOIs are provided in Figure 3.3 A. Cortical pores appeared to be non-uniform and clustered within portions of the mid-cortex. Measurements of Ct.Po and Ca.Dm are summarized in Table 3.2 and Figure 3.3 B-C. Evidence of increased Ct.Po was observed for all groups. For OVX, OVX+GC, and PTH, $p < \alpha$, while GC exhibited a 4.6-fold increase and the CI was strongly offset from zero. Similar fold-change increases and CI ranges were observed across all groups for Ca.Dm (Figure 3.3 C), although $p < \alpha$ was only observed for OVX+GC and PTH. The distributions of Ca.Dm values (Figure 3.3 D) reflected the relatively low proportion of large resorption-space sized pores in SHAM, although this group did exhibit a peak in distribution of values around the expected (100 μm) osteon/resorption space diameter for rabbits. A similar peak dominated the distributions for OVX and PTH. The two GC dosed groups (GC and OVX+GC) exhibited a different pattern with higher proportions of much larger pores.

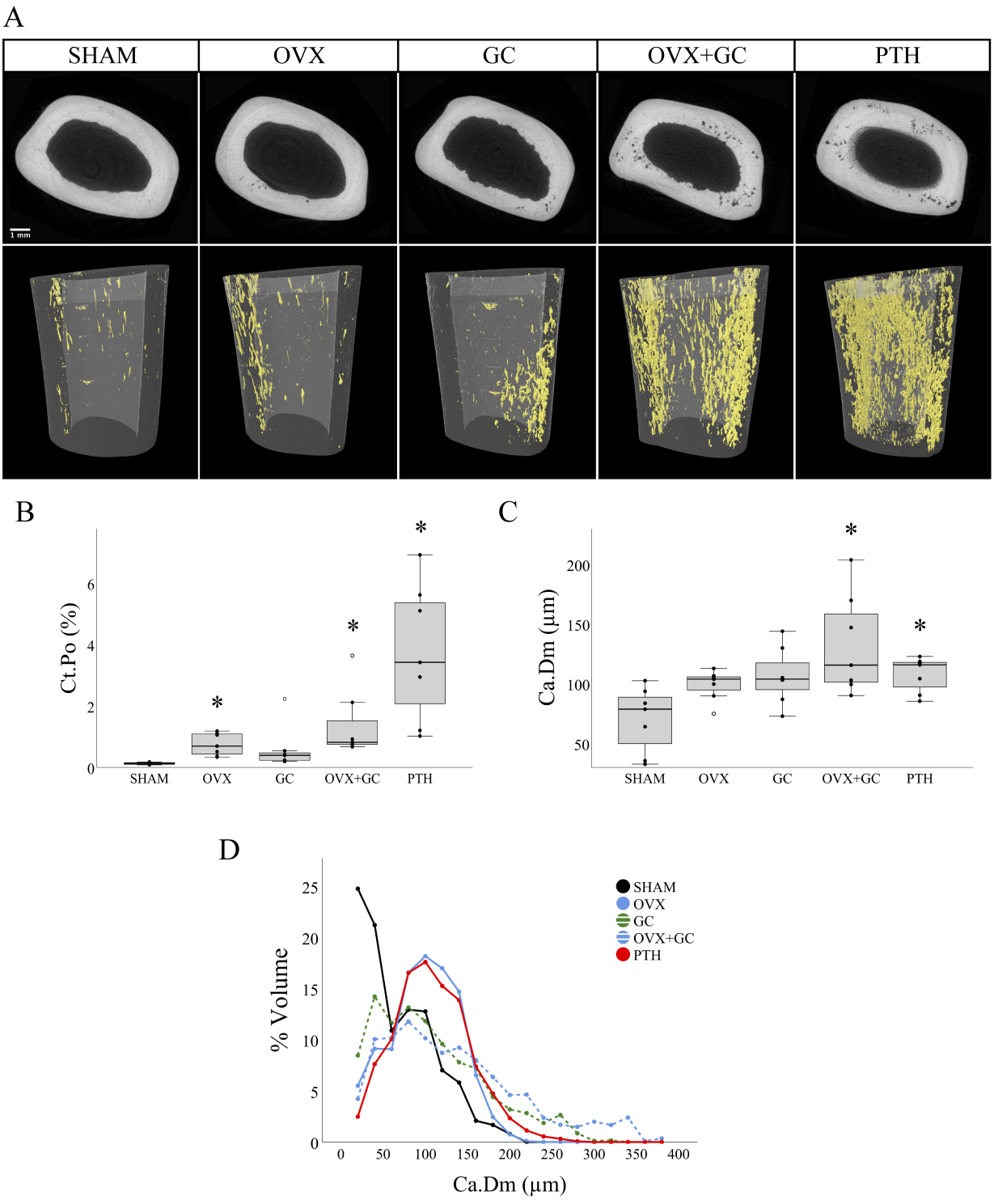

Figure 3.3. Micro-CT based analyses of cortical bone in rabbit tibiae. (*A*) Representative two-dimensional micro-CT cross sectional images of cortical bone in distal rabbit tibiae in various treatment groups with corresponding three-dimensional renders of volume of interest (*below*). Regions of cortical porosity at the level of

vascular canals are highlighted in yellow. Scale bar = 1 mm. (*B*) Cortical Porosity (Ct.Po) analysis in rabbit tibiae. Data are presented by boxplot with individual rabbits plotted as solid circles and outliers plotted as open circles. *N*=7. *Indicates $p < 0.0125$ compared to SHAM (Kruskal-Wallis with post-hoc Dunn's test). (*C*) Canal Diameter (Ca.Dm) analysis in rabbit tibiae. Data are presented by boxplot with individual rabbits plotted as solid circles and outliers plotted as open circles. *N*=7. *Indicates $p < 0.0125$ compared to SHAM (One-way ANOVA with post-hoc Bonferroni test). (*D*) Histograms depicting distributions of canal diameters in rabbit tibiae for each group. SHAM = control. OVX = Ovariectomy. GC= Glucocorticoid. OVX+GC = Ovariectomy & Glucocorticoid. PTH = Parathyroid Hormone.

Table 3.2. Micro-CT Cortical Bone Parameters

		SHAM	OVX				GC				OVX+GC				PTH			
Parameter	**Overall Test *p***	**Mean ± SD (Median)**	**Mean ± SD (Median)**	***vs.* SHAM *p***	**Mean/Median Difference (CI)**	**Fold Change**	**Mean ± SD (Median)**	***vs.* SHAM *p***	**Mean/Median Difference (CI)**	**Fold Change**	**Mean ± SD (Median)**	***vs.* SHAM *p***	**Mean/Median Difference (CI)**	**Fold Change**	**Mean ± SD (Median)**	***vs.* SHAM *p***	**Mean/Median Difference (CI)**	**Fold Change**
Ct.Po (%)	**<0.001***	0.13 ± 0.04 (0.13)	0.75 ± 0.37 (0.69)	**0.007***	-0.56 (-1.04 - -0.20)	5.8	0.60 ± 0.73 (0.39)	0.064	-0.24 (-2.09 - -0.06)[a]	4.6	1.38 ± 1.12 (0.82)	**0.001***	-0.69 (-3.49 - -0.57)	10.6	3.75 ± 2.24 (3.42)	**<0.001***	-3.29 (-6.78 - -0.92)	28.8
Ca.Dm (µm)	**0.003***	70.00 ± 27.40	99.00 ± 12.80	0.050	-28.84 (-62.37 – 4.69)	1.4	107.00 ± 24.10	0.015	-36.41 (-76.90 – 4.09)	1.5	133.00 ± 42.30	**<0.001***	-62.59 (-118.47 - -6.71)	1.9	108.00 ± 14.80	**0.012***	-37.68 (-72.23 - -3.12)	1.5

Values are reported as mean ± standard deviation. Median values are also reported for those parameters where at least one group was not normally distributed. *N*=7. One-Way ANOVA with post-hoc Bonferroni tests were employed for normal data. Kruskal Wallis test with post-hoc Dunn's tests were employed for non-normal data. Significance level for the overall tests was $\alpha = 0.05$ with the post-hoc tests adjusted for multiple comparisons vs. SHAM ($\alpha = 0.0125$). Mean differences and 98.75% CI of the mean differences are reported from independent *t* tests for normal data. Median differences and 98.75% CI of the median differences are reported from Hodges-Lehmann tests for non-normal data. [a]Indicates instances of disagreement between CIs and *p* values. Fold changes are reported relative to SHAM. Ct.Po = Cortical Porosity. Ca.Dm = Canal Diameter. SHAM = control. OVX = Ovariectomy. GC = Glucocorticoid. OVX+GC = Ovariectomy & Glucocorticoid. PTH = Parathyroid Hormone.

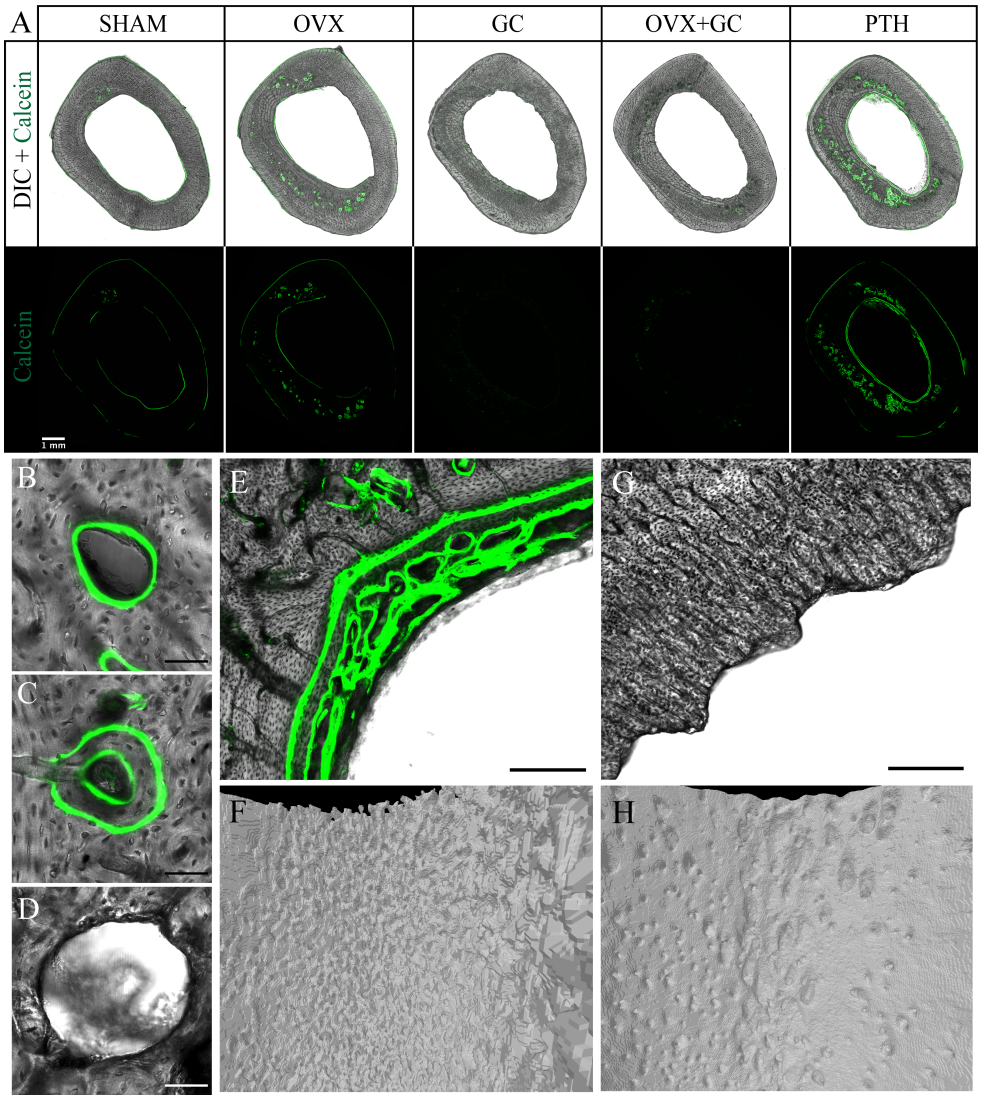

Figure 3.4. (*A*) Differential Interference Contrast (DIC) and fluorescent confocal microscopy images of transverse sections of rabbit tibiae in various treatment groups. Green fluorescent signal from calcein depicts areas of active bone formation. Absent signals from GC treated rabbits are due to inhibition of osteoblastic mediated bone formation by GC treatment. Scale bar = 1 mm. SHAM = control. OVX = Ovariectomy. GC = Glucocorticoid. OVX+GC = Ovariectomy & Glucocorticoid. PTH = Parathyroid Hormone. (*B-D*) Representative confocal microscopy images of (*B*) single labelled osteon, (*C*) double labelled osteon, and (*D*) resorption cavity. Scale bar = 50 µm. (E) Confocal microscopy image of PTH endosteal surface in transverse section. Note the trabecularized appearance of bone formed on the endosteal surface, a feature typical of woven bone. Scale bar = 150 µm. (*F*) Corresponding three-dimensional reconstructed micro-CT image of PTH endosteal surface. (*G*) Confocal microscopy image of GC endosteal surface in transverse section. Note scalloped appearance of endosteal bone. Scale bar = 150 µm. (*H*) Corresponding three-dimensional reconstructed micro-CT image of GC endosteal surface.

3.33. Cortical Bone Geometry

Representative DIC images are provided in Figure 3.4 and all cross-sectional geometry measures are summarized in Figure 3.5. It was evident from these images, as well as the 2D histological and 3D micro-CT images (Figure 3.4 G and Figure 3.3 A, respectively), that net resorption occurred at the endosteal surfaces of the two GC-dosed groups (GC and OVX+GC) with large trench-like packets of bone being removed (Figure 3.4 G). Quantitatively (Table 3.3), fold changes were generally subtle and the qualitative observations noted above were not corroborated by $p < \alpha$ with the exceptions being Ct.Ar, I_{min}, and Z_{pol} for GC.

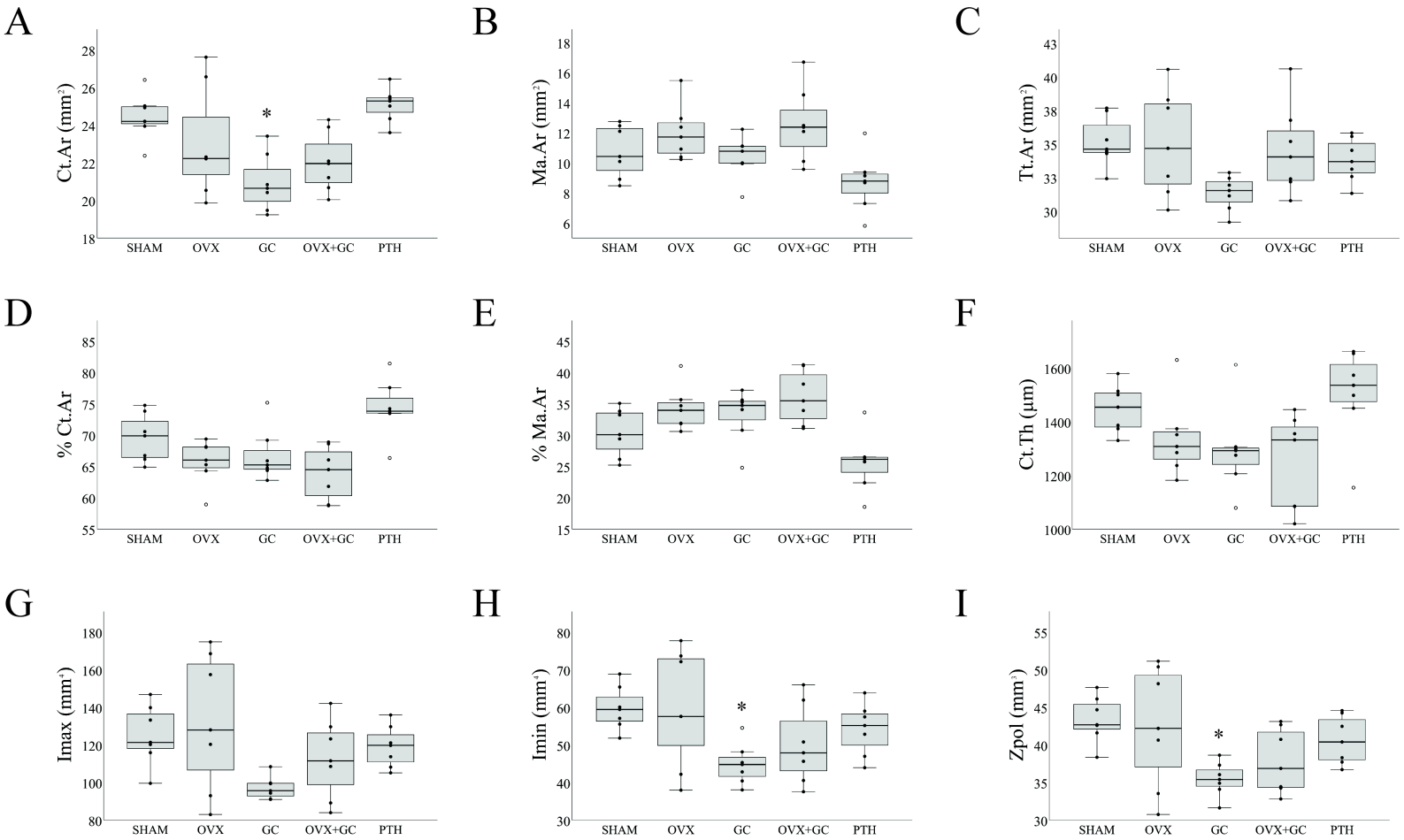

Figure 3.5. (*A-I*) Cortical bone geometry analyses in rabbit tibiae. Data are presented by boxplots with individual rabbits plotted as solid circles and outliers plotted as open circles. *N*=7. *Indicates $p < 0.0125$ compared with SHAM (One-way ANOVA with post-hoc Bonferroni test). Ct.Ar = Cortical Area. Ma.Ar = Marrow Area. Tt.Ar = Total Area. Ct.Th = Cortical Thickness. I_{max} = Maximum second moment of area. I_{min} = Minimum second moment of area. Z_{pol} = torsional section modulus. SHAM = control. OVX = Ovariectomy. GC = Glucocorticoid. OVX+GC = Ovariectomy & Glucocorticoid. PTH = Parathyroid Hormone.

Table 3.3. Cortical Bone Geometry Parameters

		SHAM	OVX				GC				OVX+GC				PTH			
Parameter	**Overall Test *p***	**Mean ± SD**	**Mean ± SD**	***vs.* SHAM *p***	**Mean Difference (CI)**	**Fold Change**	**Mean ± SD**	***vs.* SHAM *p***	**Mean Difference (CI)**	**Fold Change**	**Mean ± SD**	***vs.* SHAM *p***	**Mean Difference (CI)**	**Fold Change**	**Mean ± SD**	***vs.* SHAM *p***	**Mean Difference (CI)**	**Fold Change**
Tt.Ar (mm^2)	0.059	35.20 ± 1.86	35.10 ± 3.91	-	0.13 (-4.67 – 4.93)	1.0	31.30 ± 1.28	-	3.85 (1.34 – 6.36)[a]	0.9	34.60 ± 3.33	-	0.62 (-3.62 – 4.85)	1.0	33.80 ± 1.62	-	1.38 (-1.36 – 4.12)	1.0
Ct.Ar (mm^2)	**0.001***	24.40 ± 1.23	23.10 ± 2.93	0.100	1.40 (-2.13 – 4.92)	0.9	20.90 ± 1.52	**0.001***	3.52 (1.35 – 5.69)	0.9	22.00 ± 1.59	0.016	2.42 (0.19 – 4.65)[a]	0.9	25.10 ± 0.91	0.100	-6.65 (-2.34 – 1.05)	1.0
Ma.Ar (mm^2)	**0.007***	10.70 ± 1.72	12.00 ± 1.83	0.100	-1.26 (-4.05 – 1.53)	1.1	10.40 ± 1.42	0.100	0.33 (-2.14 – 2.80)	1.0	12.50 ± 2.46	0.086	-1.80 (-5.13 – 1.53)	1.2	8.72 ± 1.90	0.055	2.02 (-0.82 – 4.87)	0.8
% Ct.Ar (%)	**<0.001***	69.50 ± 3.83	65.70 ± 3.49	0.091	3.82 (-1.93 – 9.57)	0.9	66.80 ± 4.19	0.100	2.78 (-3.51 – 9.08)	1.0	63.90 ± 4.25	0.015	5.63 (-0.72 – 11.97)	0.9	74.40 ± 4.59	0.036	-4.80 (-11.42 – 1.83)	1.1
% Ma.Ar (%)	**<0.001***	30.40 ± 3.83	34.30 ± 3.49	0.091	-3.82 (-9.57 – 1.93)	1.1	33.20 ± 4.19	0.100	-2.78 (-9.08 – 3.51)	1.1	36.10 ± 4.25	0.015	-5.63 (-11.97 – 0.72)	1.2	25.60 ± 4.59	0.036	4.80 (-1.83 – 11.42)	0.8
Ct.Th (μm)	**0.019***	1448.63 ± 88.94	1338.49 ± 144.44	0.100	110.14 (-78.00 – 298.27)	0.9	1295.81 ± 161.98	0.070	152.82 (-51.38 – 357.01)	0.9	1247.01 ± 176.85	0.019	201.61 (-17.94 – 421.16)	0.9	1504.26 ± 172.80	0.100	-55.63 (-270.88 – 159.61)	1.0
I_{min} (mm^4)	**0.030***	59.79 ± 5.82	59.88 ± 15.62	0.100	-0.09 (-18.58 – 18.40)	1.0	44.92 ± 5.40	**0.007***	14.88 (6.06 – 23.69)	0.8	50.10 ± 10.54	0.070	9.69 (-3.67 – 23.05)	0.8	54.22 ± 6.91	0.100	5.57 (-4.46 – 15.60)	0.9
I_{max} (mm^4)	**0.039***	125.35 ± 15.98	132.22 ± 36.29	0.100	-6.87 (-50.85 – 37.12)	1.1	97.16 ± 6.08	0.017	28.19 (9.22 – 47.15)[a]	0.8	112.65 ± 21.08	0.100	12.70 (-16.64 – 42.04)	0.9	119.14 ± 11.13	0.100	6.21 (-15.39 – 27.81)	1.0
Z_{pol} (mm^3)	**0.019***	43.40 ± 3.08	42.42 ± 8.07	0.100	0.98 (-8.59 – 10.56)	1.0	35.45 ± 2.26	**0.003***	7.95 (3.71 – 12.18)	0.8	37.86 ± 4.29	0.034	5.53 (-0.32 – 11.39)	0.9	40.65 ± 3.20	0.100	2.75 (-2.17 – 7.67)	0.9

Values are reported as mean ± standard deviation. *N*=7, except for On.MAR and Ac.f measures for OVX (*N*=5) and SHAM (*N*=3). One-Way ANOVA with post-hoc Bonferroni tests were employed for normal data. Significance level for the overall tests was set at $\alpha = 0.05$ with the post-hoc tests adjusted for multiple comparisons vs. SHAM ($\alpha = 0.0125$). Mean differences and 98.75% confidence intervals (CI) of the mean differences are reported from independent *t* tests. [a]Indicates instances of disagreement between CIs and *p* values. Fold changes are reported relative to SHAM. Tt.Ar = Total Area. Ct.Ar = Cortical Area. Ct.Th = Cortical Thickness. Ma.Ar = Marrow Area. I_{min} = Minimum second moment of area. I_{max} = Maximum second moment of area. Z_{pol} = Torsional section modulus. Ma.Ar = Marrow Area. SHAM = control. OVX = Ovariectomy. GC = Glucocorticoid. OVX+GC = Ovariectomy & Glucocorticoid. PTH = Parathyroid Hormone.

3.34. Cortical Bone Histomorphometry

The calcein labels revealed active bone formation on the periosteal and endosteal surfaces as well as intra-cortical bone formation within actively forming osteons (Figures 3.4 and 3.6, Table 3.4). Formation was most pronounced in the PTH group, particularly at the endosteal surface and intra-cortically (reflected qualitatively in many geometry parameters in Figure 3.5). Conversely, the GC and OVX+GC groups exhibited reduced evidence of labelled bone formation on all surfaces (Figure 3.4 A). Due to the lack of formation, measures relying upon calcein labels were not assessable for GC and OVX+GC and were reported as no data (ND) in Table 3.4. Bone formation at both surfaces, Es.MS/BS and Ps.MS/BS, was increased in the PTH group. Endosteal bone formation in PTH had a distinct pattern that included well organized lamellar bone in places but also disorganized plates with a crude trabecular-like pattern reminiscent of woven bone in others (Figure 3.4 E & F). Periosteal MS/BS was highly variable with large outliers detected for SHAM and OVX.

Evidence of elevated remodeling was most dramatically and consistently observed in PTH with $p < \alpha$ for sL.On/Ct.Ar, dL.On/Ct.Ar, Rs.N/Ct.Ar, Ac.f, and a.Rm.Cr/Ct.Ar. The OVX group exhibited a similar but less pronounced (fold changes approximately half those of PTH) pattern for these parameters; although $p < \alpha$ was only detected for a.Rm.Cr/Ct.Ar, CIs with values largely distributed to one side of zero and with relatively large extremes caution against disregarding potential changes in the other parameters. For the glucocorticoid groups, Rs.N/Ct.Ar was elevated approximately 10- and 18-fold for GC and OVX+GC. Although only the latter had $p < \alpha$, the large fold change and distribution of the CI for GC again caution against disregarding a potential effect. The ratio of labelled osteons to resorption cavities (sL.On + dL.On)/Rs.N was 0.1 and 0.4 of that for SHAM for OVX+GC and GC, respectively, with the former having $p < \alpha$.

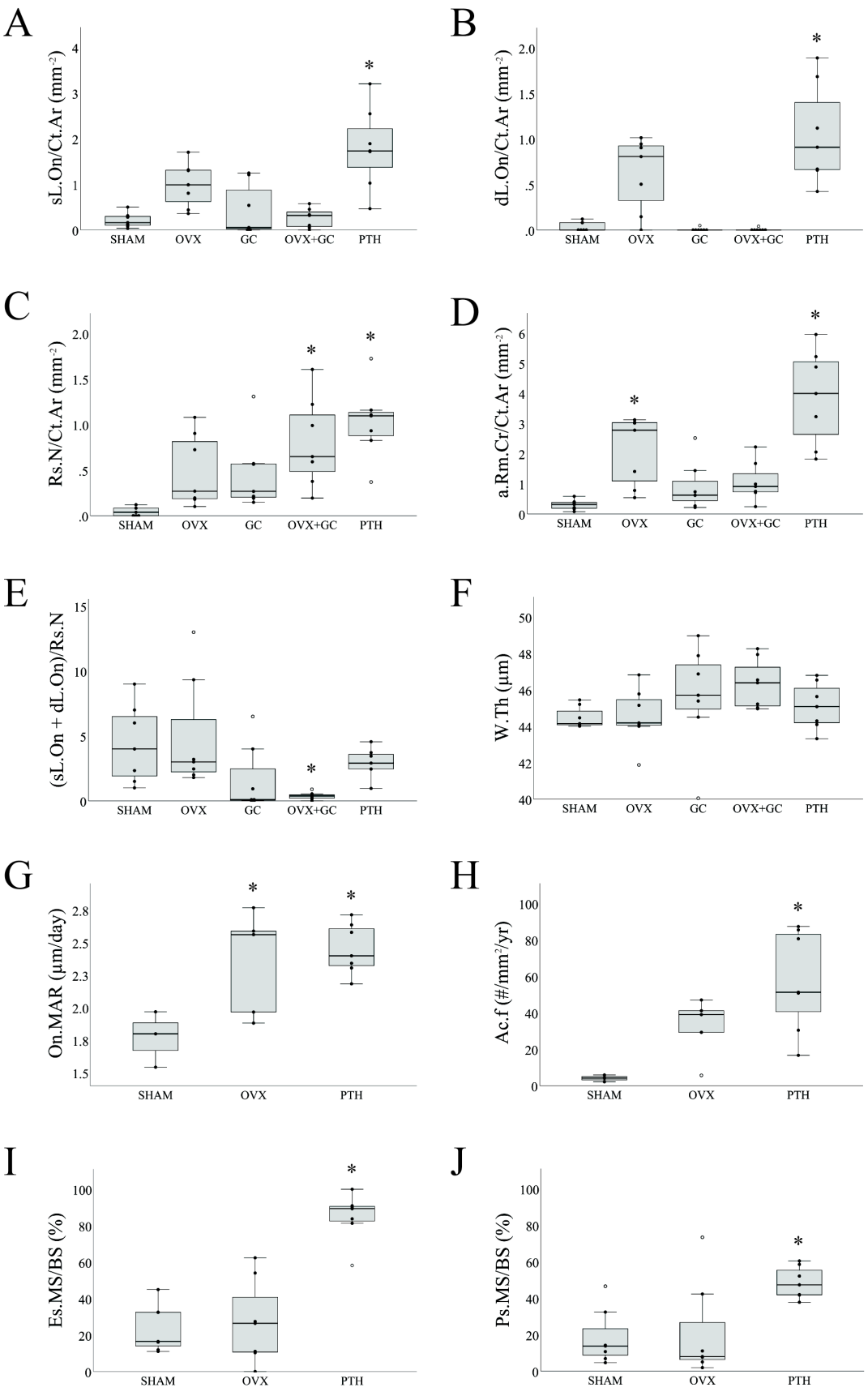
A
sL.On/Ct.Ar (mm-2)
B
dL.On/Ct.Ar (mm-2)
C
Rs.N/Ct.Ar (mm-2)
D
a.Rm.Cr/Ct.Ar (mm-2)
E
(sL.On + dL.On)/Rs.N
F
W.Th (µm)
G
On.MAR (µm/day)
H
Ac.f (#/mm2/yr)
I
Es.MS/BS (%)
J
Ps.MS/BS (%)
SHAM
OVX
GC
OVX+GC
PTH

Figure 3.6. (*A-J)* Histomorphometric analyses of transverse cortical bone sections in rabbit tibiae. Data are presented by boxplots with individual rabbits plotted as solid circles and outliers plotted as open circles. *N*=7 except for On.MAR and Ac.f measures for OVX (*N*=5) and SHAM (*N*=3). *Indicates $p < 0.0125$ compared to SHAM unless otherwise stated (Kruskal-Wallis with post-hoc Dunn's test for dL.On/Ct.Ar, sL.On/Ct.Ar, Rs.N/Ct.Ar, a.Rm.Cr/Ct.Ar, and W.Th). For On.MAR, Ac.f, PS.MS/BS, and Es.MS/BS, *indicates $p < 0.025$ (One-way ANOVA with post hoc Bonferroni test for Es.MS/BS, On.MAR, and Ac.f, Kruskal-Wallis with post-hoc Dunn's test for PS.MS/BS). sL.On = Single Labelled Osteon. dL.On = Double Labelled Osteon. Rs.N = Resorption Cavity Number. a.Rm.Cr = Active Remodeling Centers. Ct.Ar = Cortical Area. W.Th = Wall Thickness. On.MAR = Osteonal Mineral Apposition Rate. Ac.f = Activation Frequency. Es = Endosteal. Ps = Periosteal. MS/BS = Mineralizing Surface per Bone Surface. SHAM = control. OVX = Ovariectomy. GC = Glucocorticoid. OVX+GC = Ovariectomy & Glucocorticoid. PTH = Parathyroid Hormone.

Table 3.4. Cortical Bone Histomorphometric Parameters

		SHAM	OVX				GC				OVX+GC				PTH			
Parameter	**Overall Test *p***	**Mean ± SD (Median)**	**Mean ± SD (Median)**	***vs.* SHAM *p***	**Mean/Median Difference (CI)**	**Fold Change**	**Mean ± SD (Median)**	***vs.* SHAM *p***	**Mean/Median Difference (CI)**	**Fold Change**	**Mean ± SD (Median)**	***vs.* SHAM *p***	**Mean/Median Difference (CI)**	**Fold Change**	**Mean ± SD (Median)**	***vs.* SHAM *p***	**Mean/Median Difference (CI)**	**Fold Change**
sL.On/Ct.Ar (mm^{-2})	**0.001***	0.21 ± 0.16 (0.16)	0.99 ± 0.49 (0.99)	0.020	0.80 (0.13 – 1.42)[a]	4.1	0.44 ± 0.57 (0.05)	0.734	-0.03 (-0.31 – 1.12)	2.1	0.26 ± 0.22 (0.32)	0.855	0.02 (-0.28 – 0.42)	1.2	1.80 ± 0.91 (1.73)	**0.001***	1.59 (0.34 – 2.92)	8.4
dL.On/Ct.Ar (mm^{-2})	**<0.001***	0.04 ± 0.05 (0.00)	0.62 ± 0.41 (0.81)	0.031	0.78 (0.00 – 0.95)	15.4	0.01 ± 0.02 (0.00)	0.471	0.00 (-0.08 – 0.00)	0.2	0.01 ± 0.02 (0.00)	0.454	0.00 (-0.08 – 0.00)	0.2	1.05 ± 0.55 (0.91)	**0.002***	0.91 (0.42 – 1.81)	26.3
Rs.N/Ct.Ar (mm^{-2})	**<0.001***	0.05 ± 0.05 (0.04)	0.49 ± 0.40 (0.27)	0.015	0.23 (0.07 – 1.00)[a]	10.7	0.47 ± 0.41 (0.27)	0.016	0.23 (0.11 – 1.22)[a]	10.1	0.80 ± 0.50 (0.65)	**<0.001***	0.61 (0.19 – 1.52)	17.5	1.03 ± 0.41 (1.10)	**<0.001***	1.01 (0.37 – 1.64)	22.4
a.Rm.Cr/Ct.Ar (mm^{-2})	**<0.001***	0.30 ± 0.17 (0.31)	2.10 ± 1.15 (2.78)	**0.002***	2.43 (0.23 – 2.92)	7.0	0.92 ± 0.81 (0.62)	0.144	0.38 (-0.13 – 2.16)	3.1	1.07 ± 0.66 (0.91)	0.042	0.60 (0.04 – 1.86)[a]	3.6	3.87 ± 1.59 (4.00)	**<0.001***	3.68 (1.51 – 5.60)	12.9
(sL.On + dL.On)/ Rs.N	**0.003***	4.40 ± 3.02 (4.00)	4.97 ± 4.39 (3.00)	0.990	0.33 (-5.80 – 8.33)	1.1	1.66 ± 2.58 (0.09)	0.025	-2.33 (-7.00 – 2.50)	0.4	0.37 ± 0.29 (0.37)	**0.002***	-3.63 (-8.62 - -0.63)	0.1	2.93 ± 1.15 (2.90)	0.686	-1.38 (-6.05 – 2.22)	0.7
W.Th (µm)	0.093	44.49 ± 0.59 (44.15)	44.56 ± 1.57 (44.19)	-	-0.04 (-2.36 – 2.21)	1.0	45.63 ± 2.89 (45.71)	-	-1.42 (-4.51 – 4.04)	1.0	46.34 ± 1.37 (46.39)	-	-1.34 (-3.94 – 0.19)	1.0	45.11 ± 1.29 (45.08)	0.961	-0.43 (-2.54 – 1.15)	1.0
On.MAR (µm/day)	**0.013***	1.77 ± 0.21	2.35 ± 0.40	**0.015***	-0.58 (-1.34 – 0.18)[a]	1.3	ND	ND	ND	ND	ND	ND	ND	ND	2.45 ± 0.19	**0.005***	-0.68 (-1.06 - -0.30)	1.4
Ac.f (#/mm^2/yr)	**0.012***	4.04 ± 1.89	32.43 ± 16.28	0.102	-28.39 (-57.31 – 0.53)	8.0	ND	ND	ND	ND	ND	ND	ND	ND	57. 54 ± 27.98	**0.004***	-53.49 (-99.54 - -7.45)	14.2
Es.MS/BS (%)	**<0.001***	23.65 ± 13.01	27.39 ± 23.26	0.100	61.19 (-29.52 – 22.06)	1.2	ND	ND	ND	ND	ND	ND	ND	ND	84.84 ± 13.17	**<0.001***	57.46 (-79.11 - -43.27)	3.6
Ps.MS/BS (%)	**0.027***	18.44 ± 15.34 (13.75)	21.34 ± 26.67 (7.98)	0.100	-2.75 (-27.40 – 37.69)	1.2	ND	ND	ND	ND	ND	ND	ND	ND	48.58 ± 8.77 (47.35)	**0.020***	-33.14 (-47.51 - -9.35)	2.6

Values are reported as mean ± standard deviation. Median values are also reported for those parameters where at least one group was not normally distributed. *N*=7. One-Way ANOVA with post-hoc Bonferroni tests were employed for normal data. Kruskal-Wallis tests with post-hoc Dunn's tests were employed for non-normal data. Significance level for the overall tests was $\alpha = 0.05$ with the post-hoc tests adjusted for multiple comparisons vs. SHAM ($\alpha = 0.0125$). GC and OVX+GC were not analyzed for On.MAR, Ac.f, Es.MS/BS, and Ps.MS/BS due to a lack of detected labels and thus the significance level was adjusted for associated post-hoc tests ($\alpha = 0.025$). Mean differences and 98.75% ($\alpha = 0.0125$) or 97.5% ($\alpha = 0.025$) confidence intervals (CI) of the mean differences are reported from independent *t* tests for normal data. Median differences and 98.75% ($\alpha = 0.0125$) or 97.5% ($\alpha = 0.025$) CI of the median differences are reported from Hodges-Lehmann tests for non-normal data. [a]Indicates instances of disagreement between CIs and *p* values. Fold changes are reported relative to SHAM. sL.On = Single Labelled Osteon. dL.On = Double Labelled Osteon. Rs.N = Resorption Cavity Number. a.Rm.Cr = Active Remodeling Centers. Ct.Ar = Cortical Area. W.Th = Wall Thickness. On.MAR = Osteonal Mineral Apposition Rate. Ac.f = Activation Frequency. Es= Endosteal. Ps = Periosteal. MS/BS = Mineralizing Surface per Bone Surface. SHAM = control. OVX = Ovariectomy. GC = Glucocorticoid. OVX+GC = Ovariectomy & Glucocorticoid. PTH = Parathyroid Hormone. ND = No Data.

3.35. Trabecular Bone Micro-CT

Figure 3.7 A presents 3D renders of a portion of the VOI used for analysis of trabecular morphology. Overall, although fold changes were more subtle than many of the cortical parameters, a pattern of loss was observed for OVX, GC, and OVX+GC groups, while the opposite was observed for PTH (Table 3.5 and Figure 3.7 B-E). The reduction in BV/TV had $p < \alpha$ for both glucocorticoid groups, while OVX exhibited a similar fold change and a CI including zero but values offset to one side. Conversely, PTH exhibited the opposite pattern with the largest fold change (1.2) and strongly offset CI. Changes in Tb.N consistently supported the overall patterns of change with $p < \alpha$ for all groups. A predictable concomitant change in Tb.Sp was, generally, supported by the fold changes and CIs while Tb.Th had the smallest fold changes and CIs most evenly distributed about zero indicating the stability of this parameter across the groups with the only exception perhaps being GC.

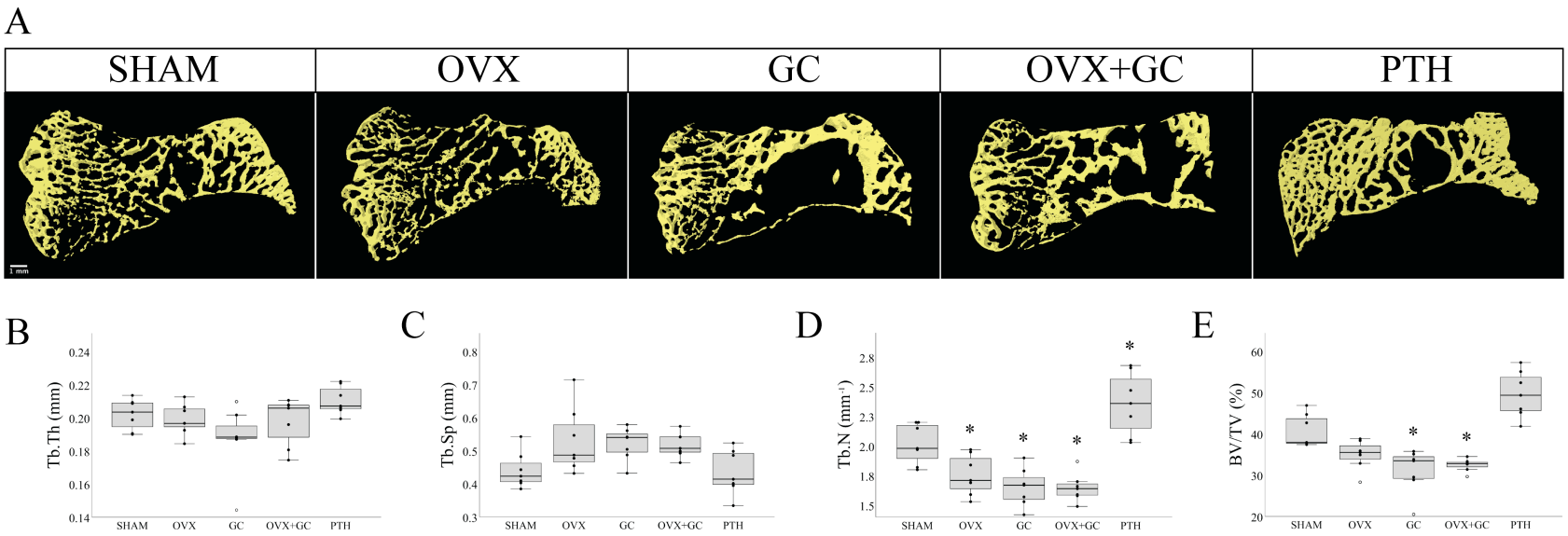

Figure 3.7. Micro-CT based analyses of trabecular bone in rabbit tibiae. (*A*) Three-dimensional reconstructed images of epiphyseal subchondral trabecular bone structure in rabbit tibiae of various treatment groups. Regions of trabecular bone are highlighted in yellow. Scale bar = 1 mm. (*B-E*) Three-dimensional trabecular bone analyses in rabbit tibiae. Data are presented by boxplots with individual rabbits plotted as solid circles and individual outliers plotted as open circles. *N*=7. *Indicates $p < 0.0125$ compared to SHAM (One-Way ANOVA with post-hoc Bonferroni test for Tb.Th and BV/TV, Kruskal-Wallis with post-hoc Dunn's test for Tb.Sp and Tb.N). BV/TV = Bone Volume/Tissue Volume. Tb.Th = Trabecular Thickness. Tb.N = Trabecular Number. Tb.Sp = Trabecular Separation. SHAM = control. OVX = Ovariectomy. GC = Glucocorticoid. OVX+GC = Ovariectomy & Glucocorticoid. PTH = Parathyroid Hormone.

Table 3.5. Micro-CT Trabecular Bone Parameters

		SHAM	OVX				GC				OVX+GC				PTH			
Parameter	**Overall Test *p***	**Mean ± SD (Median)**	**Mean ± SD (Median)**	***vs.* SHAM *p***	**Mean/Median Difference (CI)**	**Fold Change**	**Mean ± SD (Median)**	***vs.* SHAM *p***	**Mean/Median Difference (CI)**	**Fold Change**	**Mean ± SD (Median)**	***vs.* SHAM *p***	**Mean/Median Difference (CI)**	**Fold Change**	**Mean ± SD (Median)**	***vs.* SHAM *p***	**Mean/Median Difference (CI)**	**Fold Change**
BV/TV (%)	**<0.001***	40.73 ± 3.97 (37.93)	34.94 ± 3.57 (35.49)	0.112	-4.90 (-12.00 – 0.87)	0.9	31.01 ± 5.33 (33.48)	**0.006***	-8.87 (-17.42 - -2.33)	0.8	32.45 ± 1.54 (32.77)	**0.004***	-7.77 (-14.13 - -4.10)	0.8	49.60 ± 5.62 (49.36)	0.220	8.28 (-0.84 – 17.68)	1.2
Tb.Th (mm)	0.065	0.20 ± 0.01 (0.20)	0.20 ± 0.01 (0.20)	-	0.00 (-0.02 – 0.01)	1.0	0.19 ± 0.02 (0.19)	-	-0.01 (-0.05 – 0.01)	0.9	0.20 ± 0.02 (0.21)	-	0.00 (-0.03 – 0.02)	1.0	0.21 ± 0.01 (0.21)	-	0.01 (-0.01 – 0.02)	1.0
Tb.Sp (mm)	**0.018***	0.44 ± 0.06	0.53 ± 0.10	0.015	-0.09 (-0.22 – 0.04)	1.2	0.52 ± 0.05	0.031	-0.08 (-0.16 – 0.00)	1.2	0.52 ± 0.04	0.039	-0.08 (-0.15 – 0.00)	1.2	0.44 ± 0.07	0.100	0.01 (-0.09 – 0.10)	1.0
Tb.N (mm^{-1})	**<0.001***	2.02 ± 0.17	1.75 ± 0.17	**0.012***	0.26 (0.00 – 0.53)	0.9	1.65 ± 0.16	**0.001***	0.37 (0.11 – 0.63)	0.8	1.65 ± 0.12	**0.001***	0.37 (0.14 – 0.60)	0.8	2.36 ± 0.27	**0.002***	-0.34 (-0.69 – 0.01)	1.2

Values are reported as mean ± standard deviation. Median values are also reported for those parameters where at least one group was not normally distributed. *N*=7. One-Way ANOVA with post-hoc Bonferroni tests were employed for normal data. Kruskal Wallis test with post-hoc Dunn's tests were employed for non-normal data. Significance level for the overall tests was $\alpha = 0.05$ with the post-hoc tests adjusted for multiple comparisons vs. SHAM ($\alpha = 0.0125$). Mean differences and 98.75% confidence intervals (CI) of the mean differences are reported from independent *t* tests for normal data. Median differences and 98.75% CI of the median differences are reported from Hodges-Lehmann tests for non-normal data. [a]Indicates instances of disagreement between CIs and *p* values. Fold changes are reported relative to SHAM. BV/TV = Bone Volume/Tissue Volume. Tb.Th = Trabecular Thickness. Tb.N = Trabecular Number. Tb.Sp = Trabecular Separation. SHAM = control. OVX = Ovariectomy. GC = Glucocorticoid. OVX+GC = Ovariectomy & Glucocorticoid. PTH = Parathyroid Hormone.

3.4. Discussion

In general, the animals tolerated the OVX/sham surgeries well and weight gain was observed in three of the groups during the pre-dosing period (SHAM, OVX, and OVX+GC) and suggested by the data for the fourth (GC). Glucocorticoid dosing was not as well tolerated by the animals and weight loss was observed during the dosing period, an observation consistent with past studies for GC (159) and OVX+GC (163). Three of the GC rabbits had a more extreme reaction to treatment exhibiting hair textural changes. Notably, the 1.5 mg/kg/day dose we administered is moderate to high in the context of existing literature and 2 mg/kg/day has been reported as lethal (152). Further, administering lower doses (1 mg/kg/day) over longer lengths of time (six weeks) had also resulted in the premature death of one animal (163). As such, increasing GC dose or the length of dosing to possibly induce larger scale differences in cortical bone parameters may not be feasible in terms of animal welfare. Parathyroid hormone dosing was well tolerated by the animals. While they exhibited weight loss over the dosing period, it was less pronounced than that observed in the GC-dosed groups. Hirano and colleagues (71) found a similar decrease in weight after dosing rabbits with a comparatively higher dose of PTH at 40 μg/kg/5 days a week for 20 weeks.

The characterization of cortical porosity in the OP models and PTH was our primary objective and evidence of elevations were detected in all groups. Comparative data are limited as cortical porosity is only sparsely reported in the literature for rabbit OP models. In a recent report, Chandler and colleagues (163) observed no difference in Ct.Po at the femoral mid-diaphysis between SHAM (0.50%) and OVX (0.43%) groups at 18 weeks post-surgery, while their OVX+GC group (dosed for 12 weeks commencing 6 weeks after OVX) had elevated Ct.Po (9.75%). It is unclear what underpins their lack of a difference for OVX compared with our study. It could relate to the different skeletal elements studied (femur vs. tibia), relative location of the VOI (mid-shaft vs. distal shaft), the larger (15 μm) voxel size used, and/or Chandler and colleagues' longer duration post-surgery. Regarding the latter, their longer post-surgery phase for OVX, at 18 weeks *vs.* our 12 weeks, may have enabled more time for cortical remodeling to reach steady state (*see discussion of Ac.f below*). The PTH group had the most pronounced difference in Ct.Po, a result consistent with recent reports. Yamane and colleagues (150) reported a Ct.Po of 3.62% in rabbit tibiae after treatment with 40 μg/kg/day of PTH for 4 weeks, assessed using micro-CT at a 19.1 μm voxel size, while Zebaze and colleagues (106) reported a higher Ct.Po of 8.7% in rabbit femora using the same dosing regimen and imaging at 15 μm voxel size.

Across all groups, qualitative inspection of the images suggested the cortical pores did not appear to be randomly distributed rather, they were frequently clustered in the mid-cortex. The reason underpinning this is unclear although, it may be linked to developmental features and the localized age of the tissue. In rats, central bands or "islands" of calcified cartilage have been observed indicating remnants of developmental tissues in the mid-cortex (171, 172). It is unclear if this was the case in our rabbits, although the central cortex had distinctly complex microarchitecture when compared with more organized lamellar bone, which was particularly evident at the periosteal surface. Mid-cortical porosity in PTH contrasts with observations by

Zebaze and colleagues (106) and Hirano and colleagues (105) who reported increased porosity primarily adjacent to the marrow cavity in the proximal femur and tibial midshaft of rabbits, respectively. It is unclear if these endosteal pores reported by others may be related to the endosteal bone formation we observed.

Canal diameter values for SHAM were slightly lower (mean of 70 μm) than anticipated for remodeling-related resorption spaces in rabbits. This 3D micro-CT measure, however, includes all resolved pores ranging in size from the maximal diameter of cutting-cones, down through the contracting diameter of the closing-cones and, ultimately, approaching the normal scale of mature quiescent canals. The latter were not resolved by our micro-CT protocol (Supplemental Figure 3.81). The distribution of Ca.Dm (Figure 3.3 D) for SHAM did reveal a peak in values at the expected 100 μm size for secondary osteons/resorption spaces in rabbits. The distributions of Ca.Dm were very similar for OVX and PTH and their modal values (~100 μm) corresponded closely with the peak in SHAM. This suggests that the maximal diameters of the resorption spaces created in these groups are similar and of a scale consistent with past reports of normal secondary osteon size in rabbits. Conversely, the GC-dosed groups exhibited distributions skewed toward larger Ca.Dm, suggesting larger initial resorption spaces or the coalescence of spaces in the cortex. Two-dimensional data (Supplemental Figure 3.82) corroborate that pore sizes were increased in the GC-dosed groups but also in PTH. Zebaze and colleagues (106) have suggested PTH produces larger pores by enlarging existing canals which then coalesce, evidenced by micro-CT analysis.

Our secondary objective was to test the hypothesis that elevations in cortical porosity are associated with increased remodeling rates in these rabbit OP models, which we found to be increased in all groups relative to SHAM. Activation frequency represents the most direct measure of the rate of remodeling as it is a measure of the birth rate of new BMUs. That said, this measure presented several challenges for our study. First, both GC-dosed groups exhibited little sign of bone formation, rendering measures relying upon the labelled structures unassessable for these groups. This was consistent with the primary mechanism of GC-induced bone loss via osteoblast suppression (173). The low numbers of double-labelled osteons in SHAM and OVX, including their absence in some animals, further complicated the assessment of Ac.f. which requires labelled osteons in its numerator and osteon formation time (σ_f = W.Th/On.MAR) in its denominator. This reduced the number of animals available for the comparisons of this parameter, diminishing statistical power and thus, the generalizability of the results should be interpreted with caution. Finally, a key basis of this estimation of BMU birth rate is the assumption of a steady state where the same number of BMUs (generally quantified as labelled osteons) are being “born” and “dying”. Given that we expected elevation in remodeling rate for the OP models and that it has been previously demonstrated for PTH, this assumption is dubious in our case. Further, equal birth and death rates for duration of the newly established σ_f is needed to reach a new steady state after experimental perturbation (4). Osteon formation time assessed in our study (based upon mean W.Th and On.MAR reported in Table 4) was approximately 25, 19, and 18 days for SHAM, OVX, and PTH, respectively. There simply was

not enough time in our 28-day dosing period, with calcein labels first administered at the midpoint, for a new steady state to have occurred for PTH and GC. Whether or not the OVX group had reached a new steady state is less clear, but it is more plausible since the first calcein label was administered 69 and 70 days after surgery. Despite these limitations, we have reported Ac.f here to facilitate comparison with existing studies (which may also not meet the underlying assumptions) and, in the case of OVX rabbits (8-fold increase relative to SHAM with the caveat that $p > \alpha$), provide novel, albeit limited, data to the literature. Our Ac.f value for PTH was 14-fold higher than SHAM, a result that aligns well with a previous study of rabbits dosed with 40 μg/kg/day, 5 days per week for 20 weeks where Ac.f was reported to increase 20-fold in tibiae (43.8) (71). The higher Ac.f for PTH was associated with increased sL.On/Ct.Ar, dL.On/Ct.Ar, and Rs.N/Ct.Ar – findings again consistent with this previous PTH trial (71). Activation frequency was also reported in rabbits receiving a lower dose of PTH, 10 μg/kg/5 days per week, for 35 days. Due to this lower dose, Mashiba and colleagues (83) reported only a 2-fold increase in Ac.f (29.3) in comparison to aged-matched controls. While it has become standard to include only labelled osteons in Ac.f, Frost's early description indicated the numerator of Ac.f should be "the number of bone-forming or resorbing centers" (4). Thus, to overcome some of the limitations of Ac.f, and provide a measure of overall remodeling rate/activity that included the GC-dosed groups, we calculated a measure of active remodeling centers, a.Rm.Cr/Ct.Ar, which was not normalized to any assumption about osteon formation time and included both labelled osteons and resorption spaces. By this measure OVX and PTH were elevated related to SHAM 7- and 13-fold, respectively, and the approximately 3-fold increases for GC and OVX+GC suggest a difference in those groups as well. This observation for the glucocorticoid groups was corroborated by the large fold-changes in Rs.N/Ct.Ar with $p < \alpha$ for OVX+GC. OVX and PTH also exhibited elevated radial mineral apposition rates (On.MAR) within forming osteons, providing corroborating evidence of an increase in the formative activity of BMUs. Conversely, the ratio of labelled osteons to resorption cavities ((sL.On + dL.On)/Rs.N) was reduced for OVX+GC (0.1 fold, $p < \alpha$) and GC (0.4 fold) indicating a lack of transition from bone resorption to formation (uncoupling (133-135)) in the glucocorticoid groups. Taken together, the histomorphometric data support the hypothesis that the rate of remodeling was elevated in all of these OP models, although the evidence for the GC was less robust than the other groups.

Measures of cortical geometry and associated bone strength were largely unchanged across groups which was not unexpected given the skeletal maturity of the animals and the short duration of the experiments. The exceptions to this were changes in several parameters for GC associated with the distinct endosteal resorption observed in the glucocorticoid groups whereby large packets of bone were being resorbed with no evidence of formation within them. Whether these spaces reflect uncoupled BMUs (133-135) or a negative (resorptive) modeling drift (4) is perhaps a semantic point. It did not appear that these resorptions represented trabecularization of the cortex created by coalescence of numerous individual BMUs. Notably, this pattern of thinning cortices through increased endocortical bone resorption has been reported in GC treated rats (174). A previous report noted decreased cortical bone volume in GC treated rabbits (159).

For OVX+GC, Liu and colleagues (153) reported no significant changes in Ct.Th, whereas Chandler and colleagues (163) found significantly lower Ct.Ar and Ct.Th. For the current study, it was unclear if the decline in I_{min} we observed in GC was indicative of localized changes in porosity and/or cortical thickness related to mechanical axes. Given the non-random distribution of cortical pores visually apparent across all the groups, more detailed analysis of the interplay of mechanical axes and regional variation of bone microarchitecture across all envelopes (periosteal, intra-cortical, and endosteal) is certainly warranted.

Endosteal bone apposition induced by PTH administration has been well documented in animal (71, 83, 91, 105, 150) and human studies (54, 55) and it has been suggested that this bone formation may be compensating for the increase in intracortical porosity to limit negative biomechanical effects (71, 87). We observed extensive endosteal bone formation for PTH, which uniquely had a trabecular-like appearance in 2D and 3D (Figure 3.4 E & F). It has been suggested that this may be poorly developed woven bone (150), a tissue type formed in states of high turnover/growth. Previous PTH rabbit studies have demonstrated small decreases in Ma.Ar (71) and increases in Ct.Ar (71, 83, 105). Hirano and colleagues (71) also found rabbits treated with PTH increased Tt.Ar, which was associated with periosteal bone formation, while several other large animal studies showed that the measure remained unchanged (83, 85, 87). We observed increased bone formation at both the endosteal and periosteal surfaces for PTH, although this did not translate into changes in overall geometry relative to SHAM, which may be due to our relatively short dosing period of 4-weeks.

Our final objective was to contrast trabecular bone differences in the proximal tibia to facilitate contextual comparisons within the literature and compare effects across bone morphotypes. Previous reports are conflicted with respect to the effect of OVX on trabecular bone microarchitecture with one observing changes (175) and two others reporting no change relative to sham operated controls (153, 154). For the former, BV/TV and Tb.N were reduced and Tb.Sp increased in OVX rabbits compared to controls (175) at 27 weeks post OVX. For our study, Tb.N was reduced in OVX and the CI of BV/TV suggests a change in this parameter should not be ruled out. GC has been reported to reduce BV/TV (154) as well as reduce Tb.Th and Tb.N (159), while OVX+GC rabbits have also been reported to have reduced Tb.N, Tb.Th, Tb.Sp and BV/TV (153, 154, 162). Our findings of reduced BV/TV driven by a decline in Tb.N for both glucocorticoid groups are consistent with these previous reports.

Trabecular bone formation induced by PTH administration has been extensively characterized in animal and human studies (61, 80, 176-179) although increases in rabbit trabecular bone have been less consistent. In the lumbar vertebrae of rabbits, PTH at a dose of 10 μg/kg/day for 35 days increased BV/TV and Tb.Th; however, continuing PTH administration for an additional 35 days resulted in no differences in these parameters (83). Hirano and colleagues (71) also reported no difference in trabecular parameters when rabbits were treated with 40 μg/kg/d for 20 weeks. We observed higher Tb.N in PTH and, similar to OVX, CI values suggest a change in BV/TV cannot be ruled out.

This study has several limitations. First, while our group sizes (n=7) match the scale utilized in previous characterizations of the rabbit for trabecular bone and cortical geometry/density (152, 153, 161, 162), a great deal of variation was observed for many parameters, including outliers. Given there were no grounds to exclude them, all outliers were retained within our quantitative analyses. These factors ultimately limited our statistical power and certainly contributed to the uncertainty in a number of parameter changes despite considerable fold changes. Caution is thus warranted when determining significance of changes based upon p values alone, particularly where adjustments to α for multiple tests can make these comparisons occur on a very small scale. Consideration of CIs adds important contextual information but it must also be recognized that CIs are directly related to α. The necessity of additional tests to calculate adjusted CI and discrepancies detected with the primary statistical tests further highlight the perils of relying strictly on p value for analysis. As already noted, sample size limitations were further exacerbated by the lack of labelling in the GC-dosed groups and the low numbers of double labelled osteons in OVX and SHAM. Second, for our micro-CT analysis, we employed an imaging resolution (10 μm voxels) that was effective at detecting porosity on the scale of remodeling-related resorption spaces; however, it was insufficient to detect all vascular-level cortical porosity in rabbit bone (Supplemental Figure 3.81). Further, while this approach was effective at detecting resorption spaces, it is not exclusive to them and larger canals that were not actively remodeling as well as some of the porosity associated with endosteal bone formation (particularly evident in the PTH group) contributed to the overall Ct.Po measure. While the lack of bone formation observed within the GC-dosed groups is consistent with uncoupling within the BMU associated with GC treatment reported by Andreasen and colleagues (133), the shift towards larger sizes suggests a further disruption of BMU regulation through either a coalescence of resorption spaces (initiation and/or steering) or an increase in the size of individual spaces. Turning to our histological measures, a limitation of our measure of Rs.N/Ct.Ar and hence also a.Rm.Cr/Ct.Ar, was the fact that not all large spaces observed in the histological images could be confirmed as actively resorbing at the end of the experiment. This was particularly the case for the OVX groups (OVX and OVX+GC) which had a longer timeframe during which remodeling could be initiated and potentially halted/uncoupled. That said, due to our inclusion of only those spaces with roughly eroded surfaces, no lamellar bone formation, and no calcein labelling, it is a fair assumption that these spaces overwhelmingly represented *recently* active events induced by OVX and/or subsequent dosing. A more refined delineation of pores (i.e.., eroded, mixed eroded and formative, formative and quiescent pores) has recently been described (180) and presents a potential path forward for estimating the relative size/duration of the different phases of the BMU through their relative occurrences in 2D section. Such analysis paired with 3D morphological analysis of BMUs by micro-CT hold great potential for advancing our understanding of BMU spatio-temporal coordination. Expanding analysis beyond pores to the vasculature contained within them also holds great potential (181) as factors like age and corticosteroids reduce bone perfusion while PTH has been shown to increase it (182). Finally, a detailed analysis of the biomechanical impacts of increased porosity

was beyond the scale of this study. The non-uniform distribution of porosity indicates that careful consideration of sampling sites would be critical in examining the impact of these models on bone material properties.

3.5. Conclusion

Our findings indicate that Ct.Po was elevated many fold for all treatments with the caveat that the data were the least robust for GC. Histomorphometric measures supported the hypothesis that remodeling rate was elevated in all groups with, again, GC exhibiting the least robust of the findings. For trabecular bone, a pattern of loss was observed for OVX, GC, and OVX+GC groups, while the opposite was observed for PTH. The viability of the OVX model, in particular, adds new evidence to the conflicted literature. Overall, our results are encouraging for the further exploration of the role of cortical bone loss in OP using rabbits and highlight the need to consider both cortical and trabecular changes when looking at systemic bone loss. These rabbit models also have great potential to serve as a platform for more detailed analyses of BMU spatio-temporal coordination and the balance between bone resorption and formation within individual remodeling events which cumulatively determine skeletal health. In this pursuit, *in vivo* imaging (33, 39) will certainly prove illuminating.

3.6. Supplementary Materials

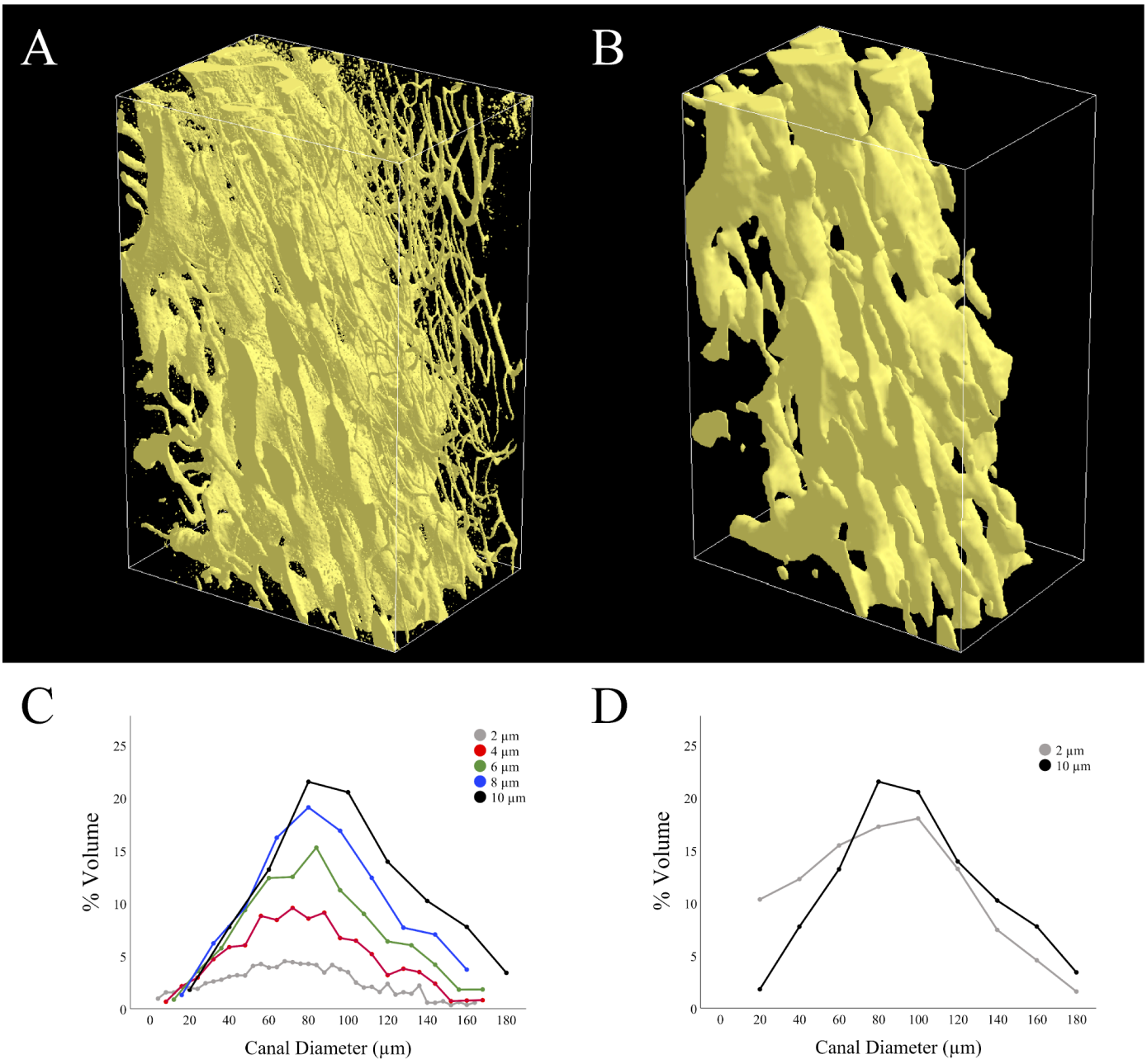

Figure 3.81. Micro-CT Canal Diameter Resolution Dependency. A block of distal tibial cortical bone (1.5 mm x 3.0 mm) from a PTH animal was imaged at 2, 4, 6, 8, and 10 µm voxel using the instrument and protocols described in the materials and methods. 3D renders of a matching volume of interest from the highest (2 µm; A) and lowest resolutions (10 µm; B) are depicted. The size of the bounding boxes around the render is approximately 950 x 1300 x 2250 µm. Below, % volume distributions of canal diameter (Ca.Dm) (comparable to Figure 3D) are plotted for all resolutions (C) and for just the highest and lowest resolutions with the former histogram data rescaled to match the latter (D). At 2 µm, there is intermittent detection of osteocyte lacunae as well as detection of quiescent primary and secondary canals whereas at

10 μm only the largest of pores, corresponding to active or recently active remodeling centers, were resolved. The pore size distributions quantitatively reflect what was visible in the 3D renders. As resolution was reduced, there was a loss of smaller pores and thus larger pores increasingly dominated the % volume distributions. Since the higher resolutions have smaller histogram bins (C) the contributions of each of these is relatively smaller, explaining the upward trend in percentages evident. When the histogram bin sizes were rescaled (C) it was clearly apparent that the higher resolution had a larger % contribution of smaller canals than the lower resolution scan. Notably, however, both distributions had a peak at the expected (~100 μm) size of normal rabbit secondary osteon diameter. Our analysis proceeded with the 10 μm voxel size as it afforded good characterization of remodeling-related pores, maximized field of view, minimized data size and, ultimately, exceeded resolutions previously employed to characterize cortical porosity in rabbit bone by micro-CT (see materials and methods).

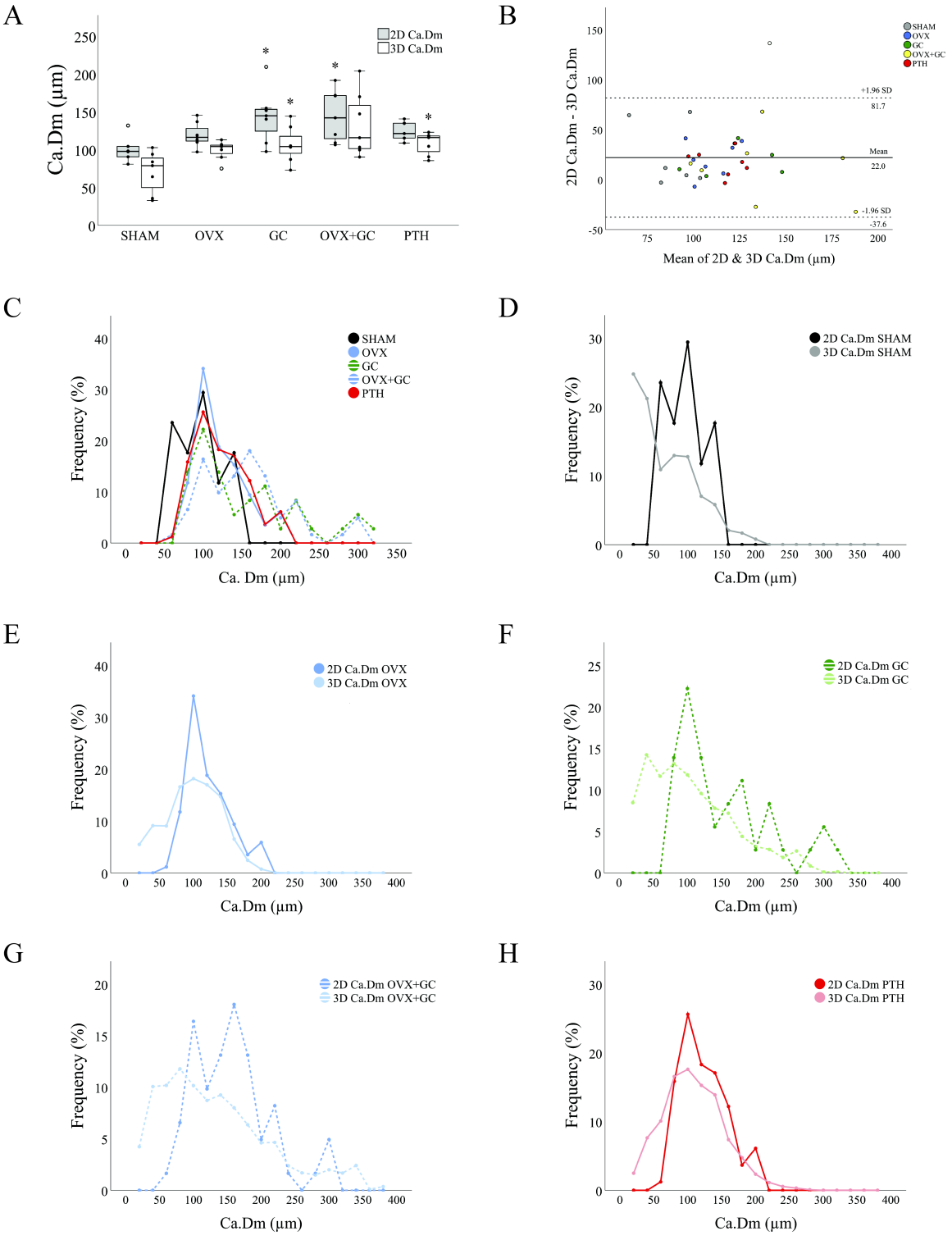

Figure 3.82. Validation of Micro-CT Assessment of Canal Diameter. To validate 3D micro-CT based measurements of Ca.Dm, the size (Feret's diameter) of up to 20 resorption cavities from each animal was assessed manually in 2D from the confocal DIC images using ImageJ.

Matching the analysis presented in the manuscript, mean 2D Ca.Dm was assessed by ANOVA with pairwise post-hoc tests against SHAM. As depicted in A, 2D Ca.Dm was greater than SHAM for GC, OVX+GC, and PTH – an overall result very similar to that of 3D Ca.Dm with the exceptions that GC was significant in 2D and not 3D and PTH was significant in 3D but not 2D. Bland-Altman plots revealed a significant but expected bias between the approaches with the 3D micro-CT measure generating lower values (22.0, one sample *t* test vs. 0, $p < 0.001$) due to the inclusion of canals ranging from the maximum diameter of cutting-cones down to the limits of the 10 μm nominal resolution (see Supplemental Figure 1). While different, the two approaches produced significantly correlated results ($r = 0.474$, $p < 0.005$ overall; $r = 0.668$, $p < 0.001$ with the exclusion of the outlier evident in B; Pearson's, $p < 0.01$). Superimposed distributions of Ca.Dm from the experimental groups (C) were strikingly similar to the 3D equivalent shown in Figure 3 D. Superimposed distribution plots for the individual groups (D-H) clearly demonstrate the similarity of the two techniques with the 3D measure having a larger % volume contribution of smaller canal diameters. As noted for the 3D analysis in the manuscript, peaks at the expected size of 100 μm size of normal rabbit secondary osteons were observed in all groups except for those dosed with GC. These had distributions skewed towards larger canal diameters. Given the similarity between these approaches, despite fundamental differences in what they specifically measure, we have confidence in the validity of the 3D outcomes.

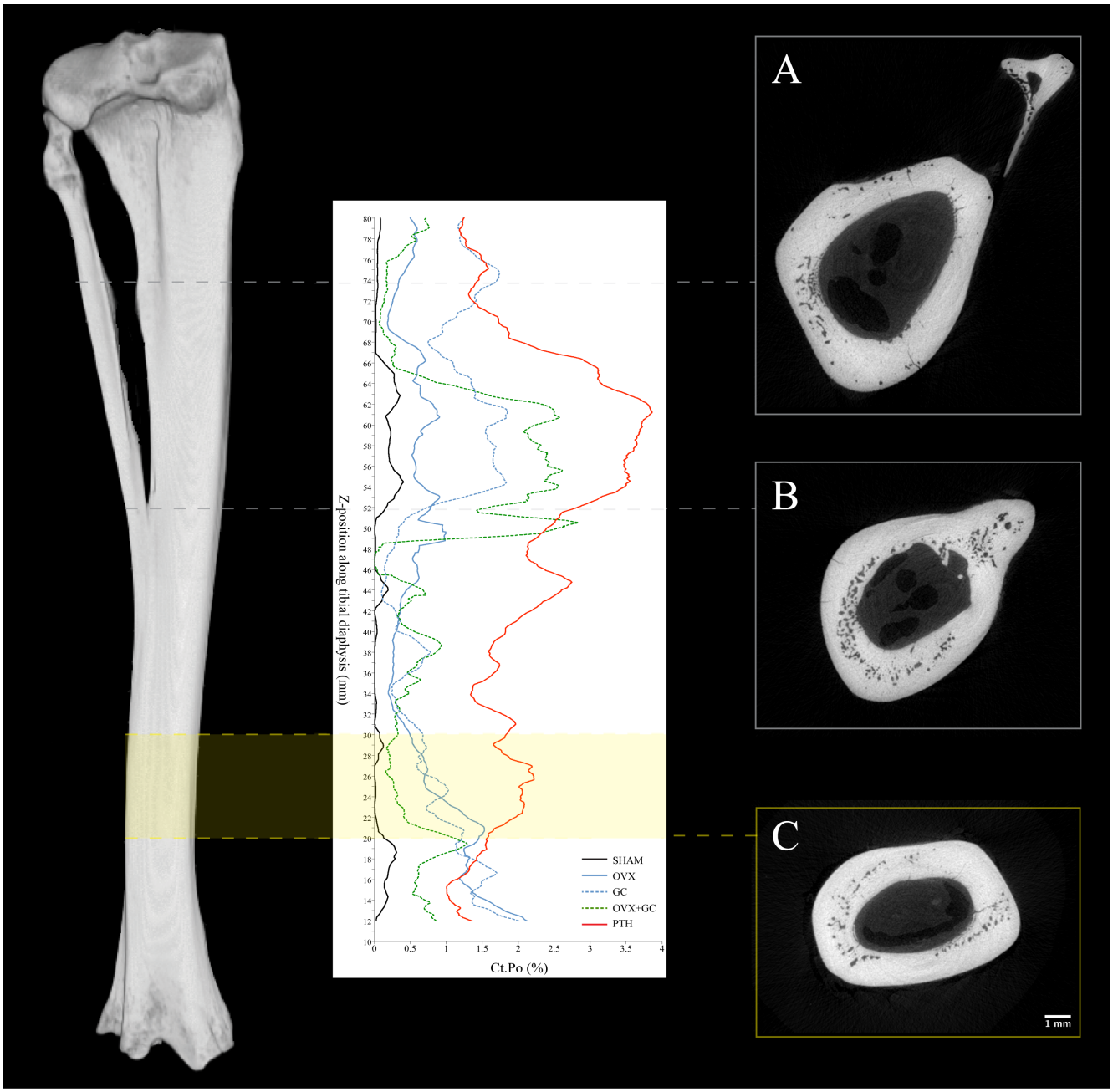

Figure 3.83. Variation in Cortical Porosity Within the Tibial Diaphysis. We explored variation in cortical porosity along the tibial diaphysis in order to select the optimal site for analysis, balancing the goals of suitability for future *in vivo* imaging and maximizing the detection of porosity/remodeling. Left tibiae (contra-lateral to those analyzed in the manuscript) from two animals from each of our experimental groups were imaged along their entire diaphyseal lengths using the 10 μm resolution and protocol previously described in the materials and methods. The tibiae had to be bisected in order to fit into the scanner. The presented results recombine the data with the caveat that some minimal data were lost at the location of the cut, which was placed just distal to the tibio-fibular junction. Mean percent cortical porosity (Ct.Po, %) for the two animals from each group was plotted relative to the position along the diaphysis starting at 1 cm from distal tibial plafond. A 200-slice (2 mm) rolling average was

utilized to reduce noise and better facilitate comparisons across groups. Representative 2D cross-sectional images along the diaphysis are presented for context (*A*-*C*; scale bar = 1 mm). The pattern was similar across groups despite variation in the overall level of Ct.Po. Porosity was lowest in the mid-diaphysis and increased proximally and distally. At the point of the tibio-fibular junction Ct.Po increased markedly and continued to do so proximally before eventually declining towards the proximal epiphysis. Considering suitability for *in vivo* imaging, overall porosity level, and anatomical complexity (e.g., one *vs*. two bones), the distal tibia ultimately presented the best overall target for our analysis. The variation along and within the diaphyses was intriguing and warrants further analysis regarding the factors underpinning it (e.g., mechanical versus developmental).

CHAPTER 4. Conclusion

4.1. Thesis Overview

Despite the growing recognition of cortical bone remodeling and microarchitecture in osteoporosis, our knowledge of the spatio-temporal behaviour of BMUs is limited, and therefore fundamental aspects of bone remodeling remain poorly understood. The emergence of high resolution imaging tools like micro-CT have enabled us to assess cortical porosity and move away from predominantly trabecular focused studies given the growing recognition of the role cortical bone microarchitecture plays in bone loss and fragility. Combining synchrotron radiation micro-CT imaging with the appropriate animal model has the potential to directly track individual BMUs *in vivo* and permit us to gain novel insight into the coordination of remodeling events. Animal models are essential for the study of the factors that affect bone remodeling and contribute to the pathogenesis of OP. The rabbit in particular, is a suitable animal model for *in vivo* imaging because it is the smallest laboratory animals to exhibit bone remodeling. Because remodeling rates are naturally low in normal rabbits, experimental approaches that increase cortical bone turnover are necessary in order to establish a viable model system. Parathyroid hormone has well-documented effects on cortical bone in rabbits, stimulating bone turnover to increase cortical porosity. The aim of this thesis was to develop a rabbit model of cortical porosity using PTH, one of which would be capable of advancing the study of bone remodeling and have the potential for 4D tracking of cortical porosity using synchrotron-based imaging *in vivo*.

Chapter 2 explored the effects of intermittent and continuous PTH administration on animal and human bone. The actions of PTH on bone seem to be dependent upon the mode of PTH administration (intermittent *vs*. continuous), duration of PTH administration, as well as the compartment (trabecular, cortical, endosteal, and periosteal) and site (vertebrae, tibia, etc.) of bone. It has been reported that intermittent PTH promotes bone formation on trabecular, endosteal, and periosteal bone surfaces, resulting in an increase in bone mass and an improvement in bone microarchitecture. This bone apposition has been associated with early modeling based bone formation, followed by remodeling and modeling based bone formation. Bone anabolism is mediated through actions on the osteoblastic cell lineage to increase osteoblast number and therefore bone formation. In addition to promoting bone apposition, intermittent PTH increases intracortical porosity by stimulating bone remodeling. In contrast to intermittent PTH administration, high circulating levels of PTH, as indicated in patients with PHPT, results in more deleterious changes in bone, mediated by pathways that prolong the action of osteoclasts. The cellular mechanisms that underlie the differential effects of PTH are currently not well understood, although it may be the case that different cellular mechanisms may be operating with each mode of administration, or at distinct bone sites. Studies evaluating the effects of intermittent PTH on rabbit bone have shown that their cortices respond to PTH with

increased turnover and intracortical porosity, which is ideal for establishing an animal model focused on cortical bone.

Chapter 3 presented the main study whose aim was to develop several rabbit based models of elevated cortical porosity, one of which was the focus of this thesis, the PTH rabbit model. Cortical porosity changes were characterized in several models of OP (OVX, GC, and OVX+GC) relative to a SHAM control and compared against the cortical bone microarchitecture of the PTH model. Trabecular microarchitecture in the proximal tibial epiphyses was assessed secondarily. Morphometric analyses by *ex vivo* micro-CT imaging and histomorphometry revealed Ct.Po to be substantially elevated in the tibiae of PTH rabbits relative to SHAM. This was associated with increases in bone remodeling rate (Ac.f), the number of actively resorbing and forming osteons (a.Rm.Cr), and cortical pore size (Ca.Dm), although the distribution of pore sizes revealed a similar peak to SHAM at 100 μm. OVX, OVX+GC, and GC rabbits exhibited a similar but less pronounced pattern of elevated porosity and remodeling, with GC having the least robust effect, likely due to high levels of variation in the results and a small sample size.

While losses were observed intracortically in the tibiae of PTH rabbits, the opposite effect appeared to occur within the trabecular compartment of the proximal epiphysis, as Tb.N and BV/TV were elevated and Tb.Sp was reduced, although these changes were more subtle than parameters of cortical bone remodeling. On the surfaces on cortical bone, histomorphometric analyses revealed extensive endosteal and periosteal bone formation, reflected qualitatively by prevalent calcein labelling and quantitatively by elevations in Es.MS/BS and Ps.MS/BS. A notable observation in these sections was the trabecularized appearance of some of the endosteal bone that had formed within a few of the PTH rabbits. This pattern is a typical feature of woven bone, however additional histological analyses (ie., collagen fiber orientation assessment with polarized light microscopy) would be needed to confirm its presence. Intracortically, PTH elevated the rate of new bone deposition within osteons, as indicated by an elevation in On.MAR relative to SHAM. Despite elevations in Ct.Po, the bending rigidity (I_{max}, I_{min}, Z_{pol}) of the cortex did not differ from SHAM, which may be associated with the bone apposition on the endosteal and periosteal bone surfaces as well as the non-uniform distribution of intracortical pores, but further biomechanical analyses are required to fully understand these effects.

In contrast to the PTH model, OVX, GC, and OVX+GC rabbits tended to lose bone in the trabecular compartment and on cortical bone surfaces. A pattern of bone loss was observed in OVX, GC, and OVX+GC groups evidenced by reductions in BV/TV for GC and OVX+GC groups and Tb.N for GC, OVX+GC, and OVX groups. A more subtle change in Tb.Sp in these groups also supported this pattern of loss. Pronounced scalloping of the endosteal surface of rabbit tibial cortices in GC dosed rabbits (GC, OVX+GC) was observed and image-based estimates of bone strength (I_{max}, I_{min}, Z_{pol}) in GC rabbit cortices were reduced. The latter result could be related to the smaller cortices (Ct.Ar) of the GC rabbits or the presence of intracortical pores. While all model systems exhibited evidence of intracortical bone loss to varying degrees, the 2D and 3D results indicate PTH induces bone remodeling that is quite distinct to that of OVX and GC models in terms of the porosity observed and the unique structural changes it produced

within various bone compartments. This is likely the result of variation in the mechanisms by which cortical porosity develops. For instance, PTH increases the rate of remodeling as well as the initiation of new BMUs to elevate porosity whereas BMU uncoupling (133) appears to be the predominant mechanism mediating GC-related bone loss as evidenced by a lack of calcein labelling and large intracortical pores within histological sections of GC dosed rabbits. Further exploration into these differences is required to better understand how BMU behaviour varies and how this variation impacts BMU morphology, which contributes to the resulting cortical bone structure. These results also highlight the importance of considering the bone as a whole when evaluating overall OP related bone loss.

Within this study, all rabbit based-models exhibited elevations in Ct.Po and cortical bone remodeling, with GC having the most varying effects in cortical bone, and PTH exhibiting the most dramatic effect in cortical bone. Parathyroid hormone was an ideal agent for developing a cortical bone model for this study because it was well tolerated by the rabbits and it induced the greatest level of porosity amongst the models within a relatively short time frame. Overall, the models described in this study are all good candidates for future longitudinal *in vivo* imaging to dynamically study their complex cortical networks. These models can serve as a platforms for further investigations into the intriguing effects that PTH, OVX, and GC impart on cortical and trabecular bone compartments and opens up new opportunities for mechanistic studies that test a number of hypotheses related to BMU regulation so we can better understand remodeling and its role in adaptation, aging, and disease.

4.2. Future Directions

The PTH rabbit model can be utilized to explore many avenues of research related to the bone remodeling process and other PTH effects in bone. One of the primary reasons for developing this model system was to establish a platform for which cortical bone remodeling events could be tracked by means of longitudinal synchrotron based micro-CT imaging. The rabbit model described in this thesis has now been implemented at the Canadian Light Source (CLS) on the BioMedical Imaging and Therapy Insertion Device beamline to achieve this goal and directly measure LER for the first time (manuscript in preparation). This was a project I had the opportunity to be involved in during my MSc program. In brief, distal rabbit tibiae were imaged *in vivo* at the CLS after 2 weeks of PTH dosing, dosed with PTH for an additional 2 weeks, and then imaged at the same region *ex vivo* using high-resolution conventional micro-CT. The two micro-CT scans were then co-registered using 3D data analysis software, so that LER could be directly measured from individual BMU related resorption spaces. LER was measured as the distance between the cutting cones at Time 1 and Time 2 (Figure 1.5). This study not only contributes to our basic understanding of bone remodeling by directly measuring cutting cone advance for the first time, but this platform allows us to better understand how PTH affects the coordination of bone remodeling events, since it is being utilized to induce bone turnover. This is clinically significant since PTH is both an anabolic treatment for OP when administered intermittently and a cause for secondary OP with high circulating levels. Results from this study

can be applied to designing future longitudinal experiments aimed at investigating specific aspects of the bone remodeling process as well as the physiological mechanisms underlying PTH's intriguing effects on bone. Some of these potential experiments utilizing this platform could involve:

- Studying the impacts of mechanical loading on BMU behaviour. It has been speculated that BMU activity is influenced by mechanical stimuli as the orientation of secondary osteons have been shown to align with the principal stresses of long bones (183). Furthermore, it has been proposed that cortical bone remodeling may be initiated by micro-damage induced by repetitive mechanical loads and that BMUs actively "steer" towards these areas to remove damage (184, 185). To test this hypothesis and evaluate the impact of mechanical loading and overloading on BMU coordination, PTH could be employed to induce a wave of remodeling in rabbits before altering the mechanical load. Rabbits dosed with PTH could be imaged *in vivo* immediately before manipulation of the mechanical load and *ex vivo* after a period of adaptation. This methodology would facilitate the direct tracking of existing BMUs present at the time of intervention so that any changes in their behaviour or orientation that occurred in response to various mechanical stimuli, could be quantified. Intrinsic mechanical loading could be applied by exercising previously sedentary PTH rabbits. Mechanical overloading could be achieved by axial loading of the tibia to produce micro-damage. To date, axial loading in rabbits has only been achieved in the forelimb (186), so this model would need to be adapted to the tibia. In the case of the axial loaded model, longitudinal imaging would indicate if existing BMUs alter their trajectories to target micro-damage induced by overloading.
- Studying the impact of mechanical unloading on BMU behaviour. On the other end of the loading spectrum, a lack of loading, or unloading, has been shown to increase cortical remodeling resulting in bone loss, as seen in individuals who experience prolonged therapeutic bed rest or are in weightless environments (ie., spaceflight) (187). To assess BMU activity in response to reduced mechanical loads, PTH rabbits would be imaged *in vivo* before undergoing single limb immobilization, which can be achieved through casting or neurogenic paralysis of the hindlimb (188). Similar to the loading experiments, tibiae would be then be imaged *ex vivo* after a period of adaption. The results from such a study would shed light on the mechanisms that underpin unloading associated bone loss.
- Assessing BMU behaviour in response to injury. Related to the mechanical loading and unloading experiments above, one could test the hypothesis that BMUs alter their course through bone tissue to target localized injury induced in PTH rabbits. A cortical bone defect could be produced in the tibia of a PTH rabbit by osteotomy using a surgical drill (189). Alternatively, injury in the form of a surgical implant or by selective irradiation could be utilized. Longitudinal

imaging during the healing period would determine if BMUs are directed towards regions of localized injury and provide more insight into the mechanisms that are involved in bone repair.

- Investigating PTH's distinct effects on bone compartments by manipulating the duration and frequency of PTH administration and imaging rabbits *in vivo*. One example could include assessing effects of once daily PTH, once weekly PTH, and continuous PTH on bone in 3D and 4D. The latter would involve developing a model of hyperparathyroidism in the rabbit. Currently, PHPT has only been induced in rabbits by a high phosphate diet (121, 122) although, cortical bone microarchitecture in these models have not yet been extensively characterized. Hyperparathyroidism has been induced in mice and rats by continuous PTH administration using subcutaneous infusion pumps (109, 111) or through the generation of transgenic models (190), so there is a potential of utilizing these interventions to induce the disease in rabbits in future studies.
- Imaging PTH dosed rabbits *in vivo* at multiple time points to detect changes in porosity and cortical geometry over time in order to evaluate the temporal nature of PTH bone effects. One could test the hypothesis that bone formation induced by PTH would be maximal at early time points during the experiment, which would provide compelling evidence for the concept of the "anabolic window" that is said to occur early in treatment (92, 93).
- Studying the effect of PTH withdrawal on BMU progression and cortical bone microarchitecture. This project has recently been undertaken in our lab utilizing the PTH dosed rabbit model and longitudinal synchrotron radiation based imaging platform. Using the dosing protocol described in this thesis, rabbit tibiae were imaged at the CLS *in vivo* after being dosed with PTH for two weeks. Half of the rabbit cohort then ceased PTH administration while the other half continued with the same dosing regimen for an additional two weeks. After this time, rabbit tibiae were imaged at the same region *ex vivo*, with desktop micro-CT. From this study, one can determine if PTH withdrawal alters the rate of BMU progression, which not only provides more insight into the bone remodeling process but also holds great clinical significance, as treatment discontinuation and long-term effects are important factors to take into consideration with OP treatments. OP patients who take teriparatide as an anabolic treatment are only permitted to take it for up to 2 years (11). There is a lack of consensus in the literature regarding the effects of PTH withdrawal on bone such that one clinical study has reported a decline in BMD in post-menopausal women after teriparatide discontinuation (191), while another found a sustained reduction in vertebral fracture risk in post-menopausal women 18 months after ceasing teriparatide treatment (192). Although limited in duration, this study would yield novel 3D and 4D information on how PTH withdrawal

impacts cortical bone remodeling, which could be applied to developing efficient OP therapies that improve long term therapeutic outcomes and limit adverse effects related to treatment discontinuation.

- Producing a more clinically relevant model system by dosing OVX rabbits with PTH at a dose similar to what is given in the anabolic treatment of OP (teriparatide, 20 ug/ day (11)) and then imaging rabbits at different time points to assess PTH effects in a model of primary cortical bone loss (postmenopausal OP). This would help us understand the mechanisms by which PTH acts so that we can optimize current treatments or design novel therapeutic interventions to more precisely control bone remodeling and to maximize anabolic effects.
- Imaging rabbits dosed with PTH in combination or in sequence with an anti-resorptive agent like bisphosphonate, to permit a greater understanding of the action of current OP therapeutic interventions on bone. Combined therapy (193) and sequential therapy (194) with PTH are more recent therapeutic approaches to combat bone loss in OP patients and results from such studies could be compared and contrasted against monotherapy.

In addition to longitudinal imaging studies, the PTH dosed rabbit model could also be utilized to quantify 2D parameters of bone remodeling by means of histology, such as measuring closing cone advance and reproducing the histological measure of LER from the classic studies from the 1970s (28, 29). Histological LER could be quantified in both the PTH dosed rabbit model and in the SHAM control to compare against previously established measures. Additionally, these values could also be compared against direct measures of LER from the same animal to assess the validity of the measure. In order to measure LER in 2D, serial longitudinal sectioning of undecalcified bone is required for morphometric evaluation. I have worked on optimizing the methodology for this protocol during my Master's program for the quantification of histological LER (Appendix A), but this technique can also be applied to any future cellular analyses requiring thin sections. The two techniques I have focused on optimizing is physical sectioning, where an entire section of bone is cut into very thin sections of 5-10 μm thickness, and optical sectioning, where sequential images are taken throughout the region of interest to produce an image stack. Physical sectioning can be achieved through plastic or frozen bone sectioning. Plastic sectioning requires undecalcified bones to be embedded in a medium that is similar to the hardness of bone, like methylmethacrylate (MMA) before being thinly sectioned using an automated heavy-duty rotary microtome. Sections are then mounted on glass slides for analysis. Methylmethacrylate is optimal for LER analysis because it preserves and supports the 2D and 3D structure of bone tissue, permits the visualization of fluorescent labels, and exhibits minimal auto-fluorescence during imaging (195). Frozen sectioning, also known as cryosectioning, requires bone to be embedded into a frozen block before being thinly sectioned with a cryostat and transferred onto glass slides. The sections produced with either technique are then imaged with a microscope possessing fluorescent capabilities and visualized in 3D by rendering the image stack. Alternatively, optical sectioning can achieve similar results, having

the advantage of being minimally destructive in comparison to physical sectioning. By utilizing the z-stack imaging tool on the confocal microscope (taking images along the z dimension of a bone), one can create a 3D render from the stack of images taken from a thick section of bone. With this technique, the bone is best preserved by first being embedded in MMA before being cut into a thick section and then mounted on a glass slide. These protocols are described in more detail in Appendix A. Reproducing the measure of histological LER using the sectioning techniques described above would provide a means for analyzing osteoblastic and osteoclastic activity at the tissue level, which is informative for our understanding of bone remodeling dynamics, especially if histological sections can be matched to a 3D micro-CT scan of the same BMU related resorption space.

Aside from being employed in studies characterizing dynamic properties of BMU activity, the PTH dosed rabbit could be used to further characterize some of the interesting bone structural outcomes observed within these rabbits. Future studies investigating the role the unique endosteal bone formation and the non-uniform distribution of cortical porosity plays in determining the overall strength of bone would be useful, considering the level of porosity induced by PTH. Currently, our lab is investigating this by performing image based biomechanical analyses on sections of the tibiae from this rabbit model. Future studies could also focus on characterizing the morphology of BMU related resorption spaces created by PTH and associated vasculature, since PTH induced remodeling that was quite distinct from the other rabbit OP models, and these morphologies could be compared to those of GC and OVX rabbits. Within the tibiae of PTH dosed rabbits, we observed BMUs of various morphologies including classic cutting cones as well as highly branched clusters. Since morphology is a direct outcome of osteoclastic and osteoblastic activity, morphological analyses of BMUs in this model may provide additional lines of evidence for some of the PTH driven alterations in bone remodeling that are thought to occur, for instance, the shape of a BMU related resorption space in this model may indicate an increased rate of closing cone advance. Finally, it would be interesting to assess the same bone microarchitectural parameters analyzed in the main study in different bones within the rabbit, like the femur and humerus, to determine if there are any site specific effects or variation in porosity within this rabbit model.

Overall, this thesis introduced a highly reproducible and efficient experimental cortical bone model in the rabbit using PTH, as apart of a larger study surveying rabbit-based models of elevated cortical bone remodeling, thereby establishing a platform for studying how cortical porosity develops and how it may contribute to the pathogenesis of OP. The information gained from this thesis will inform future studies investigating BMU regulation and variation as well as the mechanisms underlying the complex and multifaceted effects of PTH on bone microarchitecture, which together, will be transformative for bone biology.

REFERENCES

1. Burr DB, Akkus O. Chapter 1 - Bone Morphology and Organization. In: Burr DB, Allen MR, editors. Basic and Applied Bone Biology. San Diego: Academic Press; 2014. p. 3-25.
2. Martin RB, Burr DB, Sharkey NA, Fyhrie DP. Growth, Modeling and Remodeling of Bone. Skeletal Tissue Mechanics. New York, NY: Springer New York; 2015. p. 95-173.
3. Frost HM. Bone "mass" and the "mechanostat": a proposal. Anat Rec. 1987;219(1):1-9.
4. Frost HM. Tetracycline-based histological analysis of bone remodeling. Calcified Tissue Research. 1969;3(1):211-37.
5. Cooper DM, Matyas JR, Katzenberg MA, Hallgrimsson B. Comparison of microcomputed tomographic and microradiographic measurements of cortical bone porosity. Calcif Tissue Int. 2004;74(5):437-47.
6. Currey JD. Bones: structure and mechanics: Princeton university press; 2006.
7. Raggatt LJ, Partridge NC. Cellular and molecular mechanisms of bone remodeling. The Journal of biological chemistry. 2010;285(33):25103-8.
8. Parfitt AM. Osteonal and hemi-osteonal remodeling: the spatial and temporal framework for signal traffic in adult human bone. J Cell Biochem. 1994;55(3):273-86.
9. Sims NA, Martin TJ. Coupling the activities of bone formation and resorption: a multitude of signals within the basic multicellular unit. Bonekey Rep. 2014;3:481-.
10. Rochefort GY. The osteocyte as a therapeutic target in the treatment of osteoporosis. Ther Adv Musculoskelet Dis. 2014;6(3):79-91.
11. Osteoporosis Canada [Available from: https://osteoporosis.ca/about-the-disease/what-is-osteoporosis/.
12. Bartl Ra, Bartl R. Osteoporosis : Diagnosis, Prevention, Therapy. Second Revised Edition.. ed. Frisch Ba, SpringerLink, Frisch B, editors2009.
13. Fitzpatrick LA. Secondary Causes of Osteoporosis. Mayo Clinic Proceedings. 2002;77(5):453-68.
14. Hopkins RB, Burke N, Von Keyserlingk C, Leslie WD, Morin SN, Adachi JD, et al. The current economic burden of illness of osteoporosis in Canada. Osteoporos Int. 2016;27(10):3023-32.
15. Akhter MP, Lappe JM, Davies KM, Recker RR. Transmenopausal changes in the trabecular bone structure. Bone. 2007;41(1):111-6.
16. Dempster DW, Birchman R, Xu R, Lindsay R, Shen V. Temporal changes in cancellous bone structure of rats immediately after ovariectomy. Bone. 1995;16(1):157-61.
17. Bala Y, Zebaze R, Seeman E. Role of cortical bone in bone fragility. Current Opinion in Rheumatology. 2015;27(4):406-13.
18. Cooper DML, Thomas CDL, Clement JG, Turinsky AiL, Sensen CW, Hallgrímsson B. Age-dependent change in the 3D structure of cortical porosity at the human femoral midshaft. Bone. 2007;40(4):957-65.

19. Zebaze R, Seeman E. Cortical bone: a challenging geography. J Bone Miner Res. 2015;30(1):24-9.
20. Poole KE, Treece GM, Mayhew PM, Vaculik J, Dungl P, Horak M, et al. Cortical thickness mapping to identify focal osteoporosis in patients with hip fracture. PLoS One. 2012;7(6):e38466.
21. Zebaze RMD, Ghasem-Zadeh A, Bohte A, Iuliano-Burns S, Mirams M, Price RI, et al. Intracortical remodelling and porosity in the distal radius and post-mortem femurs of women: a cross-sectional study. The Lancet. 2010;375(9727):1729-36.
22. Seeman E, Martin TJ. Co-administration of antiresorptive and anabolic agents: a missed opportunity. J Bone Miner Res. 2015;30(5):753-64.
23. Adler RA. Bisphosphonates and atypical femoral fractures. Current Opinion in Endocrinology, Diabetes and Obesity. 2016;23(6):430-4.
24. Yoneda T, Hagino H, Sugimoto T, Ohta H, Takahashi S, Soen S, et al. Antiresorptive agent-related osteonecrosis of the jaw: Position Paper 2017 of the Japanese Allied Committee on Osteonecrosis of the Jaw. J Bone Miner Metab. 2017;35(1):6-19.
25. Fung P, Bedogni G, Bedogni A, Petrie A, Porter S, Campisi G, et al. Time to onset of bisphosphonate-related osteonecrosis of the jaws: a multicentre retrospective cohort study. Oral Diseases. 2017;23(4):477-83.
26. Mosca L, Grady D, Barrett-Connor E, Collins P, Wenger N, Abramson BL, et al. Effect of raloxifene on stroke and venous thromboembolism according to subgroups in postmenopausal women at increased risk of coronary heart disease. Stroke. 2009;40(1):147-55.
27. Recker RR. Bone histomorphometry. Techniques and interpretation. 1983.
28. Jaworski ZF, Lok E. The rate of osteoclastic bone erosion in Haversian remodeling sites of adult dog's rib. Calcif Tissue Res. 1972;10(2):103-12.
29. H T, H N. The Longitudianal and transverse rate of resorption of the Haversian system in canine bone. In Bone Morphometry. 1976:143.
30. van Oers RF, Ruimerman R, Tanck E, Hilbers PA, Huiskes R. A unified theory for osteonal and hemi-osteonal remodeling. Bone. 2008;42(2):250-9.
31. Martínez-Reina J, García-Aznar JM, Domínguez J, Doblaré M. A bone remodelling model including the directional activity of BMUs. Biomechanics and Modeling in Mechanobiology. 2009;8(2):111-27.
32. Kameo Y, Adachi T, Hojo M. Effects of loading frequency on the functional adaptation of trabeculae predicted by bone remodeling simulation. Journal of the Mechanical Behavior of Biomedical Materials. 2011;4(6):900-8.
33. Harrison KD, Cooper DM. Modalities for Visualization of Cortical Bone Remodeling: The Past, Present, and Future. Front Endocrinol (Lausanne). 2015;6:122.
34. Ford NL, Thornton MM, Holdsworth DW. Fundamental image quality limits for microcomputed tomography in small animals. Med Phys. 2003;30(11):2869-77.

35. Cheung AM, Adachi JD, Hanley DA, Kendler DL, Davison KS, Josse R, et al. High-resolution peripheral quantitative computed tomography for the assessment of bone strength and structure: a review by the Canadian Bone Strength Working Group. Curr Osteoporos Rep. 2013;11(2):136-46.
36. Geusens P, Chapurlat R, Schett G, Ghasem-Zadeh A, Seeman E, de Jong J, et al. High-resolution in vivo imaging of bone and joints: a window to microarchitecture. Nature Reviews Rheumatology. 2014;10(5):304-13.
37. Burghardt AJ, Kazakia GJ, Sode M, de Papp AE, Link TM, Majumdar S. A longitudinal HR-pQCT study of alendronate treatment in postmenopausal women with low bone density: Relations among density, cortical and trabecular microarchitecture, biomechanics, and bone turnover. J Bone Miner Res. 2010;25(12):2558-71.
38. Wong AK. A comparison of peripheral imaging technologies for bone and muscle quantification: a technical review of image acquisition. Journal of musculoskeletal & neuronal interactions. 2016;16(4):265-82.
39. Pratt IV, Belev G, Zhu N, Chapman LD, Cooper DM. In vivo imaging of rat cortical bone porosity by synchrotron phase contrast micro computed tomography. Phys Med Biol. 2015;60(1):211-32.
40. Zhou S-A, Brahme A. Development of phase-contrast X-ray imaging techniques and potential medical applications. Physica Medica: European Journal of Medical Physics. 2008;24(3):129-48.
41. Bonucci E, Ballanti P. Osteoporosis-bone remodeling and animal models. Toxicol Pathol. 2014;42(6):957-69.
42. Reinwald S, Burr D. Review of nonprimate, large animal models for osteoporosis research. J Bone Miner Res. 2008;23(9):1353-68.
43. Turner AS. Animal models of osteoporosis--necessity and limitations. Eur Cell Mater. 2001;1:66-81.
44. Pazzaglia UE, Zarattini G, Giacomini D, Rodella L, Menti AM, Feltrin G. Morphometric analysis of the canal system of cortical bone: An experimental study in the rabbit femur carried out with standard histology and micro-CT. Anat Histol Embryol. 2010;39(1):17-26.
45. Sietsema WK. Animal models of cortical porosity. Bone. 1995;17(4 Suppl):297S-305S.
46. Gilsanz V, Roe TF, Gibbens DT, Schulz EE, Carlson ME, Gonzalez O, et al. Effect of sex steroids on peak bone density of growing rabbits. American Journal of Physiology-Endocrinology and Metabolism. 1988;255(4):E416-E21.
47. Martin RB. On the histologic measurement of osteonal BMU activation frequency. Bone. 1994;15(5):547-9.
48. Silva BC, Costa AG, Cusano NE, Kousteni S, Bilezikian JP. Catabolic and anabolic actions of parathyroid hormone on the skeleton. J Endocrinol Invest. 2011;34(10):801-10.
49. Canalis E, Giustina A, Bilezikian JP. Mechanisms of anabolic therapies for osteoporosis. N Engl J Med. 2007;357(9):905-16.

50. Huang JC, Sakata T, Pfleger LL, Bencsik M, Halloran BP, Bikle DD, et al. PTH differentially regulates expression of RANKL and OPG. J Bone Miner Res. 2004;19(2):235-44.
51. Osagie-Clouard L, Sanghani A, Coathup M, Briggs T, Bostrom M, Blunn G. Parathyroid hormone 1-34 and skeletal anabolic action: The use of parathyroid hormone in bone formation. Bone Joint Res. 2017;6(1):14-21.
52. Selye H. ON THE STIMULATION OF NEW BONE-FORMATION WITH PARATHYROID EXTRACT AND IRRADIATED ERGOSTEROL. Endocrinology. 1932;16(5):547-58.
53. Macdonald HM, Nishiyama KK, Hanley DA, Boyd SK. Changes in trabecular and cortical bone microarchitecture at peripheral sites associated with 18 months of teriparatide therapy in postmenopausal women with osteoporosis. Osteoporos Int. 2011;22(1):357-62.
54. Ma YL, Zeng QQ, Chiang AY, Burr D, Li J, Dobnig H, et al. Effects of teriparatide on cortical histomorphometric variables in postmenopausal women with or without prior alendronate treatment. Bone. 2014;59:139-47.
55. Jiang Y, Zhao JJ, Mitlak BH, Wang O, Genant HK, Eriksen EF. Recombinant Human Parathyroid Hormone (1–34) [Teriparatide] Improves Both Cortical and Cancellous Bone Structure. Journal of Bone and Mineral Research. 2003;18(11):1932-41.
56. Neer RM, Arnaud CD, Zanchetta JR, Prince R, Gaich GA, Reginster J-Y, et al. Effect of Parathyroid Hormone (1-34) on Fractures and Bone Mineral Density in Postmenopausal Women with Osteoporosis. New England Journal of Medicine. 2001;344(19):1434-41.
57. Lindsay R, Cosman F, Zhou H, Bostrom MP, Shen VW, Cruz JD, et al. A novel tetracycline labeling schedule for longitudinal evaluation of the short-term effects of anabolic therapy with a single iliac crest bone biopsy: early actions of teriparatide. J Bone Miner Res. 2006;21(3):366-73.
58. Lindsay R, Zhou H, Cosman F, Nieves J, Dempster DW, Hodsman AB. Effects of a one-month treatment with PTH(1-34) on bone formation on cancellous, endocortical, and periosteal surfaces of the human ilium. J Bone Miner Res. 2007;22(4):495-502.
59. Dempster DW, Cosman F, Kurland ES, Zhou H, Nieves J, Woelfert L, et al. Effects of Daily Treatment with Parathyroid Hormone on Bone Microarchitecture and Turnover in Patients with Osteoporosis: A Paired Biopsy Study*. Journal of Bone and Mineral Research. 2001;16(10):1846-53.
60. Kotowicz M, Klee G, Kao P, O'Fallon W, Hodgson S, Cedel S, et al. Relationship between serum intact parathyroid hormone concentrations and bone remodeling in type I osteoporosis: Evidence that skeletal sensitivity is increased. Osteoporosis International. 1990;1(1):14-22.
61. Reeve J, Meunier PJ, Parsons JA, Bernat M, Bijvoet OL, Courpron P, et al. Anabolic effect of human parathyroid hormone fragment on trabecular bone in involutional osteoporosis: a multicentre trial. Br Med J. 1980;280(6228):1340-4.

62. Hodsman AB, Steer BM. Early histomorphometric changes in response to parathyroid hormone therapy in osteoporosis: Evidence for de novo bone formation on quiescent cancellous surfaces. Bone. 1993;14(3):523-7.
63. Cosman F, Dempster DW, Nieves JW, Zhou H, Zion M, Roimisher C, et al. Effect of Teriparatide on Bone Formation in the Human Femoral Neck. J Clin Endocrinol Metab. 2016;101(4):1498-505.
64. Orwoll ES, Scheele WH, Paul S, Adami S, Syversen U, Diez-Perez A, et al. The effect of teriparatide [human parathyroid hormone (1-34)] therapy on bone density in men with osteoporosis. J Bone Miner Res. 2003;18(1):9-17.
65. Nishiyama KK, Cohen A, Young P, Wang J, Lappe JM, Guo XE, et al. Teriparatide Increases Strength of the Peripheral Skeleton in Premenopausal Women With Idiopathic Osteoporosis: A Pilot HR-pQCT Study. The Journal of Clinical Endocrinology & Metabolism. 2014;99(7):2418-25.
66. Saag KG, Shane E, Boonen S, Marin F, Donley DW, Taylor KA, et al. Teriparatide or alendronate in glucocorticoid-induced osteoporosis. N Engl J Med. 2007;357(20):2028-39.
67. Yamamoto T, Hasegawa T, Sasaki M, Hongo H, Tsuboi K, Shimizu T, et al. Frequency of Teriparatide Administration Affects the Histological Pattern of Bone Formation in Young Adult Male Mice. Endocrinology. 2016;157(7):2604-20.
68. Oki Y, Doi K, Makihara Y, Kobatake R, Kubo T, Tsuga K. Effects of continual intermittent administration of parathyroid hormone on implant stability in the presence of osteoporosis: an in vivo study using resonance frequency analysis in a rabbit model. J Appl Oral Sci. 2017;25(5):498-505.
69. Ozer T, Baslarli O, Aktas A, Baris E, Celik HH, Ocak M. Locally administrated single-dose teriparatide affects critical-size rabbit calvarial defects: A histological, histomorphometric and micro-CT study. Acta Orthop Traumatol Turc. 2019;53(6):478-84.
70. Aleksyniene R, Eckardt H, Bundgaard K, Lind M, Hvid I. Effects of parathyroid hormone on newly regenerated bone during distraction osteogenesis in a rabbit tibial lengthening model. A pilot study. Medicina (Kaunas). 2006;42(1):38-48.
71. Hirano T, Burr DB, Turner CH, Sato M, Cain RL, Hock JM. Anabolic effects of human biosynthetic parathyroid hormone fragment (1-34), LY333334, on remodeling and mechanical properties of cortical bone in rabbits. J Bone Miner Res. 1999;14(4):536-45.
72. Bellido M, Lugo L, Castañeda S, Roman-Blas JA, Rufián-Henares JA, Navarro-Alarcón M, et al. PTH Increases Jaw Mineral Density in a Rabbit Model of Osteoporosis. Journal of Dental Research. 2010;89(4):360-5.
73. Brommage R, Hotchkiss CE, Lees CJ, Stancill MW, Hock JM, Jerome CP. Daily treatment with human recombinant parathyroid hormone-(1-34), LY333334, for 1 year increases bone mass in ovariectomized monkeys. J Clin Endocrinol Metab. 1999;84(10):3757-63.

74. Hansen S, Hauge EM, Beck Jensen JE, Brixen K. Differing effects of PTH 1-34, PTH 1-84, and zoledronic acid on bone microarchitecture and estimated strength in postmenopausal women with osteoporosis: an 18-month open-labeled observational study using HR-pQCT. J Bone Miner Res. 2013;28(4):736-45.
75. Hodsman AB, Kisiel M, Adachi JD, Fraher LJ, Watson PH. Histomorphometric evidence for increased bone turnover without change in cortical thickness or porosity after 2 years of cyclical hPTH(1-34) therapy in women with severe osteoporosis. Bone. 2000;27(2):311-8.
76. Obermayer-Pietsch BM, Marin F, McCloskey EV, Hadji P, Farrerons J, Boonen S, et al. Effects of two years of daily teriparatide treatment on BMD in postmenopausal women with severe osteoporosis with and without prior antiresorptive treatment. J Bone Miner Res. 2008;23(10):1591-600.
77. de Bakker CM, Altman AR, Tseng WJ, Tribble MB, Li C, Chandra A, et al. muCT-based, in vivo dynamic bone histomorphometry allows 3D evaluation of the early responses of bone resorption and formation to PTH and alendronate combination therapy. Bone. 2015;73:198-207.
78. Uzawa T, Hori M, Ejiri S, Ozawa H. Comparison of the effects of intermittent and continuous administration of human parathyroid hormone(1-34) on rat bone. Bone. 1995;16(4):477-84.
79. Sato M, Westmore M, Ma YL, Schmidt A, Zeng QQ, Glass EV, et al. Teriparatide [PTH(1–34)] Strengthens the Proximal Femur of Ovariectomized Nonhuman Primates Despite Increasing Porosity. Journal of Bone and Mineral Research. 2004;19(4):623-9.
80. Jerome CP, Burr DB, Van Bibber T, Hock JM, Brommage R. Treatment with human parathyroid hormone (1-34) for 18 months increases cancellous bone volume and improves trabecular architecture in ovariectomized cynomolgus monkeys (Macaca fascicularis). Bone. 2001;28(2):150-9.
81. Hock JM, Gera I. Effects of continuous and intermittent administration and inhibition of resorption on the anabolic response of bone to parathyroid hormone. Journal of Bone and Mineral Research. 1992;7(1):65-72.
82. Dobnig H, Turner RT. The Effects of Programmed Administration of Human Parathyroid Hormone Fragment (1–34) on Bone Histomorphometry and Serum Chemistry in Rats*. Endocrinology. 1997;138(11):4607-12.
83. Mashiba T, Burr DB, Turner CH, Sato M, Cain RL, Hock JM. Effects of human parathyroid hormone (1-34), LY333334, on bone mass, remodeling, and mechanical properties of cortical bone during the first remodeling cycle in rabbits. Bone. 2001;28(5):538-47.
84. Dempster DW, Compston JE, Drezner MK, Glorieux FH, Kanis JA, Malluche H, et al. Standardized nomenclature, symbols, and units for bone histomorphometry: a 2012 update of the report of the ASBMR Histomorphometry Nomenclature Committee.

Journal of bone and mineral research : the official journal of the American Society for Bone and Mineral Research. 2013;28(1):2-17.
85. Boyce RW, Paddock CL, Franks AF, Jankowsky ML, Eriksen EF. Effects of intermittent hPTH(1–34) alone and in combination with 1,25(OH)2d3 or risedronate on endosteal bone remodeling in canine cancellous and cortical bone. Journal of Bone and Mineral Research. 1996;11(5):600-13.
86. Yamamoto Y, Washimi Y, Kanaji A, Tajima K, Ishimura D, Yamada H. The effect of bisphosphonate and intermittent human parathyroid hormone 1-34 treatments on cortical bone allografts in rabbits. J Endocrinol Invest. 2012;35(2):139-45.
87. Burr DB, Hirano T, Turner CH, Hotchkiss C, Brommage R, Hock JM. Intermittently Administered Human Parathyroid Hormone(1–34) Treatment Increases Intracortical Bone Turnover and Porosity Without Reducing Bone Strength in the Humerus of Ovariectomized Cynomolgus Monkeys. Journal of Bone and Mineral Research. 2001;16(1):157-65.
88. Wronski TJ, Yen CF. Anabolic effects of parathyroid hormone on cortical bone in ovariectomized rats. Bone. 1994;15(1):51-8.
89. Yamane H, Takakura A, Shimadzu Y, Kodama T, Lee JW, Isogai Y, et al. Acute development of cortical porosity and endosteal naïve bone formation from the daily but not weekly short-term administration of PTH in rabbit. PLoS One. 2017;12(4):e0175329.
90. Ma YL, Zeng Q, Donley DW, Ste-Marie LG, Gallagher JC, Dalsky GP, et al. Teriparatide increases bone formation in modeling and remodeling osteons and enhances IGF-II immunoreactivity in postmenopausal women with osteoporosis. J Bone Miner Res. 2006;21(6):855-64.
91. Vrahnas C, Buenzli PR, Pearson TA, Pennypacker BL, Tobin MJ, Bambery KR, et al. Differing Effects of Parathyroid Hormone, Alendronate, and Odanacatib on Bone Formation and on the Mineralization Process in Intracortical and Endocortical Bone of Ovariectomized Rabbits. Calcif Tissue Int. 2018;103(6):625-37.
92. Bilezikian JP. Combination anabolic and antiresorptive therapy for osteoporosis: opening the anabolic window. Curr Osteoporos Rep. 2008;6(1):24-30.
93. Rubin MR, Bilezikian JP. The anabolic effects of parathyroid hormone therapy. Clin Geriatr Med. 2003;19(2):415-32.
94. Compston JE. Skeletal actions of intermittent parathyroid hormone: effects on bone remodelling and structure. Bone. 2007;40(6):1447-52.
95. Gatti D, Viapiana O, Idolazzi L, Fracassi E, Rossini M, Adami S. The waning of teriparatide effect on bone formation markers in postmenopausal osteoporosis is associated with increasing serum levels of DKK1. J Clin Endocrinol Metab. 2011;96(5):1555-9.
96. Nishida S, Yamaguchi A, Tanizawa T, Endo N, Mashiba T, Uchiyama Y, et al. Increased bone formation by intermittent parathyroid hormone administration is due to the

stimulation of proliferation and differentiation of osteoprogenitor cells in bone marrow. Bone. 1994;15(6):717-23.
97. Balani DH, Ono N, Kronenberg HM. Parathyroid hormone regulates fates of murine osteoblast precursors in vivo. J Clin Invest. 2017;127(9):3327-38.
98. Bellido T, Ali AA, Plotkin LI, Fu Q, Gubrij I, Roberson PK, et al. Proteasomal degradation of Runx2 shortens parathyroid hormone-induced anti-apoptotic signaling in osteoblasts. A putative explanation for why intermittent administration is needed for bone anabolism. J Biol Chem. 2003;278(50):50259-72.
99. Jilka RL, Weinstein RS, Bellido T, Roberson P, Parfitt AM, Manolagas SC. Increased bone formation by prevention of osteoblast apoptosis with parathyroid hormone. J Clin Invest. 1999;104(4):439-46.
100. Jilka RL, O'Brien CA, Ali AA, Roberson PK, Weinstein RS, Manolagas SC. Intermittent PTH stimulates periosteal bone formation by actions on post-mitotic preosteoblasts. Bone. 2009;44(2):275-86.
101. Kim SW, Pajevic PD, Selig M, Barry KJ, Yang JY, Shin CS, et al. Intermittent parathyroid hormone administration converts quiescent lining cells to active osteoblasts. J Bone Miner Res. 2012;27(10):2075-84.
102. Jilka RL, O'Brien CA, Bartell SM, Weinstein RS, Manolagas SC. Continuous elevation of PTH increases the number of osteoblasts via both osteoclast-dependent and -independent mechanisms. J Bone Miner Res. 2010;25(11):2427-37.
103. Bellido T, Ali AA, Gubrij I, Plotkin LI, Fu Q, O'Brien CA, et al. Chronic elevation of parathyroid hormone in mice reduces expression of sclerostin by osteocytes: a novel mechanism for hormonal control of osteoblastogenesis. Endocrinology. 2005;146(11):4577-83.
104. Keller H, Kneissel M. SOST is a target gene for PTH in bone. Bone. 2005;37(2):148-58.
105. Hirano T, Burr DB, Cain RL, Hock JM. Changes in geometry and cortical porosity in adult, ovary-intact rabbits after 5 months treatment with LY333334 (hPTH 1-34). Calcif Tissue Int. 2000;66(6):456-60.
106. Zebaze R, Takao-Kawabata R, Peng Y, Zadeh AG, Hirano K, Yamane H, et al. Increased cortical porosity is associated with daily, not weekly, administration of equivalent doses of teriparatide. Bone. 2017;99:80-4.
107. Lindsay R, Cosman F, Nieves J, Dempster D, Shen V. A CONTROLLED CLINICAL-TRIAL OF THE EFFECTS OF 1-34HPTH IN ESTROGEN-TREATED OSTEOPOROTIC WOMEN. Journal Of Bone And Mineral Research. 1993;8:S130-S.
108. Bouxsein ML, Karasik D. Bone geometry and skeletal fragility. Current Osteoporosis Reports. 2006;4(2):49-56.
109. Lotinun S, Evans GL, Bronk JT, Bolander ME, Wronski TJ, Ritman EL, et al. Continuous parathyroid hormone induces cortical porosity in the rat: effects on bone turnover and mechanical properties. J Bone Miner Res. 2004;19(7):1165-71.

110. Osima M, Borgen TT, Lukic M, Grimnes G, Joakimsen RM, Eriksen EF, et al. Serum parathyroid hormone is associated with increased cortical porosity of the inner transitional zone at the proximal femur in postmenopausal women: the Tromso Study. Osteoporos Int. 2018;29(2):421-31.
111. Zhou H, Shen V, Dempster DW, Lindsay R. Continuous parathyroid hormone and estrogen administration increases vertebral cancellous bone volume and cortical width in the estrogen-deficient rat. J Bone Miner Res. 2001;16(7):1300-7.
112. Vu TDT, Wang XF, Wang Q, Cusano NE, Irani D, Silva BC, et al. New insights into the effects of primary hyperparathyroidism on the cortical and trabecular compartments of bone. Bone. 2013;55(1):57-63.
113. Silverberg SJ, Shane E, de la Cruz L, Dempster DW, Feldman F, Seldin D, et al. Skeletal disease in primary hyperparathyroidism. J Bone Miner Res. 1989;4(3):283-91.
114. Parisien MAY, Silverberg SJ, Shane E, Cruz LDL, Lindsay R, Bilezikian JP, et al. The Histomorphometry of Bone in Primary Hyperparathyroidism: Preservation of Cancellous Bone Structure*. The Journal of Clinical Endocrinology & Metabolism. 1990;70(4):930-8.
115. Adami S, Braga V, Squaranti R, Rossini M, Gatti D, Zamberlan N. Bone Measurements in Asymptomatic Primary Hyperparathyroidism. Bone. 1998;22(5):565-70.
116. Lindsay R, Nieves J, Henneman E, Shen V, Cosman F. Subcutaneous administration of the amino-terminal fragment of human parathyroid hormone-(1-34): kinetics and biochemical response in estrogenized osteoporotic patients. J Clin Endocrinol Metab. 1993;77(6):1535-9.
117. Dempster DW, Parisien M, Silverberg SJ, Liang XG, Schnitzer M, Shen V, et al. On the mechanism of cancellous bone preservation in postmenopausal women with mild primary hyperparathyroidism. J Clin Endocrinol Metab. 1999;84(5):1562-6.
118. Onyia JE, Helvering LM, Gelbert L, Wei T, Huang S, Chen P, et al. Molecular profile of catabolic versus anabolic treatment regimens of parathyroid hormone (PTH) in rat bone: an analysis by DNA microarray. J Cell Biochem. 2005;95(2):403-18.
119. Ma YL, Cain RL, Halladay DL, Yang X, Zeng Q, Miles RR, et al. Catabolic Effects of Continuous Human PTH (1–38) in Vivo Is Associated with Sustained Stimulation of RANKL and Inhibition of Osteoprotegerin and Gene-Associated Bone Formation. Endocrinology. 2001;142(9):4047-54.
120. Locklin RM, Khosla S, Turner RT, Riggs BL. Mediators of the biphasic responses of bone to intermittent and continuously administered parathyroid hormone. J Cell Biochem. 2003;89(1):180-90.
121. Bai RJ, Cheng XG, Yan D, Qian ZH, Li XM, Qu H, et al. Rabbit model of primary hyperparathyroidism induced by high-phosphate diet. Domestic Animal Endocrinology. 2012;42(1):20-30.

122. Ma GL, Bai RJ, Yan D, Cheng XG, Qu H, Shen BZ, et al. [The study of an animal model in rabbits with the early primary hyperparathyroidism]. Zhonghua Yi Xue Za Zhi. 2010;90(43):3087-90.
123. www.iofbonehealth.org. [Available from: www.iofbonehealth.org.
124. WHO scientific group on the assessment of osteoporosis at primary health care level. WHO Scientific Group on the Assessment of Osteoporosis at the Primary Health Care Level; 7-MAY-2004; Brussels, Belgium. Geneva, Switzerland: WHO Press; 2004.
125. Cooper DM, Kawalilak CE, Harrison K, Johnston BD, Johnston JD. Cortical Bone Porosity: What Is It, Why Is It Important, and How Can We Detect It? Curr Osteoporos Rep. 2016;14(5):187-98.
126. Bala Y, Zebaze R, Seeman E. Role of cortical bone in bone fragility. Current opinion in rheumatology. 2015;27(4):406-13.
127. McCalden RW, McGeough JA, Barker MB, Court-Brown CM. Age related changes in the tensile properties of cortical bone. Journal of Bone and Joint Surgery. 1993;75A(8):1193-205.
128. Parfitt AM. The coupling of bone formation to bone resorption: a critical analysis of the concept and of its relevance to the pathogenesis of osteoporosis. Metab Bone Dis Relat Res. 1982;4(1):1-6.
129. Hattner R, Epker BN, Frost HM. Suggested sequential mode of control of changes in cell behavior in adult bone remodeling. Nature. 1965;206:489-90.
130. Lassen NE, Andersen TL, Ploen GG, Soe K, Hauge EM, Harving S, et al. Coupling of Bone Resorption and Formation in Real Time: New Knowledge Gained From Human Haversian BMUs. J Bone Miner Res. 2017;32(7):1395-405.
131. Martin RB. On the significance of remodeling space and activation rate changes in bone remodeling. Bone. 1991;12(6):391-400.
132. Heaney RP. The bone-remodeling transient: implications for the interpretation of clinical studies of bone mass change. Journal of bone and mineral research : the official journal of the American Society for Bone and Mineral Research. 1994;9(10):1515-23.
133. Andreasen CM, Ding M, Overgaard S, Bollen P, Andersen TL. A reversal phase arrest uncoupling the bone formation and resorption contributes to the bone loss in glucocorticoid treated ovariectomised aged sheep. Bone. 2015;75:32-9.
134. Hinge M, Delaisse JM, Plesner T, Clasen-Linde E, Salomo M, Andersen TL. High-dose therapy improves the bone remodelling compartment canopy coverage and bone formation in multiple myeloma. Br J Haematol. 2015;171(3):355-65.
135. Jensen PR, Andersen TL, Hauge EM, Bollerslev J, Delaisse JM. A joined role of canopy and reversal cells in bone remodeling--lessons from glucocorticoid-induced osteoporosis. Bone. 2015;73:16-23.
136. Yoneda T, Hagino H, Sugimoto T, Ohta H, Takahashi S, Soen S, et al. Antiresorptive agent-related osteonecrosis of the jaw: Position Paper 2017 of the Japanese Allied Committee on Osteonecrosis of the Jaw. J Bone Miner Metab. 2016.

137. Fung P, Bedogni G, Bedogni A, Petrie A, Porter S, Campisi G, et al. Time to onset of bisphosphonate-related osteonecrosis of the jaws: a multicentre retrospective cohort study. Oral Dis. 2016.
138. Khan AA, Morrison A, Kendler DL, Rizzoli R, Hanley DA, Felsenberg D, et al. Case-Based Review of Osteonecrosis of the Jaw (ONJ) and Application of the International Recommendations for Management From the International Task Force on ONJ. J Clin Densitom. 2016.
139. Khow KS, Shibu P, Yu SC, Chehade MJ, Visvanathan R. Epidemiology and Postoperative Outcomes of Atypical Femoral Fractures in Older Adults: A Systematic Review. J Nutr Health Aging. 2017;21(1):83-91.
140. Adler RA. Bisphosphonates and atypical femoral fractures. Curr Opin Endocrinol Diabetes Obes. 2016;23(6):430-4.
141. Cooper DML, Thomas CDL, Clement JG, Hallgrímsson B. Three-dimensional microcomputed tomography imaging of basic multicellular unit-related resorption spaces in human cortical bone. Anat Rec A Discov Mol Cell Evol Biol. 2006;288A(7):806-16.
142. Felder AA, Phillips C, Cornish H, Cooke M, Hutchinson JR, Doube M. Secondary osteons scale allometrically in mammalian humerus and femur. R Soc Open Sci. 2017;4(11):170431.
143. Jee WS, Yao W. Overview: animal models of osteopenia and osteoporosis. J Musculoskelet Neuronal Interact. 2001;1(3):193-207.
144. Pearce AI, Richards RG, Milz S, Schneider E, Pearce SG. Animal models for implant biomaterial research in bone: a review. Eur Cell Mater. 2007;13:1-10.
145. Thompson DD, Simmons HA, Pirie CM, Ke HZ. FDA Guidelines and animal models for osteoporosis. Bone. 1995;17(4 Suppl):125s-33s.
146. Pazzaglia UE, Bonaspetti G, Rodella LF, Ranchetti F, Azzola F. Design, morphometry and development of the secondary osteonal system in the femoral shaft of the rabbit. J Anat. 2007;211(3):303-12.
147. Pazzaglia UE, Congiu T, Raspanti M, Ranchetti F, Quacci D. Anatomy of the intracortical canal system: scanning electron microscopy study in rabbit femur. Clin Orthop Relat Res. 2009;467(9):2446-56.
148. Gilsanz V, Roe TF, Gibbens DT, Schulz EE, Carlson ME, Gonzalez O, et al. Effect of sex steroids on peak bone density of growing rabbits. The American journal of physiology. 1988;255(4 Pt 1):E416-21.
149. Newman E, Turner AS, Wark JD. The potential of sheep for the study of osteopenia: current status and comparison with other animal models. Bone. 1995;16(4 Suppl):277s-84s.
150. Yamane H, Takakura A, Shimadzu Y, Kodama T, Lee JW, Isogai Y, et al. Acute development of cortical porosity and endosteal naive bone formation from the daily but not weekly short-term administration of PTH in rabbit. PLoS One. 2017;12(4):e0175329.

151. Voor MJ, Yang S, Burden RL, Waddell SW. In vivo micro-CT scanning of a rabbit distal femur: repeatability and reproducibility. J Biomech. 2008;41(1):186-93.
152. Castaneda S, Calvo E, Largo R, Gonzalez-Gonzalez R, de la Piedra C, Diaz-Curiel M, et al. Characterization of a new experimental model of osteoporosis in rabbits. J Bone Miner Metab. 2008;26(1):53-9.
153. Liu X, Lei W, Wu Z, Cui Y, Han B, Fu S, et al. Effects of glucocorticoid on BMD, micro-architecture and biomechanics of cancellous and cortical bone mass in OVX rabbits. Med Eng Phys. 2012;34(1):2-8.
154. Baofeng L, Zhi Y, Bei C, Guolin M, Qingshui Y, Jian L. Characterization of a rabbit osteoporosis model induced by ovariectomy and glucocorticoid. Acta orthopaedica. 2010;81(3):396-401.
155. Wanderman NR, Mallet C, Giambini H, Bao N, Zhao C, An KN, et al. An Ovariectomy-Induced Rabbit Osteoporotic Model: A New Perspective. Asian Spine J. 2018;12(1):12-7.
156. Chen X, Giambini H, Ben-Abraham E, An KN, Nassr A, Zhao C. Effect of Bone Mineral Density on Rotator Cuff Tear: An Osteoporotic Rabbit Model. PLoS One. 2015;10(10):e0139384.
157. Qi M, Hu J, Li J, Li J, Dong W, Feng X, et al. Effect of zoledronate acid treatment on osseointegration and fixation of implants in autologous iliac bone grafts in ovariectomized rabbits. Bone. 2012;50(1):119-27.
158. Sevil F, Kara ME. The effects of ovariectomy on bone mineral density, geometrical, and biomechanical characteristics in the rabbit femur. Vet Comp Orthop Traumatol. 2010;23(1):31-6.
159. Grardel B, Sutter B, Flautre B, Viguier E, Lavaste F, Hardouin P. Effects of glucocorticoids on skeletal growth in rabbits evaluated by dual-photon absorptiometry, microscopic connectivity and vertebral compressive strength. Osteoporos Int. 1994;4(4):204-10.
160. Eberhardt AW, Yeager-Jones A, Blair HC. Regional Trabecular Bone Matrix Degeneration and Osteocyte Death in Femora of Glucocorticoid- Treated Rabbits*. Endocrinology. 2001;142(3):1333-40.
161. Castaneda S, Largo R, Calvo E, Rodriguez-Salvanes F, Marcos ME, Diaz-Curiel M, et al. Bone mineral measurements of subchondral and trabecular bone in healthy and osteoporotic rabbits. Skeletal Radiol. 2006;35(1):34-41.
162. Wen XX, Xu C, Wang FQ, Feng YF, Zhao X, Yan YB, et al. Temporal changes of microarchitectural and mechanical parameters of cancellous bone in the osteoporotic rabbit. Biomed Res Int. 2015;2015:263434.
163. Chandler H, Brooks DJ, Hattersley G, Bouxsein ML, Lanske B. Abaloparatide increases bone mineral density and bone strength in ovariectomized rabbits with glucocorticoid-induced osteopenia. Osteoporos Int. 2019;30(8):1607-16.

164. Muller R, Koller B, Hildebrand T, Laib A, Gianolini S, Ruegsegger P. Resolution dependency of microstructural properties of cancellous bone based on three-dimensional mu-tomography. Technol Health Care. 1996;4(1):113-9.
165. Jowsey J. Studies of Haversian systems in man and some animals. J Anat. 1966;100(4):857-64.
166. Lieberman DE, Pearson OM, Polk JD, Demes B, Crompton AW. Optimization of bone growth and remodeling in response to loading in tapered mammalian limbs. J Exp Biol. 2003;206(Pt 18):3125-38.
167. Hennig C, Thomas CDL, Clement JG, Cooper DML. Does 3D orientation account for variation in osteon morphology assessed by 2D histology? Journal of Anatomy. 2015;227(4):497-505.
168. Doube M, Klosowski MM, Arganda-Carreras I, Cordelieres FP, Dougherty RP, Jackson JS, et al. BoneJ: Free and extensible bone image analysis in ImageJ. Bone. 2010;47(6):1076-9.
169. Dunn O. Multiple Comparisons Using Rank Sums. Technometrics. 1964;6(3):241-52.
170. Bonferroni CE. Teoria statistica delle classi e calcolo delle probabilità. Pubblicazioni del R Istituto Superiore di Scienze Economiche e Commerciali di Firenze1936.
171. Bach-Gansmo FL, Irvine SC, Bruel A, Thomsen JS, Birkedal H. Calcified cartilage islands in rat cortical bone. Calcif Tissue Int. 2013;92(4):330-8.
172. Shipov A, Zaslansky P, Riesemeier H, Segev G, Atkins A, Shahar R. Unremodeled endochondral bone is a major architectural component of the cortical bone of the rat (Rattus norvegicus). J Struct Biol. 2013;183(2):132-40.
173. Canalis E, Delany AM. Mechanisms of glucocorticoid action in bone. Ann N Y Acad Sci. 2002;966:73-81.
174. Turner RT, Hannon KS, Greene VS, Bell NH. Prednisone inhibits formation of cortical bone in sham-operated and ovariectomized female rats. Calcif Tissue Int. 1995;56(4):311-5.
175. Jensen PR, Andersen TL, Pennypacker BL, Duong LT, Delaissé J-M. The bone resorption inhibitors odanacatib and alendronate affect post-osteoclastic events differently in ovariectomized rabbits. Calcified tissue international. 2014;94(2):212-22.
176. Jerome CP, Johnson CS, Vafai HT, Kaplan KC, Bailey J, Capwell B, et al. Effect of treatment for 6 months with human parathyroid hormone (1-34) peptide in ovariectomized cynomolgus monkeys (Macaca fascicularis). Bone. 1999;25(3):301-9.
177. Arita S, Ikeda S, Sakai A, Okimoto N, Akahoshi S, Nagashima M, et al. Human parathyroid hormone (1-34) increases mass and structure of the cortical shell, with resultant increase in lumbar bone strength, in ovariectomized rats. J Bone Miner Metab. 2004;22(6):530-40.
178. Brouwers JE, van Rietbergen B, Huiskes R, Ito K. Effects of PTH treatment on tibial bone of ovariectomized rats assessed by in vivo micro-CT. Osteoporos Int. 2009;20(11):1823-35.

179. Graeff C, Timm W, Nickelsen TN, Farrerons J, Marin F, Barker C, et al. Monitoring teriparatide-associated changes in vertebral microstructure by high-resolution CT in vivo: results from the EUROFORS study. J Bone Miner Res. 2007;22(9):1426-33.
180. Andreasen CM, Delaisse JM, van der Eerden BC, van Leeuwen JP, Ding M, Andersen TL. Understanding Age-Induced Cortical Porosity in Women: The Accumulation and Coalescence of Eroded Cavities Upon Existing Intracortical Canals Is the Main Contributor. Journal of Bone and Mineral Research. 2018;33(4):606-20.
181. Lafage-Proust MH, Roche B, Langer M, Cleret D, Vanden Bossche A, Olivier T, et al. Assessment of bone vascularization and its role in bone remodeling. Bonekey Rep. 2015;4:662.
182. Prisby RD. The Clinical Relevance of the Bone Vascular System: Age-Related Implications. Clinical Reviews in Bone and Mineral Metabolism. 2019;17:48-62.
183. Hert J, Fiala P, Petrtyl M. Osteon orientation of the diaphysis of the long bones in man. Bone. 1994;15(3):269-77.
184. Burr DB, Martin RB, Schaffler MB, Radin EL. Bone remodeling in response to in vivo fatigue microdamage. J Biomech. 1985;18(3):189-200.
185. Martin RB. Targeted bone remodeling involves BMU steering as well as activation. Bone. 2007;40(6):1574-80.
186. Buettmann EG, Silva MJ. Development of an in vivo bone fatigue damage model using axial compression of the rabbit forelimb. J Biomech. 2016;49(14):3564-9.
187. Bikle DD, Halloran BP. The response of bone to unloading. Journal of Bone and Mineral Metabolism. 1999;17(4):233-44.
188. Meakin LB, Price JS, Lanyon LE. The Contribution of Experimental in vivo Models to Understanding the Mechanisms of Adaptation to Mechanical Loading in Bone. Frontiers in Endocrinology. 2014;5(154).
189. McGovern JA, Griffin M, Hutmacher DW. Animal models for bone tissue engineering and modelling disease. Dis Model Mech. 2018;11(4):dmm033084.
190. Imanishi Y, Nagata Y, Inaba M. Parathyroid diseases and animal models. Frontiers in endocrinology. 2012;3:78-.
191. Leder BZ, Neer RM, Wyland JJ, Lee HW, Burnett-Bowie SM, Finkelstein JS. Effects of teriparatide treatment and discontinuation in postmenopausal women and eugonadal men with osteoporosis. J Clin Endocrinol Metab. 2009;94(8):2915-21.
192. Lindsay R, Scheele WH, Neer R, Pohl G, Adami S, Mautalen C, et al. Sustained Vertebral Fracture Risk Reduction After Withdrawal of Teriparatide in Postmenopausal Women With Osteoporosis. Archives of Internal Medicine. 2004;164(18):2024-30.
193. Lou S, Lv H, Yin P, Li Z, Tang P, Wang Y. Combination therapy with parathyroid hormone analogs and antiresorptive agents for osteoporosis: a systematic review and meta-analysis of randomized controlled trials. Osteoporosis International. 2019;30(1):59-70.

194. Lou S, Lv H, Wang G, Li Z, Li M, Zhang L, et al. The effect of sequential therapy for postmenopausal women with osteoporosis: A PRISMA-compliant meta-analysis of randomized controlled trials. Medicine (Baltimore). 2016;95(49):e5496-e.
195. Suvarna SKe, Layton Ce, Bancroft JDe, Elsevier issuing b. Bancroft's theory and practice of histological techniques. Eighth edition.. ed2019.

APPENDIX A

My master's thesis project initially aimed to measure LER histologically in the PTH rabbit model to compare against previous characterizations of LER as well as to direct measures derived from longitudinal *in vivo* imaging studies. This appendix outlines several of the histological protocols I explored to produce longitudinal sections of undecalcified bone for measuring LER based on the bone microarchitecture and *in vivo* fluorochrome labels that a future graduate student can build upon.

A.1. Methylmethacrylate Embedding for Undecalcified Bone

The following protocol will produce sections of bone embedded in methylmethacrylate (MMA) that can be utilized for thin serial sectioning or for optical sectioning with confocal microscope. The Osteobed Bone Embedded Kit is recommended for this protocol.

Bone Processing

1. Clean bones of soft tissue.
2. Cut bones to desired length using a Beuhler Slow Speed Isomet saw. For rabbit tibiae, cut the diaphysis into 0.5-1 cm long sections.
3. Fix specimens in 10% neutral buffered formalin in a tightly closed container. Fixation time will vary depending on sample size. For the rabbit sections above, fix for at least 1 week. Fixation rate can be accelerated by agitating or vacuuming.
4. After fixation is complete, store bones in 70% ethanol until processing commences. This is ideal for long-term storage to prevent the loss of fluorochrome labels in bone caused by partial decalcification with prolonged fixation in formalin.
5. Dehydrate bones in graded ethanol (EtOH) solutions as follows: 70% EtOH, 80% EtOH, 95% EtOH, 95% EtOH, 100% EtOH, 100% EtOH, 100%, EtOH, xylene, and 100% EtOH. Processing time will vary depending on sample size. Specimens should be dehydrated in 10 times the volume of the sample. Vacuum specimens for 3-4 hours for each step and agitate samples. If a automated tissue processor is available, set it to run the following processing schedule:
    - EtOH 70% 6 hours, 80% EtOH 6 hours, 95% EtOH 3 hours, 95% EtOH 3 hours, 100% EtOH 4 hours, 100% EtOH 4 hours, 100% EtOH 4hours, 50% EtOH/50% xylene 2 hours, xylene 6 hours, xylene 30 hours, 100% EtOH 6 hours.
    - Start infiltration immediately after processing.

Bone Infiltration

Pre-Infiltration

1. As per the instructions of the Osteobed Bone Embedding Kit, calculate the amount of pre-infiltration solution needed; all infiltration liquids should be 10 equivalent volumes of the specimen and be placed in 2 changes of pre-infiltration solution to allow removal of

alcohol and tissue fluids. Pre-infiltration should be completed under a fume hood and with limited exposure to direct light.

2. Measure out Resin Solution in graduated cylinder and infiltrate specimens with Resin Solution in opaque plastic container with tight fitting lid.
3. In fume hood, vacuum specimens at 15-20 in.Hg for 6-8 hours, releasing vacuum every 30 minutes. Infiltrate in fume hood or in refrigerator for the remaining time until next change (~3 days). Pre-infiltration time may need to be modified depending on size of specimens. The recommendation in this protocol is for rabbit tibial samples approximately 0.5cm x 0.5 cm in size.
4. Change pre-infiltration solution and repeat steps for an additional day.

Infiltration

5. Prepare infiltration solution one day prior to infiltration. Calculate the amount of infiltration solution needed; all infiltration liquids should be 10 equivalent volumes of the specimen to allow removal of alcohol and tissue fluids. The ratio is 1.4g Catalyst per 100mL of Resin Solution. This should be completed under a fume hood and with limited exposure to direct light.
6. Weigh Catalyst in weight boat and place into plastic container with tight fitting lid and magnetic stir bar.
7. Measure Resin Solution using graduated cylinder. In fume hood, add Resin solution to opaque plastic container with tight fitting lid and stir for 4 hours with magnetic stir bar. Solution will become cloudy.
    a. Promptly store solution at 2-8°C. Solution can be stored up to 4 weeks.
8. In fume hood, add infiltration solution into opaque plastic containers with tight fitting lid.
9. In fume hood, vacuum specimens at 15-20 in.Hg for 6-8 hours, releasing vacuum every 30 minutes. Repeat for ~3 days and refrigerator samples in between.

<u>Bone Embedding</u>

1. Prepare embedding medium one day prior to embedding. Calculate the amount of embedding medium needed according to volume of molds (19/65 mm 3 Dram (~10 ml) glass vials are recommended). The ratio is 3.5g of Catalyst per 100ml Resin Solution.
2. Weigh Catalyst and measure out Resin Solution and place in opaque plastic container with tight fitting lid. Dissolve and mix for 4 hours with magnetic stir bar. This should be completed under a fume hood.
    a. Solution will become cloudy. Promptly store solution at 2-8°C. Store up to 4 weeks.
3. Place samples into opaque plastic container with embedding medium. Place into vacuum for 4 hours at 15-20 in.Hg. Tightly cap and leave in refrigerator to further infiltrate specimen and vacuum the next day for 4-6 hours (total infiltration ~48 hours).

4. Before polymerization step, prepare water bath setup at least 12 hours in advance. Pre-heat oven with water bath (37°C). Check temperature with thermometer.
5. Under a fume hood, place specimen into glass vial with forceps. For longitudinal sections, position the bone so that the longitudinal axis of the diaphysis is parallel with the base of the glass vial. Pipette embedding solution into glass vial with plastic pipette. Do not completely fill glass vials with resin as it may increase polymerization temperature.
    a. *Optional*: For a pre-polymerized base, pipette 3-5 mm of embedding solution into vial. Cap the vial and place into water bath for 2 hours to make viscous base before adding specimen and filling the rest of the vial with embedding solution.
6. In fume hood, vacuum specimen for 1 hour in vials at 15-20 in.Hg to remove any trapped air in the specimen.
7. After vacuuming, adjust final position of specimen to ensure it is centered within the vial and cap vial tightly. The presence of oxygen inhibits polymerization at the surface. Place vials into water bath at 37.0°C for at least 24-48 hours. Larger volumes may require longer polymerization times. Do not disturb container. Do not overcrowd water bath as this can increase polymerization temperature and cause bubbling.
8. Remove blocks from molds when resin has fully cured.
    a. Place glass vial with sample block into bag with towels. Carefully smash vial to free sample block with cut resistant gloves. Carefully dispose of broken glass in the appropriate container.
9. Remove any unpolymerized resin on top of block by scraping it off. Sample blocks can now be sectioned with a microtome to produce thin, serial sections or cut with a slow-speed saw to produce a thick section (~500 μm) for optical sectioning with confocal microscope.

A.2. Serial Sectioning of Undecalcified Bone with Automated Microtome

The following protocol is for sectioning undecalcified bone in MMA using an automated microtome. This protocol uses the Microm 350S automated microtome. A sledge or sliding microtome would be ideal for this technique. Tungsten carbide blades are recommended for sectioning hard tissues like undecalcified bone.

1. Retract sample holder of automated microtome in preparation for sectioning.
2. Secure bone sample into holder and tighten the clamp using associated knobs. Align the sample to produce sections within the desired place.
    a. Ensure the block face of the sample is directly parallel to the holder.
    b. If needed, adjust the position of sample, by first releasing the sample holder clamp and then using the various adjusting knobs to modify the position of the clamp and sample. Re-tighten the holder when finished.
3. Carefully place tungsten carbide blade into knife holder. First release the right block handle of the knife holder, insert the blade using forceps, and re-fasten.
    a. Ensure blade is level.
    b. Label the blades for future reference. Designate one blade for trimming and make note of which blades are used for sectioning.
    c. Before sectioning with a previously used blade, clean it in fume hood by wiping away any remaining residue from the blade with a Kimwipe dipped in xylene. Allow fumes to evaporate in fume hood for 2-3 minutes before sectioning.
4. Adjust clearance angle and section thickness.
    a. Adjust clearance angle with right knob of holder (~4°).
    b. Set cutting speed at 4.
    c. Adjust the section thickness dial; 20 μm for trimming, 5-10 μm for sectioning.
5. Bring the sample close to the blade by moving the knife holder backwards (release the left handle and slide backwards) with approximately 1 mm of space between. Use the automated extender button on the control pad to advance the sample closer to the blade.
6. Ensure everything is secured tightly in place. This is very important for producing consistent, even sections as instability can induce chatter (vibration of blade edge).
7. Start trimming the block. Use 30% EtOH to lubricate the block face before sectioning the block by rubbing an ethanol soaked Kimwipe over the blockface every few sections. Begin by trimming the block manually by turning the right wheel to produce a section. Make sure to remove any MMA or bone residue every few sections from the block face and the blade with a paintbrush for smooth and consistent sectioning and to prevent imperfections in section.
8. Once you have reached the desired region of interest (ROI) of the sample, switch the blade to a new, sharp blade and start automatically sectioning the block by pressing start on the control pad. It is very important the blade is sharp for successful and consistent sectioning. Blades that contain nicks can introduce tearing of the section. The microtome will automatically advance the sample block to produce consistent sections of a desired

thickness. Thin sections of MMA with the sample will be produced that can be set aside with forceps.

   a. Press the red or yellow stop button to stop at any time or when finished.

9. Place sections on glass microscope slides and flatten. This can be achieved by carefully stretching sections over slides with forceps and then covering with plastic wrap with weight to prevent the section from rolling up. Mount section onto slide with fluorochrome protective mounting medium and coverslip. Sections should be stored to avoid exposure to light (opaque slide box) in order to protect the bone fluorochrome labels.
10. Once finished, carefully remove blade by releasing right handle of knife block, and using forceps to remove blade.
11. Clean microtome and dispose of large MMA and bone residue into waste bag and remaining residue with 70% EtOH with Kimwipes.
12. For analysis, image sections with a microscope with fluorescent capabilities to capture fluorescent labels. Image stacks can then be assembled to produce a 3D render for analysis.

A.3. Optical Sectioning of Bone with Confocal Microscope

The following protocol uses the Leica DMi8 confocal microscope for analysis of thick ground sections of undecalcified bone embedded in MMA by z-stack imaging.

1. Prepare Leica DMi8 microscope and associated software for imaging.
    a. Remove Microscope Cover.
    b. Ensure microscope stage is in its lowest position, on the lowest objective.
    c. Turn on laser (green switch on the large black system).
    d. Turn on microscope (switch on white electronic box).
    e. Allow microscope to calibrate.
    f. Turn on computer and open up LasX program (Machine, DMIS, ok).
2. Ensure microscope slide is clean by carefully wiping it with a KimWipe and cleaning spray.
3. Carefully tilt the transmitted light arm on the microscope backwards to place slide onto stage upside down. The sample should be facing down.
    a. The slide should fit into the indentations on the stage and held into place with metal clips.
4. To turn on the light source, click the buttons on the motorized objective nosepiece and motorized fluo turret panel located below the eyepiece to open the shutter.
5. Bring the section into focus and adjust its x-y position. Use course and fine adjusting knobs on side of microscope to focus on section and adjust x-y position using SmartMove controls to move the stage (white knobs).
6. Once the ROI within the section is in focus, change objectives if desired. Rotate through the objective nosepiece (dial located under the stage- 10X, 20X, 40X, 60X) and adjust fine focus with each magnification.
7. Before turning on laser system, turn off lights.
8. In LasX program, make a new project. All subsequent images will be saved here.
9. Use the combination of fluorescence and transmitted light differential interference contrast (DIC) for imaging. A previous scan with the desired image settings can be opened by locating the file, right clicking on it and selecting “Apply Image Settings”. This will prompt a window with a reminder to turn on the laser. Turn the key of the laser system to turn it on (big black box), and then press ok on the program to confirm. Oil immersion or dry immersion may be used. Depending on sample, image settings will need to be modified. For dry immersion, settings are set to:
    a. Objective: HXC PL FLUOTAR 5x/0.15 numerical aperture
    b. Wavelength excitation: 488 nm using TD 405/488/635 beamsplitter
    c. Laser intensity: 30%

<u>Adjust Imaging Parameters</u>

1. While modifying imaging settings, use the image format 512 x 512.

2. Adjust the settings for transmission and fluorescence axes separately by toggling between them using the sequential tab (bottom left hand corner). Start with fluorescence view.
3. Click Live to project live view of section on computer so that you can simultaneously adjust settings.
4. Use the z position knob on the control panel in front of the computer to move through the section and locate the region that emits the brightest fluorescence. Then use the fine focusing knob to adjust.
5. Click on the icon on the top left corner (Quick Lookup Table button) to toggle to the detector signals to adjust the gain and the offset. This will allow the signal intensity and noise level of the image to be adjusted.
    d. To adjust Smart Gain (signal amplification), turn the 1st knob on control panel (left) to approximately ~700 V.
        i. In fluorescent image, ensure the pixels of detected signals of the fluorescent labels are mainly red and white, limiting the amount of blue pixels, which indicates an over-saturated signal. Lower the gain if there is too many blue pixels and increase gain to maximize brightness. The sample position may also need to be adjusted to find the optimal plane of section.
    e. To adjust Smart Offset (the minimum signal intensity detected by the sensor), turn the 2nd knob on black panel to approximately ~0.6%.
        i. In fluorescent image, background should be is mostly green with a little black (this indicates there is no signal/ noise). Adjust offset until black pixels just mostly disappear.
        ii. Click the icon in the top left corner to return to normal view.
6. Click Stop, switch microscope settings to transmission and then adjust DIC image.
7. Click Stop once adjustments are completed.
8. Once the image has been adjusted to produce the desired image, snapshots of images can be taken by clicking on Capture. If both fluorescence and DIC are to be taken, select both views in the sequential tab. Rename the file under the project tree.

<u>Tiled Scan</u>

1. If specimen is large, utilize a tile scan. Click on the tiled image tab and use the imaging format 512 x 512 while adjusting image settings. Set image speed to 600.
2. Click Live, find region of interest (ROI) on the section and adjust the image as above if needed.
3. Click Stop and change image format to 2048 x 2048.
4. Select field size as 5 x 5 or 10 x 10 (this depends on the size of the ROI to be imaged).
5. In the stage window, zoom out to find the middle of the slide.
6. Select Merge On.
7. Select Start to begin tile scan.

8. Once tile scan if finished, you can repeat for all other ROIs. Once all tile scans are complete, delete the tiled scan tab or it will be applied to other scans (ie., standard images or z-series scans). The output will contain all of the individual tiled fluorescence and DIC images, as well as a complete, stitched together final image.
9. Rename the tile scan under the project tree.

Z-Series

1. To create a 2D image stack, begin with the image format of 512 x 512.
2. Click on Z series.
3. Click Live, and adjust image of desired ROI.
4. Use the fluorescence mode to set up z-stack.
5. Define the volume of bone to be imaged:
    a. Using Z series knob (last knob on the right of the control panel), turn the knob counterclockwise until the top or "beginning" of the sample is reached. The image will appear blurry and the fluorescence will be faint.
    b. Once this limit is reached, click Begin under the z-series tab and turn the same knob clockwise until the bottom or "end" of the sample is reached Click on End.
6. If needed, select move to center and adjust focus to find optimal image.
7. Click Stop and select the 2048 x 2048 image format.
8. Define the resolution of the z-stack by entering in desired z step size (~0.5-5 μm). Based on the image step, image and pixel size, the number of steps will be calculated and the optical section thickness will be produced.
9. Select the z-series to run between frames (alternating between fluorescence & DIC images) or between stacks (will run stack through all fluorescence, then DIC).
10. Press Start to begin Z series.
11. Once finished, a 3D reconstruction of the z-stack can be visualized by clicking on the 3D icon in the top, right window. Additional modifications to the z-stack can be made in this program.
12. When finished, rename the z-series under the project tree.

Confocal Microscope Shutdown

1. Save project by clicking on the Save icon to the right of the project tree.
2. Begin shut down process of microscope.
    a. Switch off laser with Laser Key.
    b. Exit LasX software.
    c. Switch to 5x objective and lower stage to its lowest position.
    d. Shut down computer.
    e. Switch off supply unit at power switch.
    f. Switch off microscope (white box).
    g. Put microscope cover on microscope.

Z-Stack Assessment

1. Open Leica file (lif) that contains the z-stack in Fiji or in Image J (with Bio-Formats plugin).
2. A window will appear that contains a list of all the images collected within the project. Select the images or image series to be analyzed. Click OK.
3. The selected project will open as separate z-stacks, for fluorescent and transmission (DIC) channels. The appropriate colour may need to be applied: Image > Lookup Tables > Grays for DIC images & Green for fluorescent calcein images. To assess fluorescent and DIC images together, merge the two image stacks by selecting Image > Color > Merge Channels and select the DIC image under the G4 Gray category and the fluorescent image under the C2 Green category. Keep source images. Click ok. To convert the 2 slice stack into an image, select Image > Color > Stack to RGB. Save the images in tiff format.
4. A raw 3D render can be generated in by selecting Image > Stack > 3D Project.
5. Further image processing in other 3D data visualizing software is required to produce the desired, final 3D render.

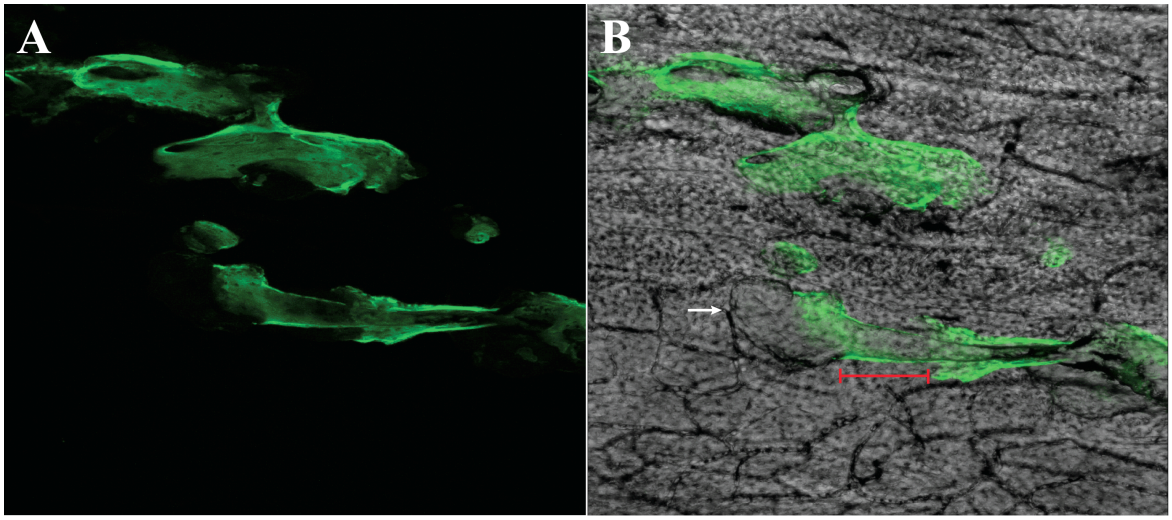

Figure A.1. (*A-B*) Fluorescent confocal and differential interference microscopy 2D image (z) stacks of a longitudinal section (~400 μm) of undecalcified PTH rabbit bone (from Chapter 3) depicting an example of a BMU from which LER can be measured from. In *B*, the white arrow indicates the tip of the cutting cone of the BMU and the red bar indicates the region where LER would be measured (between the 2 fluorescent calcein labels).

A.4. Cryosectioning of Undecalcified Bone

The following protocol produces thin frozen sections of undecalcified bone. The Kawamoto Tape Transferring Method is recommended for this protocol. Materials for this method can be found at http://www.section-lab.jp/. This protocol utilizes the TBS cryostat.

Cryo-Embedded Specimen Preparation

1. Cryosections can be prepared from fresh or fixed bones. For fixation, place bone specimens in 10% formalin solution for at least 48 hours. Fixation time will vary depending on size of specimens. For 0.5 cm x 0.5 cm sections of rabbit tibiae, fix for 5-7 days.
2. Incubate bones in 30% sucrose in 0.1M phosphate buffered saline (PBS) for 1 week at 4°C.
    a. 30% Sucrose: Dissolve 30 g sucrose in 70 ml 0.1M PBS. Once dissolved, make up volume to 100ml with 0.1M PBS.
3. Prepare a large beaker (2000 ml) or Styrofoam container with dry ice and ethanol (2:1) under fume hood. Place small beaker (150-250 ml volume) with hexane (30-50 ml) inside container. Allow hexane to cool, approximately 10 minutes until frost appears outside of the small beaker.
4. Fill ¾ of labelled square or rectangular mold (Polysciences Peel-A-Way molds are recommended) with Cryo-embedding medium. Supercryoembedding Medium (SCEM) is recommended but Optimal Cutting Temperature medium (OCT) can also be used. Carefully place specimens into molds until fully immersed taking care not to touch the edge of the mold. For rabbit tibiae, position longitudinal axis of diaphysis so that it is parallel with base of mold. Make sure bubbles are removed. With forceps, hold the cryomold with the specimen into the beaker so that the bottom of mold just touches the surface of the cooled hexane.
5. Allow the outer edges of the embedding medium to freeze (indicated by opacity, approximately 15 seconds). Fully drop the mold into the hexane and allow freezing for 1-2 minutes. Once frozen, remove sample from hexane and immediately wrap it in cellophane and aluminum foil to prevent it from drying out or being exposed to light.
6. Repeat for other samples, adding additional dry ice to ethanol to ensure quick freezing of specimens. Store samples at -80°C until sectioning commences.

Cryo-Sectioning

1. Set the cryochamber temperature to -24°C /-25°C.
2. Place frozen sample block in cryochamber to acclimatize for at least 1 hour.
3. Prepare cryofilm (Cryofilm Type 3C- 16UF, 2.5mm) by cutting sheets into sections large enough to just cover the ROI of the specimen in the frozen block. Place into cryostat to chill. Pre-chill roller, small paintbrush, slides, and forceps.
4. Once sample block has acclimatized, fix it onto the sample holder chuck using SCEM or OCT. Ensure sample block is positioned on chuck so that block edge is parallel to blade

edge. This may require some additional adjustments to get accurate positioning. Failing to do so can result in uneven, inconsistent sections. Allow freezing for 5 minutes.

5. Secure the chuck with the sample block onto the holder. Ensure the bottom of the block edge is parallel with where the blade would sit. Adjust position of holder by turning the associated adjusting knob if necessary.
6. Disengage the ratchet pawl handle located in the back of the cryostat chamber.
7. Retract sample holder to starting position by pressing retract button on cryostat. This will move the system towards the back.
8. Carefully place tungsten carbide blade in knife holder with forceps and secure.
9. Adjust the position of the knife holder so that it is close to the sample with approximately 1 mm of space between. Release the knife holder using its front lever and slide it backwards towards the block face edge. Secure knife holder in place. Use the advance button on the cryostat to slowly advance the blade forward, towards the sample. The sample should now be at a position that it can produce a thin section. It may take some adjustments to ensure the blade does not cut into the sample too deeply, which can damage the block or the specimen.
10. Engage the ratchet pawl handle.
11. Adjust the section thickness to 10-16 μm for trimming. To adjust section thickness, release the thickness knob and select the desired section thickness. Re-tighten the knob.
12. Trim the block by rotating the handle located on the right side of the cryostat manually until the ROI appears on the cut surface. Clean away any cryoembedding medium or bone residue from the block surface and the blade every few sections using the paintbrush to keep sections clean and consistent.
13. After trimming, move the blade edge to a new position or place a new, sharp blade into the knife holder. Set desired section thickness (~10 μm for rabbit tibiae).
14. Remove the paper cover from the cryofilm by holding the metallic, non-sticky edge with forceps and peeling from the backing. Mount the cryofilm onto the clean, cut surface with the metallic section on the inferior edge of the ROI and tightly adhere the film to the block surface using the pre-chilled roller.
15. Hold the edge of the cryotape with forceps as the section is cut such that the section does not fall off the stage during sectioning. Section the block in one quick, swift motion. The bone section should be stuck onto the cryofilm.
16. Place the section tissue side up on a microscope slide within the cryostat. Allow sections to dry for 30 minutes. Then remove the slide from the cryostat and allow the cryo-embedding medium to melt such that the section adheres to the surface of the slide. Sections can either be taped directly onto slides or mounted onto slides using fluorochrome protective mounting medium with a cover slip. Sections can be stored in slide boxes at -80°C.
17. For analysis, assess fluorescent labels using a microscope with fluorescent capabilities. Images can be assembles into 3D volumetric renders for analysis.